NUMERICAL AND EXPERIMENTAL ASSESSMENT OF MRI RF COIL INDUCED HEATING FOR EXTERNAL FIXATION DEVICES AND TECHNIQUE TO REDUCE THE THERMAL EFFECTS

A Dissertation

Presented to

the Faculty of the Department of Electrical and Computer Engineering

University of Houston

In Partial Fulfillment

of the Requirements for the Degree

Doctor of Philosophy

in Electrical Engineering

by

Xin Huang

May 2016

NUMERICAL AND EXPERIMENTAL ASSESSMENT OF MRI RF COIL INDUCED HEATING FOR EXTERNAL FIXATION DEVICES AND TECHNIQUE TO REDUCE THE THERMAL EFFECTS

Xin Huang

Approved:

Chair of the Committee
Ji Chen, Professor
Electrical and Computer Engineering

Committee Members:

Donald R. Wilton, Professor Emeritus
Electrical and Computer Engineering

David R. Jackson, Professor
Electrical and Computer Engineering

Nikolaos V. Tsekos, Associate Professor
Computer Science

Driss Benhaddou, Associate Professor
Engineering Technology

Wolfgang Kainz, Senior Principal Scientist, U.S. Food and Drug Administration

Suresh K. Khator, Associate Dean
Cullen College of Engineering

Badri Roysam, Professor and Chair
Electrical and Computer Engineering

Acknowledgements

I would like to give special thanks to my advisor Prof. Ji Chen, who has provided me with excellent guidance and support since I came to University of Houston. Without his valuable suggestions, my research would not be complete. Prof. Ji Chen has been a great mentor and friend who has been very encouraging through the challenging process of completing my degree.

I would also like to express deep appreciation to the members of my dissertation committee: Dr. David Jackson, Dr. Donald Wilton, Dr. Nikolaos Tsekos, Dr. Driss Benhaddou, and Dr. Wolfgang Kainz for their time and commitment. Their assistance and constructive criticism are of utmost importance to my research.

In addition, I would like to thank Ms. Shiloh Sison, and Dr. Gabriel Mouchawar for offering an internship opportunity in St. Jude Medical. The experience I gained during 2015 summer internship expanded my horizons and had made a great impact on my Ph.D research.

I would like to thank the colleagues and friends in my research group: Dr. Yan Liu, Dr. Zubiao Xiong, Dr. Shi Feng, Dr. Xichen Guo, Dr. Jianfeng Zheng, Dr. Cong Gao, Mr. Dawei Li, Mr. Qingyan Wang, Ms. Qi Zeng, Ms. Mengna Yang, Mr. Jingshen Liu, Mr. Ran Guo, Ms. Xiaohe Ji, Ms. Xinyu Liu, Ms. Sohini Sengupta, and Ms. Krishna Kota for their kindness and friendship. With their company, challeging graduate study has become full of passion and pleasure. The same appreciation also goes to Ms. Brandie Yale, Ms. Jan Zaniffa and all other staff in the ECE department for their help with patience and discretion.

Finally, I would like to thank my family and my girl friend for always being supportive and providing encouragement. I am grateful for their love and support.

NUMERICAL AND EXPERIMENTAL ASSESSMENT OF MRI RF COIL INDUCED HEATING FOR EXTERNAL FIXATION DEVICES AND TECHNIQUE TO REDUCE THE THERMAL EFFECTS

An Abstract

of a

Dissertation

Presented to

the Faculty of the Department of Electrical and Computer Engineering

University of Houston

In Partial Fulfillment

of the Requirements for the Degree

Doctor of Philosophy

in Electrical Engineering

by

Xin Huang

May 2016

Abstract

Tissue heating under MRI environment is one of the primary concerns in MRI related safety, especially with the presence of medical devices. This dissertation focuses on the MRI RF coil induced heating effects of external fixation devices and the technique to reduce such thermal impact. Different categories of external fixation devices, including modular external fixation devices and circular external fixation devices are investigated both numerically and experimentally.

Published literature has studied the RF induced heating effects on modular external fixation devices. The shortest insertion depth, largest pin spacing and conductive bar will result in worst-case heating. Using absorption material is proposed as an effective way to reduce the RF induced heating effects. With the proper choice of absorption material, the maximum 1g-averaged SAR can be significantly reduced by more than 70 % through simulation study. Experimental results also show the effectiveness of the technique.

When we assess the MRI RF coil induced heating for circular external fixation devices, the conventional testing approach does not apply. A novel leg phantom was designed. Good agreement can be seen from a comparison of the electric field or SAR distribution between the human model and leg phantom. Numerical study suggests that all screw configurations with fewer screws, large ring frame size and relatively large strut length and the maximum insertion angle pointing outwards may lead to the worst case MRI RF coil induced heating.

The usage of absorption material has the same impact on circular external fixation devices. For the worst case scenario, using low permittivity absorption material with appropriate conductivity can reduce the 1g-averaged SAR from 346 W/kg to 26 W/kg. Based on the induced current behavior, we propose a circuit model of MRI RF coil induced heating on external fixation devices, which gives qualitative insights on the

mechanism of the heating reduction using absorption material.

Preliminary error quantification is discussed for simulations and experiments. By using a simple case for which analytical solutions are possible, the simulation uncertainty is bounded within 6.7%. By using an uncertainty budget, the combined uncertainty is shown to be 14.99% for standard testing method for MRI RF experiment system.

Table of Contents

List of Figures

List of Tables

Chapter 1

Introduction

1.1 RF Coil Induced Heating in MRI System

Magnetic Resonance Imaging (MRI) has become the diagnostic tool of choice over recent decades due to its non-ionized nature and high-resolution image quality for soft tissues. Although MRI does not use ionized radiation, there are other potential safety hazards related to MRI scans. Most of the issues are associated with the interaction between electromagnetic (EM) field produced by MR system and medical devices. In 2005, a set of MRI labeling terms for medical devices was developed and released [1]. This terminology, which is currently recognized by the Food and Drug Administration (FDA), is as follows: (a) MR Safe - an item that poses no known hazards in all MRI environments. (b) MR Conditional - an item that has been demonstrated to pose no known hazards in a specified MRI environment with specified conditions of use. Conditions that define the MRI environment may include the strength of the static magnetic field value, the spatial gradient magnetic field value, the time-varying magnetic field value, the radio frequency (RF) field value, and the specific absorption rate (SAR) level. Additional conditions, including the specific configuration for the item may be required. (c) MR Unsafe - an item that is known to pose hazards in all MRI environments [2].

Safety hazards related to MRI environment include undesired force, torque, tissue heating, image artifacts, and device malfunction. While many of these hazards may be greatly reduced by utilizing non-magnetic materials for medical devices, one of the primary safety concerns is tissue heating by the absorption of radiofrequency (RF) energy. The intensive electromagnetic field that is emitted by MRI RF coils during scanning can penetrate into biologic tissues and cause thermal effects. The RF induced heating can be extremely severe with the presence of conductive medical implants. Metallic parts of medical devices will interact strongly with the electromagnetic field. Localized energy can be deposited near the edges of these medical devices and lead to high temperature increase near devices. For example, the temperature elevation of deep brain stimulation (DBS) electrode is reported to be as high as 25.3 °C [3]. By following international standards, studies on numerous medical devices have been carried out over years to provide guidance with respect to MRI RF induced heating evaluation including orthopedic implants [4–10], pacemakers/defibrillators [11–15], and deep brain stimulators [16–18]. While a number of fully implanted medical devices are investigated in published literature, there is an increasing trend to study the heating effect of external fixation systems. Luechinger et al. evaluated a group of nonmagnetic large external fixation clamps and frames in the MR environment and found a maximum temperature increase of 4.1 °C at the tip of metallic pin [19]. Liu et al. studied the heating effects of external fixators with different structures [20]. Under certain worst-case MR circumstances, the huge temperature increase can lead to permanent damage to human tissues. In this study, we focus on the RF coil induced heating effects of external fixation devices.

1.2 Current Regulations for MRI RF Heating and Limitations

The process of determining whether a given medical device causes tissue heating above safe levels is subject to international standards. Demonstrating that a device will not cause patient harm is of utmost importance in the process of obtaining proper labeling for devices in the marketplace. The following standards are defined recently to assess safety of medical devices in MRI, particularly in RF heating aspect.

The ASTM 2182 standard entitled Standard Test Method for Measurement of

Radio Frequency Induced Heating On or Near Passive Implants during Magnetic Resonance Imaging covers measurement of RF induced heating on or near a passive medical implant and its surroundings during MRI. This test method assumes that testing is done on devices that will be entirely inside the body [21].

The implant to be tested is placed in a phantom material that simulates the electrical and thermal properties of the human body. The implant is placed at a location with well characterized exposure conditions. An RF field producing a sufficient whole body averaged SAR of about 2W/kg averaged over the volume of the phantom is applied for approximately 15 min. The test procedure is divided into two steps. In Step 1, the temperature rise on or near the implant at several locations is measured using fiber-optic thermometry probes (or equivalent technology) during approximately 15 min of RF application. Temperature rise is also measured at a reference location during Step 1. In Step 2, the implant is removed and the same RF application is repeated while the temperature measurements are obtained at the same probe locations as in Step 1.

The ISO/TS 10974 standard entitled Assessment of the safety of magnetic resonance imaging for patients with an active implantable medical device is applicable to implantable parts of active implantable medical devices (AIMDs) intended to be used in patients who undergo a magnetic resonance scan in 1.5 T, cylindrical bore, whole body MR scanners for imaging the hydrogen nucleus [22].

Determining the rise in local tissue temperature due to interaction of an AIMD with the RF field of an MRI scanner is a complicated process, and depends on AIMD design, MRI scanner technology (RF coil and pulse sequence design), patient size, anatomy, position, AIMD location and tissue properties. Depending on the specific conditions, variation of in vivo temperatures may span several orders of magnitude. A four-tier testing approach is described in order to accommodate the diversity of AIMD configurations and specific applications. After the determination of a conservative estimate of energy deposition, including the uncertainty, in a controlled in vitro system, the second step is to assess the maximum in vivo temperature rise using previous assessed energy deposition.

The IEC 60601-2-33 standard entitled Particular requirements for the basic safety and essential performance of magnetic resonance equipment for medical diagnosis establishes specific basic safety and essential performance requirements for MR equipment to provide protection for the patient and the MR worker [23]. The standard categorized MR equipment into 3 operating modes: a) normal operating mode b) first level controlled operating mode and c) second level controlled operating mode. Specific whole body SAR limits are described in details for each mode.

Although the standards give guidelines for MRI labeling for a medical device, there are still many limitations in regards to external fixation devices. ISO/TS 10974 only deals with AIMD; IEC 60601-2-33 applies to the basic safety of MR equipment and MR systems, i.e., no specific description of medical devices is mentioned; ASTM F2182 assumes that testing is done on devices that will be entirely inside the body. For external fixation devices, modifications of the testing methods in each standard are necessary.

1.3 Motivation

Recently, people have viewed MRI as an interventional tool for minimally invasive image-guide interventions [24]. However, because of the potential RF heating issue, there has been reluctance in medical community to take interventional MRI techniques in surgery. Compared to other imaging techniques such as x-ray fluoroscopic guidance, MRI has no known long-term health risks [25]. It would be regrettable if a patient were prevented from MRI-guided intervention merely for fear of potential RF heating issue. Therefore, the risk of RF heating needs to be appropriately quantified to give a precise assessment. Due to the limitation of current regulations, new criteria should be derived.

On the other hand, there is also an urgent need for the reduction of RF heating effects to an acceptable level. Efforts have been made to reduce such high temperature rises for external fixation devices during an MR scan. The method of using electrical insulating material was considered. Liu et al. studied the effect of electrical insulated material, and found it can potentially lower the induced RF heating [26]. However, the capability of an insulating layer for RF heat reduction is limited since the RF fields at MRI operating frequencies can be coupled to the device pins via the capacitive coupling. In this study, novel solutions to reduce RF-induced heating for external fixation devices are proposed.

1.4 Overview

The remainder of the proposal is organized as follows. In Chapter 2, the basic methodology of MRI RF coil induced heating assessment is described, including the mechanism of RF induced heating, external fixation devices, numerical simulation and experimental setup. RF induced heating can be decoupled into a two-step process. Two categories of external fixation devices, i.e., modular external fixation and circular external fixation, are described. Numerical modeling of MRI environment is introduced in detail. The experiment testing procedure is also discussed.

In Chapter 3, some current results and progress have shown the effectiveness for MRI RF heating reduction on modular external fixations. The incorporation of absorption material has proven to be a potential way to reduce MRI RF heating in both simulation and experiment aspects.

In Chapter 4, a novel leg phantom design has been proposed for both numerical and experimental assessment of MRI RF heating induced by external fixation devices. New evaluation schemes are proposed to appropriately quantify the heating effects.

Numerical studies compared to the human body simulations were carried out to show the validity of the leg phantom design. Parameter-sweeping strategy is used to search for the worst-case RF induced heating scenario of circular external fixation.

In Chapter 5, the technique of using absorption material is applied after we get the worst case through previous searching strategy. Through simulation and experimental studies, the reduction capability of absorption material has been verified. A simple circuit model has qualitatively explained the heating reduction mechanism.

Uncertainty analysis plays an important part in measurement. In Chapter 6, preliminary study of how selected parameters affect the temperature increases are discussed. Quantitative results are provided for standard testing cases.

Conclusions will be drawn in Chapter 7, where potential related topics are introduced in the future work.

Chapter 2

Methodology to Study RF Coil Induced Heating

A basic description of RF Coil induced heating analysis is introduced in this chapter. A two-coupled-problem model of RF induced heating mechanism is presented. Categorization of external fixation regarding RF induced heating is proposed by frame application. Standardized simulation tools and experiment instruments are described in detail. The implementation of the above forms the foundation for RF coil induced heating evaluation.

2.1 RF Coil Induced Heating Mechanism

Tissue heating during an MRI scan occurs due to the RF-induced electric field produced in the body. Published studies in literature have revealed the mechanism of RF induced heating as a two-step process depicted in Figure 2.1[27]. The problem of RF coil induced heating can be decomposed into two coupled problems: an electromagnetic problem and a heat transfer problem.

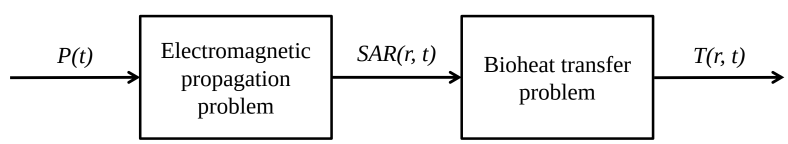

Figure 2.1. Two-step model of RF coil induced heating in MRI.

The electromagnetic problem is modeled with Maxwells equations. RF power deposited into the body is quantified by the specific absorption rate (SAR), which is measured in W/kg, and determined by

$$SAR = \frac{\sigma E^2}{\rho}, \tag{2.1}$$

where σ is the electrical conductivity in S/m, E is the electric field amplitude, and ρ is the mass density.

The heat transfer problem is modeled with the tissue bioheat equation. The temperature of a specific tissue due to SAR is calculated by the Pennes bioheat equation

$$\rho c \frac{\partial T}{\partial t} = \nabla \cdot (k \nabla T) + \rho Q + \rho SAR - \rho_b c_b \rho \omega \left(T - T_b \right), \tag{2.2}$$

where k is the thermal conductivity, SAR is the specific absorption rate, ω is the perfusion rate and Q is the metabolic heat generation rate. ρ is the density of the medium, ρ_b, c_b and T_b are the density, specific heat capacity and temperature of blood [28]. In this study, an assumption is made that no metabolic heat or blood perfusion occurs during the process so that the heat transfer equation can be further simplified as

$$\rho c \frac{\partial T}{\partial t} = \nabla \cdot (k \nabla T) + \rho SAR, \tag{2.3}$$

where ρ, c and k are the density, specific heat capacity, and thermal conductivity. For a specified problem, temperature increase is merely related to SAR. It is commonly accepted to use SAR values as indicators of thermal effects.

2.2 External Fixation Devices

External fixation is a surgical treatment used to stabilize bone and soft tissues at a distance from the operative or injury focus. The device is popular because it causes minimal damage to soft tissues. A typical external fixator is composed of clamps, pins, and connection bars. In terms of RF coil induced heating, it is commonly accepted that external fixation systems will cause hazardous RF heating problems in MR scan due to the length of the device and the formation of conductive loops [29]. Specifically, large metallic devices exposed to an RF field will excite strong induced currents, producing high localized energy which is deposited near the pin tips of medical devices; conductive loops will easily receive RF signals, and strongly impact the current distribution in tissue. High induced current is excited on the metallic frame. Depending on the frame shape, the RF induced heating effects will behave differently. Characterized by frame application, external fixation devices are categorized into two types: modular external fixation and circular external fixation. Both sets of external fixation devices are developed and investigated in this study.

Generic modular external fixator models were developed to study the RF heating effects on device under MRI environment [30], as shown in Figure 2.2. It is comprised of three parts: 1) two metallic blocks to represent the clamps; 2) two connection bars between the clamps; and 3) four pins which are screwed into the bones during surgery. The metallic block has the dimension of 11.4 cm $\times$ 2 cm $\times$ 3.75 cm. The distance between the centers of the two clamps is 30 cm. The pin has a diameter of 0.5 cm and a length of 16 cm.

The connection bar has a diameter of 1.1 cm and a length of 41.5 cm. The majority of the external fixator is made up of biocompatible metal, especially the part that enters human body. In EM simulations, those pins and clamps are treated as PEC. Connecting bars are made of carbon fiber to maintain the mechanical strength.

When placed in MR environment, the device is located at the point of maximum electric field according to the international standard. Numerical studies have been conducted to show the RF heating effects for modular external fixation devices in an MR environment [30]. Typically, the shortest insertion depth and largest pin spacing with the conductive bar will result in worst-case heating. In this paper, we focus on

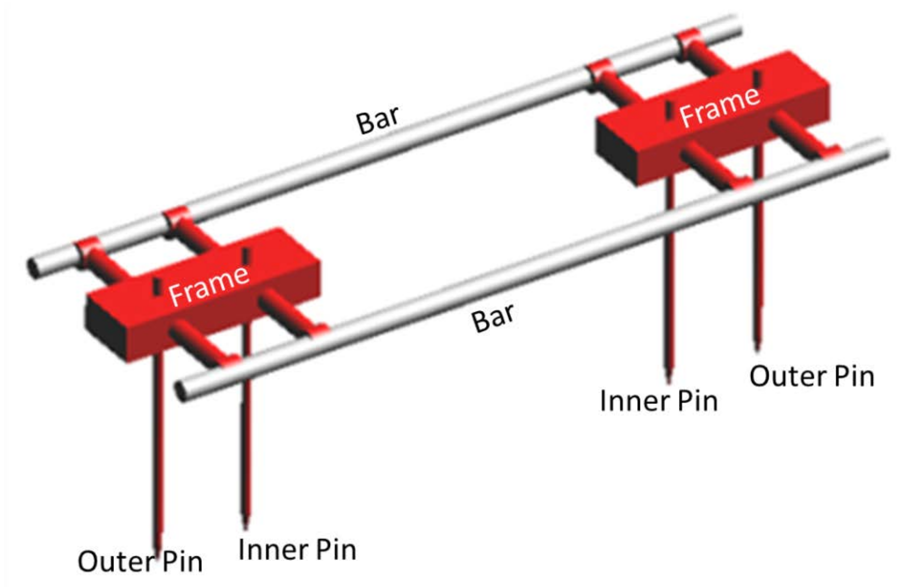

Figure 2.2. Typical structure of modular external fixation devices.

techniques to reduce RF heating effects.

Circular external fixation devices are special forms of external fixators. The main purpose of circular external fixators is the correction of complex malunions, nonunions, and deformities. There are three dominating advantages of circular external fixations over conventional modular external fixations: 1) it can reach optimal stabilization of bone fragments; 2) the frame can be simplified for reconfigurable application; 3) it enables the usage of tensioned wire structure for minimal damage to soft tissue [31]. These three fascinating features have helped circular external fixation gain increasing popularity over the years.

In our study, typical circular external fixation models are developed as in Figure 2.3. Although the actual dimension of the device may vary for different manufacturers, a typical circular external fixation device consists of the following parts: the ring structure (marked as blue part), strut (grey part), clamp (yellow part), and pin (red part). The ring has a diameter of about 200 mm. Struts are solid cylinders which are bent to connect with different holes on the ring. The vertical length of the strut is about 170 mm. Clamps are modeled as simple cylinder holders. The height may vary from 2 cm to 5 cm depending on the number and configuration of pins. The diameter of the pin is 2.5 mm with the first 6 cm sharpened as a screw. The threads on the screws are omitted in the model to reduce the geometrical complexity of the structure. For some circumstances, there is also a demand to use metal wires. The tensioned wires are modeled as thin wire with 2mm diameter. In EM modeling, all components are set to PEC.

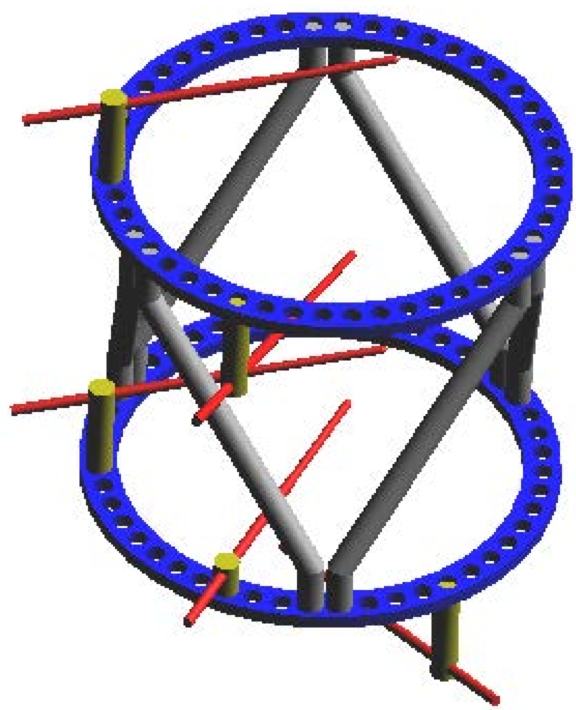

Figure 2.3. Typical structure of circular external fixation devices.

There is a wide variety of circular external fixation devices, i.e. number, position, insertion depth and/or angle for pin/wires, clamp size, size of ring frame, and strut shape. The generic circular external fixation devices developed in this study are also capable of adjusting these parameters, which enhance the feasibility of numerical studies.

2.3 Numerical Modeling of MRI RF Environment

To understand the mechanism of MRI RF heating, published literature has built mathematical models based on a coupled electromagnetic and heat transfer problem [27]. Because of the direct relationship between SAR and temperature increase, SAR is simply used as an indicator of RF heating. For simple geometries, the RF coil induced heating evaluation can be calculated analytically. The MR RF environment is, however, too complicated to derive an analytic solution. Specific EM configurations are applied to the MRI RF coil, while the ASTM phantom, external fixation devices and the human body are treated as inhomogeneous media. Thus in this study, numerical simulation are employed for MRI RF heating evaluation.

2.3.1 MRI RF Environment Modeling using FDTD Method

SEMCAD X, a commercial 3-D full wave simulation environment based on the finite-difference time-domain (FDTD) method, is used in our simulation study. The software can provide 3-D solid modeling for medical devices and solutions for coupled EM-thermal simulations. The post-processing portion of this simulator is robust enough to handle massive computation tasks. The simulator is interfaced with GPU acceleration, which can further reduce run time by a factor of at least 25. In simulation studies, SEMCAD X is used to model the interactions between MRI-related RF signals and patients or phantom loaded with medical devices. The following models are developed to represent the RF environment in a real clinical case.

Birdcage can achieve near optimal RF field (B_1) homogeneity and signal-to-noise ratio (SNR) among all different kinds of RF coils [32]. A physical birdcage coil is usually difficult to model because it requires the detailed information of a specific birdcage coil design. The shapes, sizes and the tuning capacitors vary from one MR system to another, and the manufacturers are reluctant to release the data due to the proprietary rights to the commercial MR scanner. In addition, the multi-component structure of physical birdcage coil model will also increase the complexity of the numerical model, and thus increase the simulation time. A simplified birdcage coil model is proposed which has been shown to be computationally equivalent to a physical coil model [33].

A 1.5 T high-pass birdcage coil is designed to represent real MRI RF coil in simulation. As shown in Figure 2.4, the diameter of the RF coil is 63 cm and the height of the RF coil is 65 cm. The eight parallel red lines (rungs) are current sources. The blue lines (end rings) on the top and bottom of the RF coils are tuning capacitors. To generate a circular polarized electromagnetic field inside the coil, all current sources have a uniform magnitude. The phase difference between current sources on adjacent rungs is $2\pi/N$, where N is the total number of rungs (N = 8 in our case). All tuning capacitors were adjusted so that the coil is resonant at 64 MHz.

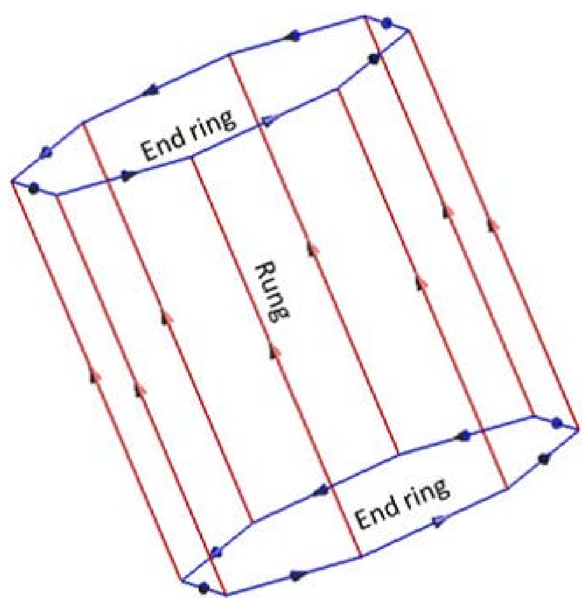

Figure 2.4. Structure of MRI RF coil in simulation.

Since the birdcage model is composed of infinitesimally thin wires instead of actual perfect electric conductor (PEC) wire with finite thickness, there is no practical method for solving an analytical formula to calculate capacitor value. A three-step tuning process is proposed [34]: 1) set an initial capacitance value for all capacitors on end rings and add a broadband pulse signal on one single rung. The other seven rungs are modeled as zero ohm resistors. 2) After broadband simulation, the power spectrum is extracted. If the second highest resonant frequency is not at 64 MHz, the capacitance needs to be adjusted. 3) After three to five broadband simulations, the second highest resonant frequency needs to be located at 64 MHz.

The magnetic field distribution at the center plane of the RF coil is shown in Figure 2.5. The magnetic field is uniformly distributed within the birdcage. It can be concluded that the RF coil is operating at the correct resonant mode. The simplified coil will be used for MRI RF heating simulation studies.

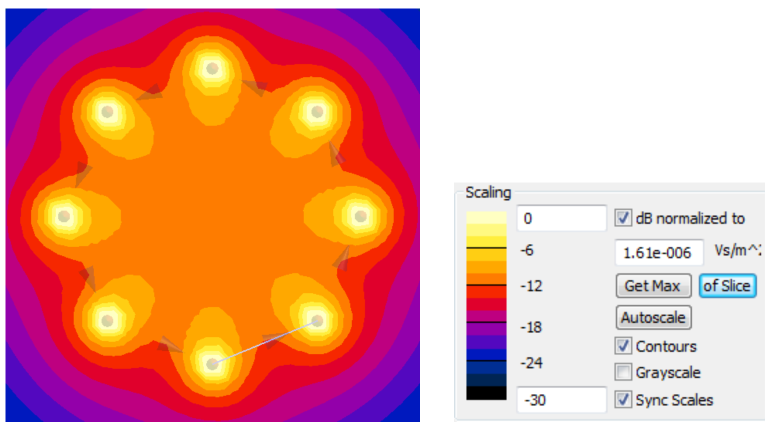

Figure 2.5. B field homogeneity of tuned MRI RF coil.

2.3.2 ASTM Phantom/Virtual Family

An ASTM standard phantom is filled with saline gel. The phantom is of the dimensions shown in Figure 2.6. The trunk part is about 42 cm wide and 60 cm high. The head is about 15 cm wide and 27 cm high. Although the thickness of the phantom gel is 9 cm, it is also possible to increase the depth of the gel material in order to test larger devices. Phantom gelled-saline material should match the average conductivity of the human body at body temperature. The dielectric constant is close to the average dielectric constant of the human body. For the simulations, the dielectric constant is set to 80.38, while the conductivity is set to 0.448 S/m. The relative permittivity of the container is 3.7, and the conductivity is zero since it is made up of non-metallic materials.

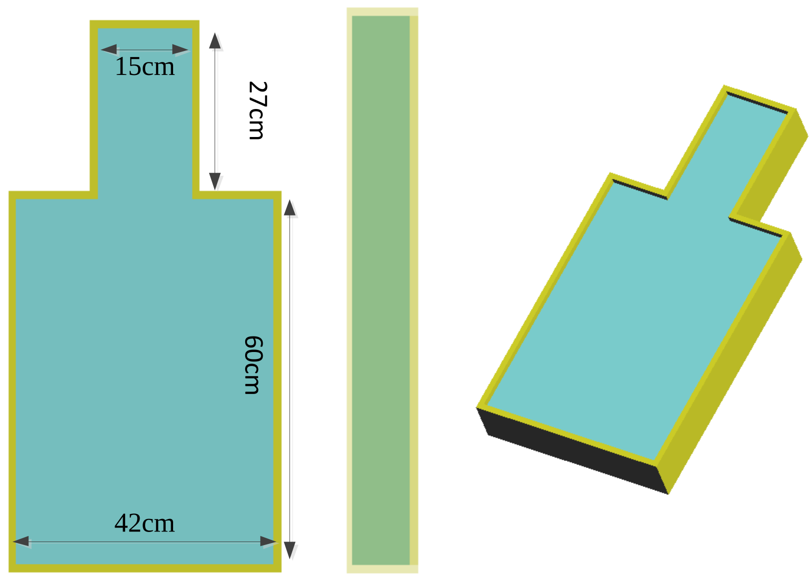

Figure 2.6. Dimension of ASTM phantom in simulation.

During the testing process, the ASTM phantom should be placed inside the RF coil as shown in Figure 2.7. The center of the trunk portion coincides with the center of the RF coil. Electromagnetic simulations are performed to determine the electric field distribution within the ASTM phantom. As shown in Figure 2.8, the maximum electric field locations are near the side walls of the phantom as indicated by Nordbeck et al. [33], along the center for both the horizontal and the vertical directions. According to international standard ASTM-F2182 [21], testing devices should be placed at the location of maximum electric field. To comply with the standard, devices should be placed in locations that receive maximum RF energy exposure. In this study, the spacing between the devices and the side wall is 2 cm for all simulations. With this placement, the EM study can be executed.

There is also a possibility that external fixation devices are not practical to be placed in ASTM phantom, e.g., circular external fixation. The insertion pins must

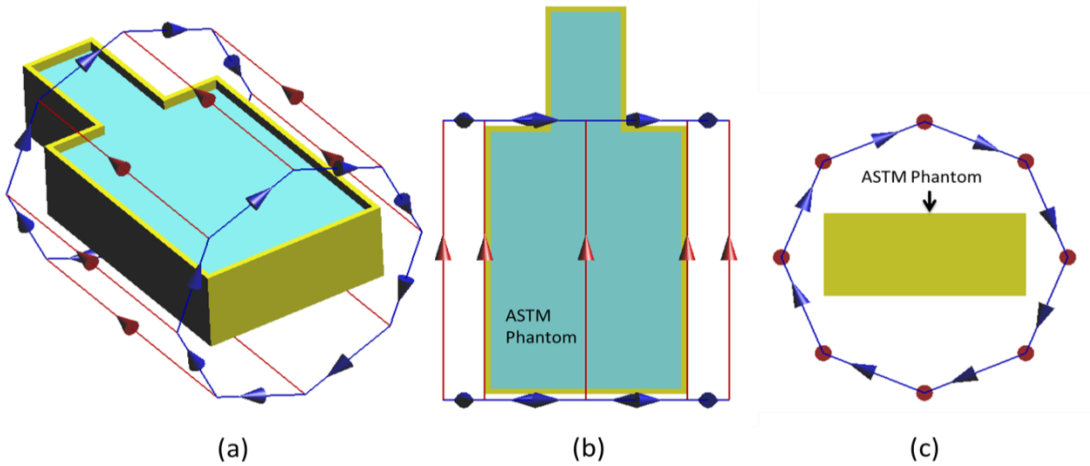

Figure 2.7. Simulation setup to determine the maximum electric field location inside the ASTM heating phantom.

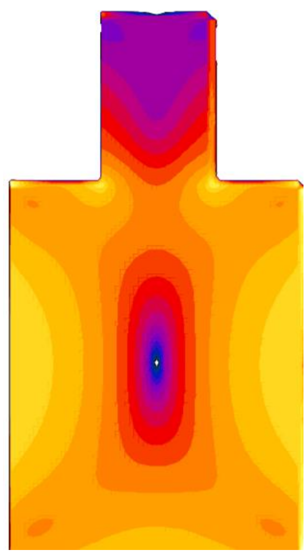

Figure 2.8. The electric field distribution for 1.5-T/64-MHz MR systems in ASTM heating phantom.

impinge into the human body from various directions. In such cases, a virtual family model will be used. The virtual family is a set of highly detailed, anatomically correct whole-body models, including segmentation of approximately 80 high-resolution organs and tissues [35]. It contains five different human models: obese male (Fats), adult male (Duke), adult female (Ella), girl (Billie), and boy (Thelonius) as shown in Figure 2.9. In this study, DUKE, a 34-year old adult male model is chosen for RF heating evaluation. The Duke model was developed based on several high resolution magnetic resonance (MR) images of a healthy 34 year old volunteer (height: 1.77m, weight: 72.4Kg). Seventy seven different tissue types were distinguished during the segmentation. The electromagnetic properties of each tissue can be obtained from ITIS foundation database.

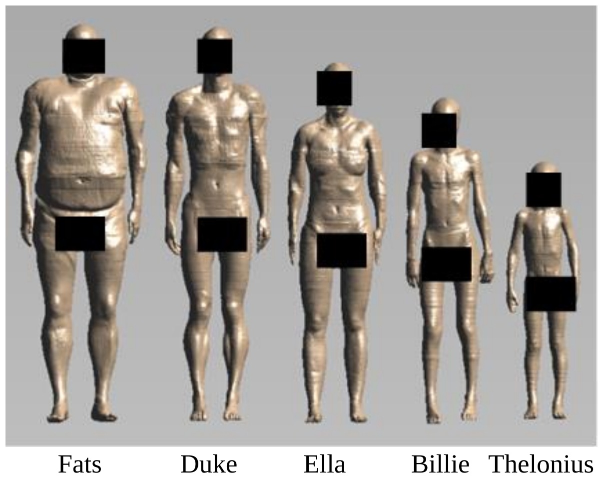

Figure 2.9. Five human models in virtual family project.

2.4 Experiment Measurement

2.4.1 ASTM Testing Procedure

According to international standard ASTM F2182, the device to be tested is placed in a phantom material that simulates the electrical and thermal properties of the human body. The device is placed at a location with well characterized exposure conditions. The local SAR is assessed to characterize the exposure conditions at that location. The phantom material is a gelled saline consisting of a saline solution and a gelling agent. Temperature probes are placed at locations where the induced device heating is expected to be the greatest (this may require pilot experiments to determine the proper placement of the temperature probes). The phantom is placed in an MR system or an apparatus that reproduces the RF field of such an MR system. An RF field producing a sufficient whole body averaged SAR of about 2 W/kg averaged over the volume of the phantom is applied for approximately 15 min, or other duration that is sufficient to characterize the temperature rise and the local SAR.

The test procedure is divided into two steps. In Step 1, the temperature rise on or near the implant at several locations is measured using fiber-optic thermometry probes (or equivalent technology) during approximately 15 min of RF application. Temperature rise is also measured at a reference location during Step 1. In Step 2, the implant is removed and the same RF application is repeated while the temperature measurements are obtained at the same probe locations as in Step 1. All measurements are done with the implant holders in place. The local SAR is calculated from the temperature measurements for each probe location, including the reference location. The local SAR value at the temperature reference probe is used to verify that the same RF exposure conditions are applied during Steps 1 and 2.

To carry out such an experiment, the MRI RF exposure system, phantom material and temperature probe as mentioned above are the basic requirements of MRI RF coil induced heating effects assessment. The following sections specify each part in detail and the examination of each separate portion guarantees the correctness of the experimental measurement.

2.4.2 MRI RF Coil with Shielding Room

Zurich MedTech (ZMT) Medical Implant Test System (MITS) is deployed to simulate high precision worst-case RF incident fields as commercial 1.5 T MR scanners in our experiment study (Figure 2.10). MITS1.5 is compatible with the latest draft of the ISO/IEC Joint Working Group (JWG) Technical Specification. It can provide quadrature drive, precise frequency and phase control, and automatic tuning function.

By adjusting the initial input parameters on the MITS1.5 system, the pulse shape

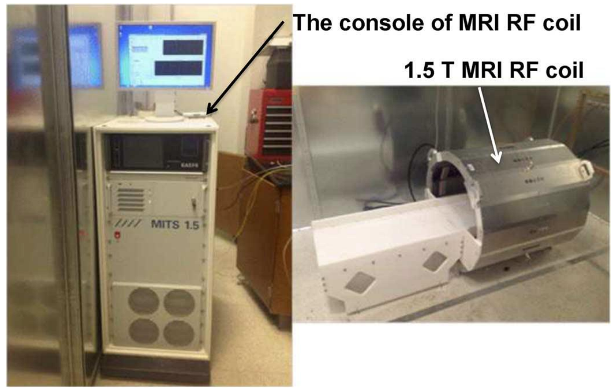

Figure 2.10. ZMT MITS 1.5T MRI RF coil system and MR shielding room.

as well as the field polarization can be obtained inside the RF coil. A circular polarized field is formed using an IQ feed, where the phase difference between Feed I and Feed Q is 90°.

In addition, to block out any interference with surrounding areas or radio waves, an ETS-Lindgren MR shielding room is built outside the RF coil. This shielding system provides RF attenuation levels greater than 100 dB up to MR frequencies of 400 MHz (9.4 Tesla).

2.4.3 ASTM Phantom

As mentioned in ASTM F2182, the measurement of RF-induced heating requires the implant to be placed in a phantom that simulates the electrical and thermal properties of the human body [21]. To carry out temperature measurements, an ASTM standard phantom is loaded into the MRI RF coil. The gelled saline, which consists of sodium chloride and polyacrylic acid, is made to meet the criteria for the purpose of simulating human tissue. The conductivity of the gelled saline shall be 0.47 S/m at room temperature. The heat capacity is around 4150 $J \cdot Kg^{-1} \cdot {}^{\circ}C^{-1}$ and the relative electric permittivity shall be 80 at the test frequency. The rectangular phantom with exact dimension as described in ASTM F2182 standard and is filled with saline gel to provide sufficient viscosity to prevent bulk transport or convection currents (Figure 2.11). The phantom is placed inside the RF coil such that the center of torso is aligned with the center of the RF coil. Implanted devices are located at maximum electric field location, which is 2 cm from the inner side wall indicated by simulation. This location has been recognized as the worst-case heating conditions in MRI heating tests.

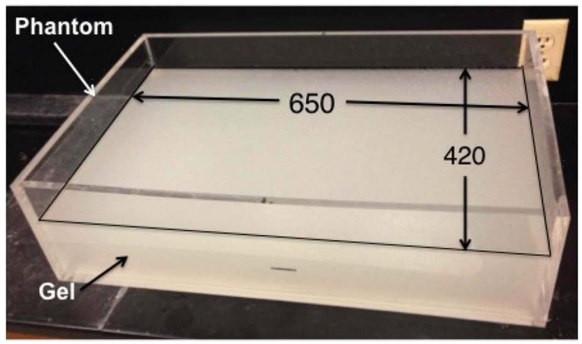

Figure 2.11. Dimension of ASTM phantom in experiment.

2.4.4 Temperature Probe/H field Probe

Depending on the requirement of RF heating test, the RF exposure time should be either 6 minutes or 15 minutes with one minute of data collection before and after the test sequence. Optic fiber temperature probes (Neoptix) are therefore used in the testing procedure. As shown in Figure 2.12, this temperature probe complies with ASTM D2413 and D149 standards [36, 37]. During data collection, the measurement end of the probe is attached to the medical device. Temperature recording platform is embedded with the probe system so that there is no need to do reading manually.

The H field probe is embedded in the MITS 1.5 system as shown in Figure 2.13. Usually the probe is used before thermal testing to ensure the birdcage is working at proper frequency. The probe can measure the vector H field, which will be displayed on the MITS 1.5 system. The amplitude can be calculated and is displayed on the interface.

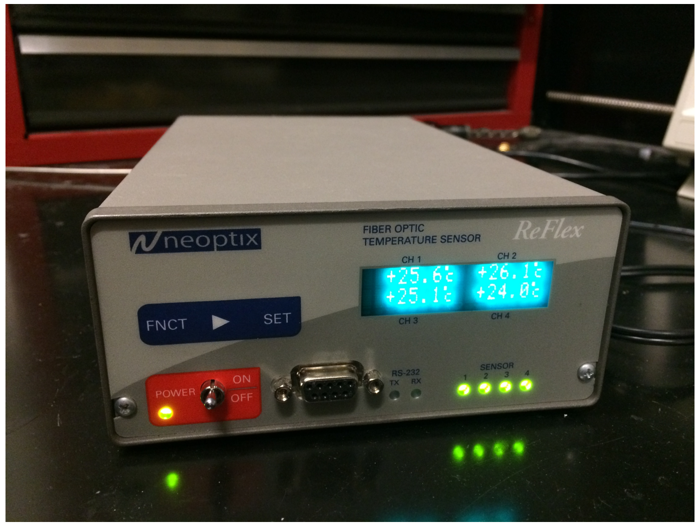

Figure 2.12. Temperature probe with data acquisition unit.

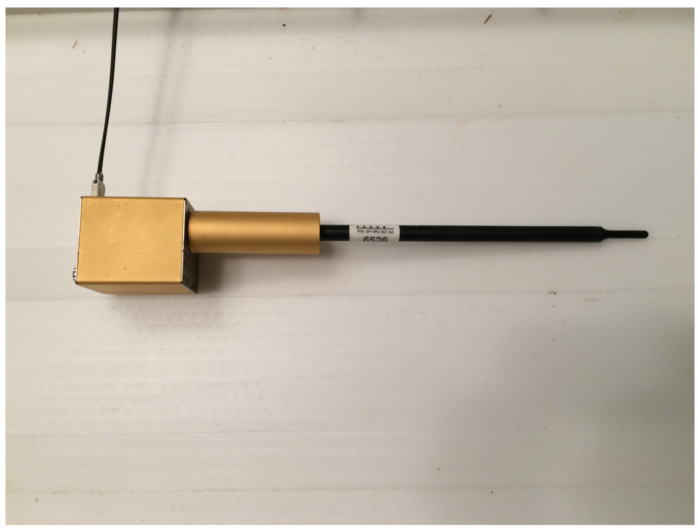

Figure 2.13. H field probe

Chapter 3

MRI RF Heating Reduction for Modular External Fixation

Previous studies have shown that the shortest insertion depth and largest pin spacing with the conductive bar will result in worst-case heating for modular external fixation devices [20]. The modular external fixation device usually has severe heating effects due to the length of the conductive components of the device. Based on the worst-case external fixation configuration, the method of using absorption material was shown to be effective to reduce the MRI RF heating.

3.1 Background

During an MRI scan, induced currents are generated on the surface of metallic parts. The propagation of induced energy that flow towards the pin can generate large local energy deposition at the tip of the screws. If the current is electrically isolated and thus prevented from flowing through the pin into human body, it can potentially reduce the heating effect. A solution to reduce RF-induced heating for external fixation devices is studied. The effectiveness of using insulating layers between the clamp and the pin is limited due to the capacitive coupling effects at 64 MHz [26]. As an alternative to the previous method, a novel and effective solution of using RF absorption material is proposed to alter the electric field distribution near and on the external fixation devices. The material can absorb part of the RF-induced energy on the device frame, and thus reduce the heating effects in human body. In addition, the material can also change the induced current distribution on the device so that less energy will be coupled into the human subjects. This provides a potential solution to the design of MRI RF-compatible external fixation devices.

It has been shown that the induced heating on the generic external fixation device comes from the induced energy generated on the bar as well as the clamps. These induced energies can be coupled onto the device pins and propagate towards the tips of the pins. Using insulating material is considered a good way to block the energy flow. However, the capability of insulated layer for RF heat reduction is limited due to capacitive coupling. Instead of energy blocking using insulating material, the absorption material is able to absorb such induced energies between the bar and clamp, and the clamp and pins [38]. Such absorption material can also change the current distribution and minimize the current flow toward the pin tips.

The absorption material has been used in anechoic chamber designs where the absorber on the wall of the chamber is used to absorb the impinging wave [39]. The absorber should be lossy so that the reflected EM waves can be eliminated. For single frequency RF heating evaluation, the absorption characteristics can be characterized by electrical conductivity. In our study, conductivity ranging from 10^{-4} to 10^{3} S/m is investigated.

3.2 Simulation Study

To evaluate the RF-induced heating effect on such a device, the device is placed at a location in the ASTM phantom where high incident tangential electric field is observed (see Figure 3.1). Four tubular structures with 5 mm inner diameter and 7 mm outer diameter are placed between the clamps and pins as shown in Figure 3.2. As mentioned earlier, the purpose of these four tubular structures is to absorb the partial energy induced on the device and change the current flow from the device toward the pin tips. Electrical properties for all materials used in this investigation are shown in Table 3.1.

To study the effect of different absorption materials on induced RF heating of the device, five categories of materials with different absorption characteristics are

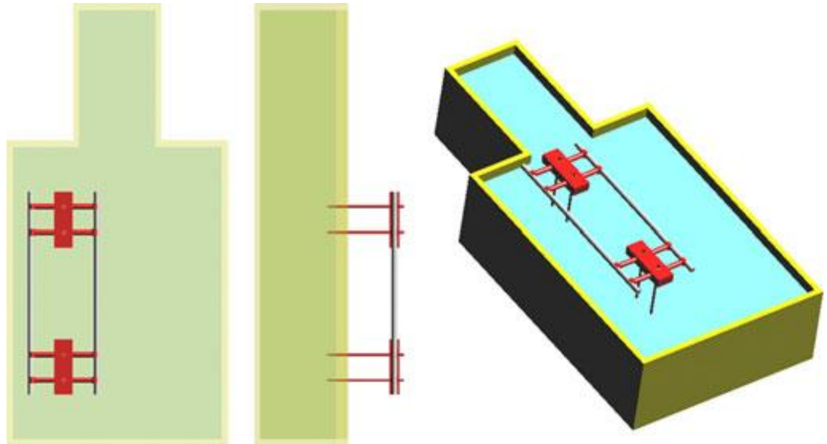

Figure 3.1. Relative location of modular external fixation and ASTM phantom.

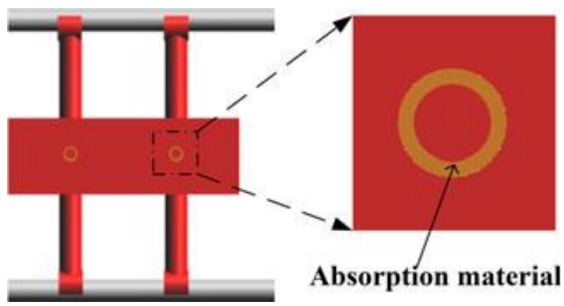

Figure 3.2. Absorption material geometry on modular external fixation devices.

Table 3.1. Electrical properties of the material

	Relative Permittivity	Electrical conductivity(S/m)
ASTM Phantom Gel	80.38	0.448
ASTM Phantom Shell	3.7	0
Bar (Carbon fiber)	10	5700000
Device Clamp, Pin	PEC	PEC

examined. Each category has its individual dielectric constant ε_r = 2, 3, 5, 7, 9, and the electrical conductivity varies from 10^4 to 10^3 S/m. The electromagnetic properties of the device bar, ASTM phantom gel, ASTM phantom shell are shown in Table 3.1. Once the simulation was complete, 1g-averaged SAR along device pins were calculated for further analysis.

The side view of a typical simulation result is shown in Figure 3.3. For simplicity, the four pins are named as pin 1, pin 2, pin 3, and pin 4 from right to left. Two examples are chosen to illustrate typical SAR patterns.

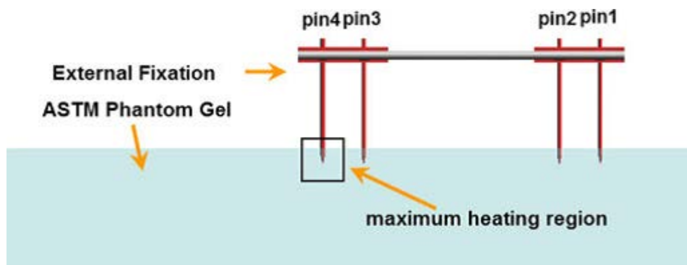

Figure 3.3. Side view of external fixation geometry.

The first example is shown in Figure 3.4(a). The absorption material has a dielectric constant $\varepsilon_r = 9$ and an electrical conductivity $\sigma = 0$ S/m. The maximum heating location occurs at the tips of the pins. The red square in this figure denotes the global maximum SAR location. The SAR along a horizontal line across the pin tip (the green line in Figure 3.4(a)) is shown in Figure 3.5. It is observed that the points near the outer pins (pin 1 and pin 4) have a larger SAR value than at the inner pins (pin 2 and pin 3). The highest SAR value is 1160 W/kg, which is located at tip of pin 4.

In the second example, the absorption material has $\varepsilon_r = 9$ and $\sigma = 0.1$ S/m; the SAR pattern is shown in Figure 3.4(b). The SAR pattern inside the phantom gel is similar as to that of the first example, but the peak SAR near the tips is significantly reduced. The global maximum SAR occurs at the layer of absorption materials between the clamp and pin, as denoted by a red square. The SAR value along the same green line across the pin tip (the green line in Figure 3.4(b)) is plotted in Figure 3.5. While the global maximum SAR is 905 W/kg, the maximum SAR inside the phantom is about 470 W/kg. Since the region of interest is confined to the interior of the phantom, the maximum SAR is reduced by nearly 60% compared to using pure insulating material.

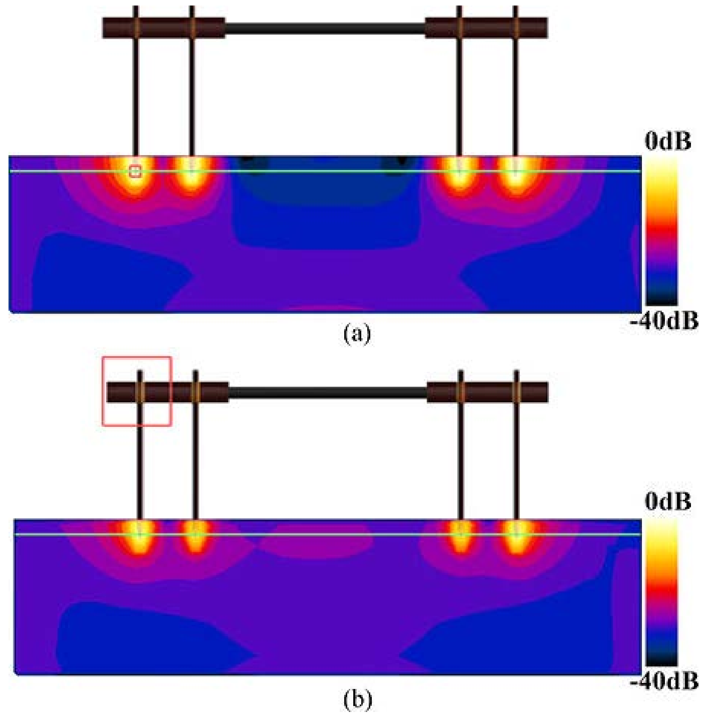

Figure 3.4. The 1g-averaged SAR distribution at cross-section plane of pins for case a) $\varepsilon_r = 9$, $\sigma = 0$ and b) $\varepsilon_r = 9$, $\sigma = 0.1$ S/m. 0 dB refers to 1160 W/kg.

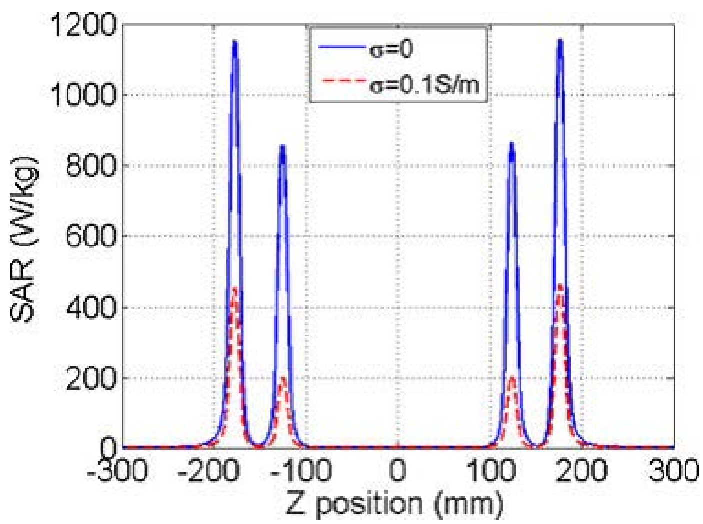

Figure 3.5. SAR along green line that across the tips of pins ($\varepsilon_r = 9$).

The field distributions in Figure 3.4 are normalized to 1160 W/kg, i.e., 0 dB denotes 1160 W/kg. For case $\varepsilon_r = 9$ and $\sigma = 0.1$ S/m, the maximum SAR at the tip of the pin is smaller than the case $\varepsilon_r = 9$, $\sigma = 0$ S/m. This implies that materials with absorption characteristics could be capable of reducing heating effects.

As the conductivity of the material changes, the external fixation device will exhibit a different thermal behavior. For $\varepsilon_r = 9$, the relationship between conductivity and the maximum SAR near the pin is plotted in Figure 3.6. There is a valley in the middle range (10^{-2} to 10^{0} S/m). The minimum value for maximum SAR at pin is 450 W/kg. When conductivity becomes lower (10^{-4} to 10^{-3} S/m) or higher (10^{1} to 10^{3} S/m), the maximum SAR increases to 1160 W/kg and 645 W/kg respectively. It should be pointed out that the optimal conductivity is acquired based on the thickness of the 1mm lossy ring at 64 MHz. This optimal conductivity could change as a function of ring thickness.

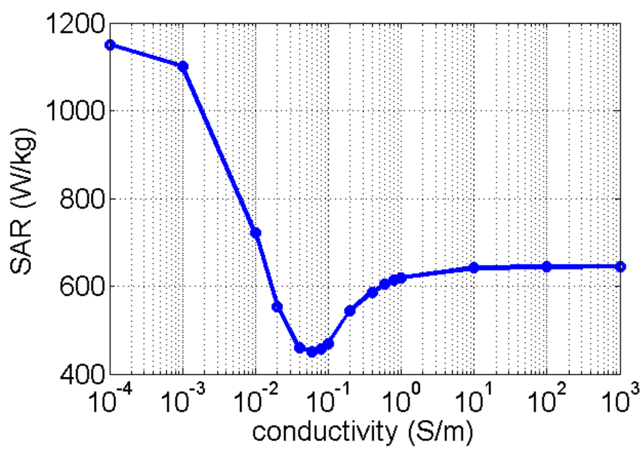

Figure 3.6. Maximum 1g-averaged SAR near pin vs. conductivity for $\varepsilon_r = 9$.

For various dielectric constants, the relationship between conductivity and the maximum SAR near a pin is plotted in Figure 3.7. As the conductivity of the material changes, the external fixation device will exhibit different thermal behavior. There is a minimum point in the middle range ($10^{-2} - 10^{0}$ S/m) for each curve as shown in Figure 3.7. When conductivity decreases ($10^{-4} - 10^{-3}$ S/m) or increases ($10^{1} - 10^{3}$ S/m), the maximum SAR value goes up. It should be pointed out that based on the thickness of 1-mm lossy tubes at 64 MHz, there is an optimal conductivity value that can provide maximum heating reduction for external fixation devices.

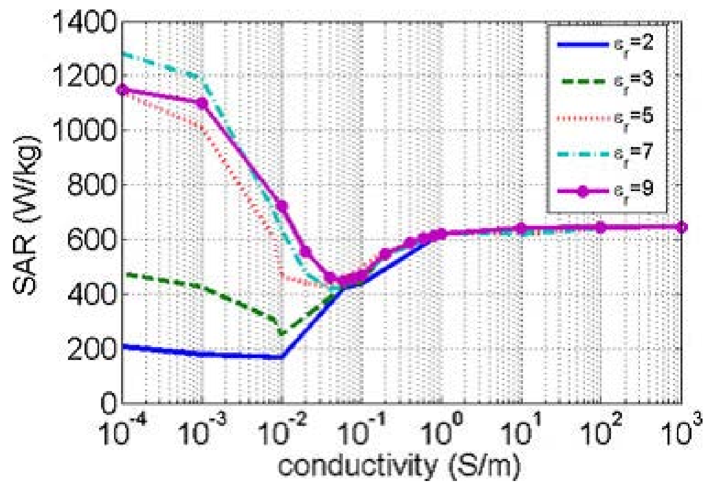

Figure 3.7. Maximum 1g-averaged SAR near pin versus conductivity for different dielectric.

3.3 Experimental Validation

In addition to the numerical investigation, experimental studies of using absorbing materials for RF heating reduction were carried out. A commercially available external fixation device, provided by Orthofix, Italy, is being analyzed through a series of lab work. During experimentation, the ASTM Phantom loaded with external fixation device is tested using a ZMT Medical Implant Test System MRI RF safety evaluation system. The ETS-Lindgren MRI shielding room is deployed to prevent leakage of RF field. Up to four fiber-optical temperature probes were used to measure the temperature rises near the device pins. The temperature recording platform is embedded with a probe system to allow automatic readings.

According to standard ASTM F2182-11a [21], the device is placed on top of the phantom at isocenter location and about $2-3$ cm from the side (see Figure 3.8). The phantom with device is exposed to MRI through a birdcage body coil for 15 min. The temperature is recorded 1 min before the MRI coil is turned on and continuously recorded for 2 min after MRI system powering off (totally 18 min). The data are exported to a computer for analysis.

(a)top view

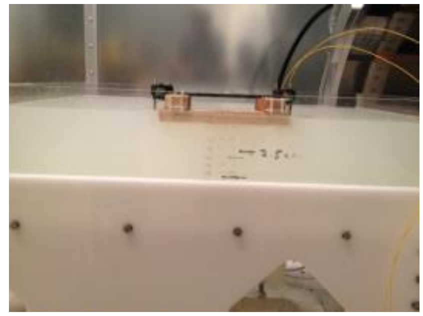

(b)side view

(c)front view

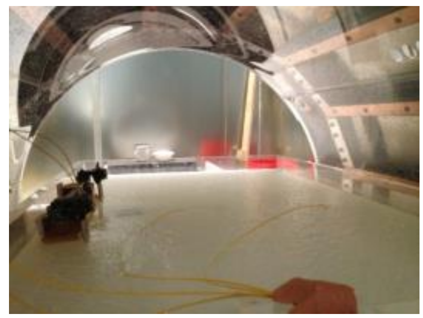

(d)placed into ASTM phantom

Figure 3.8. Experimental setup for modular external fixation and ASTM phantom. (a) top view. (b) side view. (c) front view. (d) placed into ASTM phantom.

The absorption material, provided by Molex Inc., Lisle, IL, USA, is shown in Figure 3.9. Provided by the company, the electrical properties changed with frequency can be found in Figure 3.10. At 64 MHz, the relative permittivity is 136.1, while the conductivity is 0.0095 S/m. For testing, the material is wrapped at the connecting part between device components with 1 mm thickness (see Figure 3.9). Absorbing materials are used at two connection locations. One is used between clamps and pins, whereas the other one is used between clamps and bars [shown in Figure 3.9(c) and (d)]. For convenience, these two configurations are named “pin cover” and “bar cover”, respectively. Four cases are measured in the experimental study, which are listed as follows:

1) no cover for device (no cover);

2) cover between pin and clamp (pin cover);

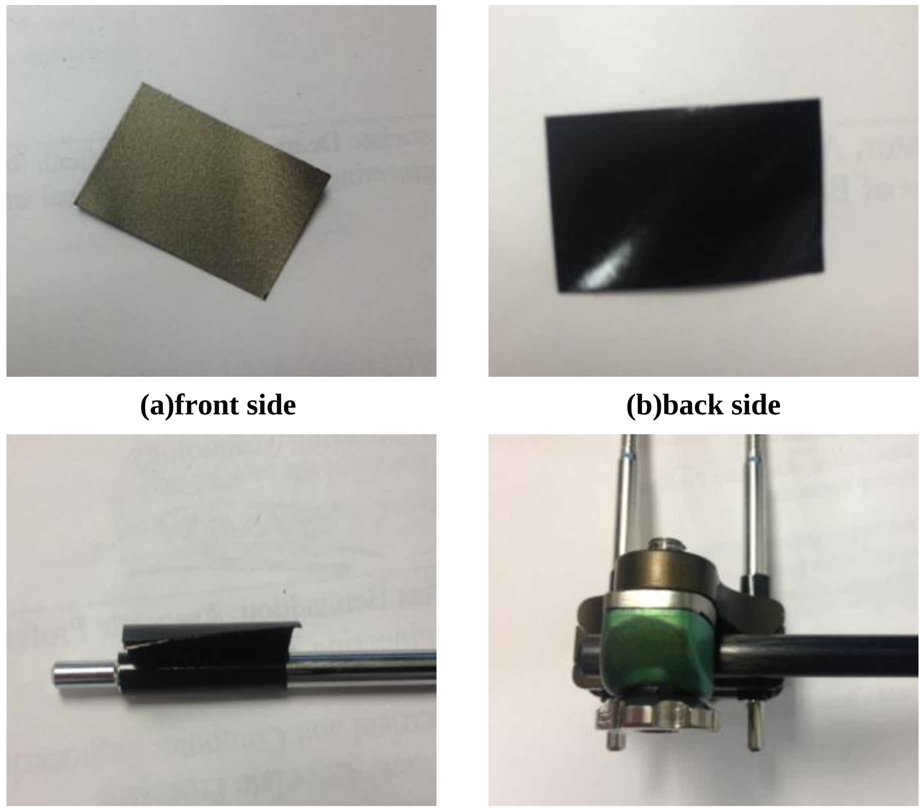

(a)front side **(b)back side**

(c)wrap into pin **(d)placed into clamp**

Figure 3.9. Setup for absorption material. (a) front side. (b) back side. (c) wrap into pin. (d) placed into clamp.

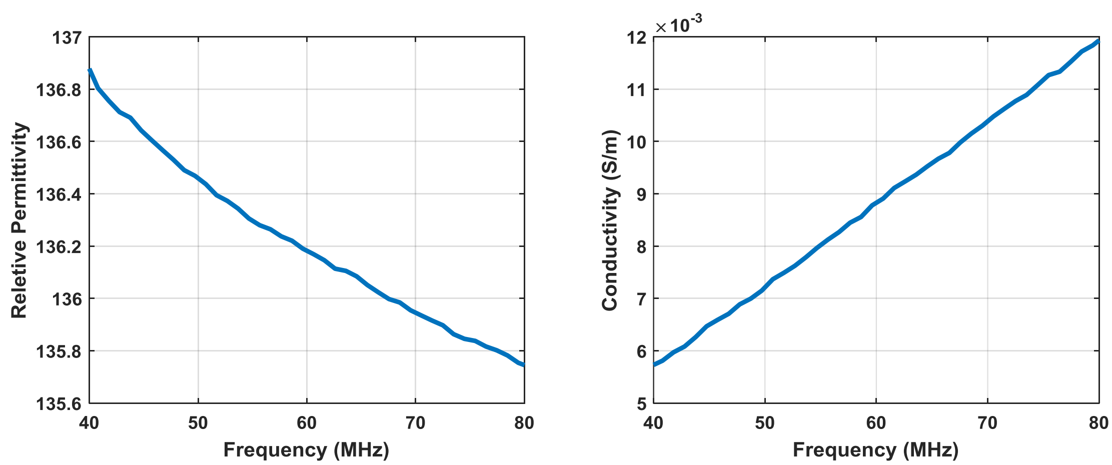

Figure 3.10. Permittivity and conductivity of the testing absorption material change with frequency.

3) cover between clamp and bar (bar cover);

4) cover on both sides (both cover).

The temperature increase measurements for all four cases are plotted in Figure 3.11. The device with no cover is observed to have the highest temperature increase, of about 4.2°C. As the pin cover or bar cover are applied to the external fixation device, the heating effects become less significant (at 3.3 and 2.6°C, respectively). In the case of a device with cover on both sides, the temperature rise is as low as 1.7°C.

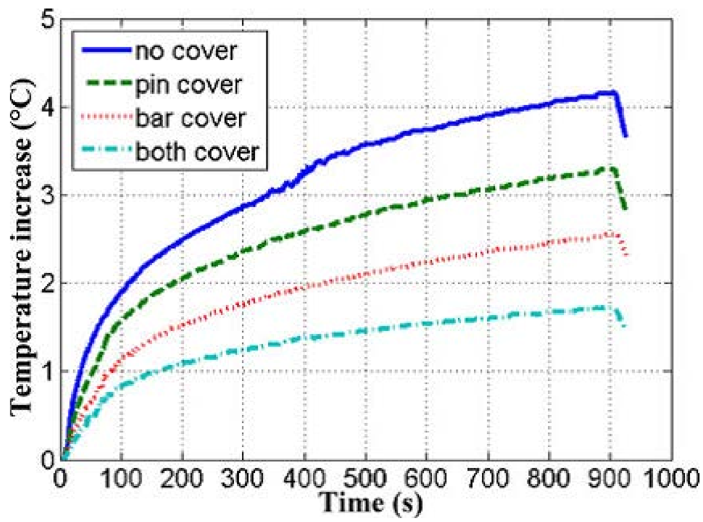

Figure 3.11. Temperature increase measurement for all four cases.

3.4 Discussion on Using Absorption Material

The analysis above can be summarized as follows: by using different absorption material, the RF-induced heating effects may have different behavior. If properly chosen, the absorption material can reduce the RF-induced heating effect in human body. Experimental results reveal the potential to achieve lower RF heating effect using absorption material as well.

The reason why a very high or very low conductivity results in a higher SAR at pin can be explained by the definition of SAR. SAR is defined as $\sigma E^2/2\rho$. The induced energy for the external fixation can be assumed relatively invariant. When conductivity is very close to zero, i.e., σ approaches zero, the dissipated energy in the absorption material is zero. On the other hand, when the conductivity becomes high enough, the material acts like a PEC, which means the electric field inside the material is zero. Because there is no power dissipation in the absorption material, all energy enters into the phantom gel and thus higher SAR is expected in the gel. When conductivity is in the middle range (10^{-2} to 10^{0} S/m), neither conductivity nor E-field approaches to zero. The power consumption in the material reaches the maximum. Energy that can propagate in the phantom becomes lower.

Table 3.2. Optimum conductivity for different dielectric constants

Relative Permittivity	Optimum Conductivity (S/m)	Loss Tangent
2	0.006	0.84
3	0.01	0.93
5	0.015	0.84
7	0.04	1.61
9	0.06	1.87

When the minimum value for max SAR near pin occurs, the corresponding conductivity is called optimum conductivity. Table 3.2 lists the optimum conductivity for different dielectric constants. Loss tangent is also provided. When the loss tangent is near 1 or 2, the minimum peak SAR near the pin can be achieved.

3.5 RSM Strategy for Optimum Absorption Material

During the selection of absorption material to minimize induced RF heating, it is not possible to test all combinations of material parameters such as permittivity, permeability, and conductivity. One of the common approaches is to analyze One-Variable-At-a-Time (OVAT), i.e. a single variable is varied at a time while other variables are kept fixed. This type of searching requires large resources to obtain a limited amount of information about the process [40]. For multi-variable optimization, the OVAT method is inefficient and sometimes unreliable. To overcome this limitation, a statistical method called Response Surface Methodology (RSM) is used here. This method has been widely accepted and applied with a number of successful applications in many US and European designs over the last 25 years [41]. In our study, RSM is used to search for the optimal parameters for the absorption material for a specific device. Using an RSM optimization process can minimize the device-induced heating. This allows one to obtain device-specific absorption materials for maximum heating reduction.

In the previous section, the effectiveness of using absorption material to reduce MRI RF heating effect has been shown through both simulation results and experimental validations. It can significantly reduce the RF heating inside phantom body when electromagnetic properties of absorption material are properly chosen. In terms of resonance, the frequency, permittivity, conductivity, permeability and geometry structure would be factors in this. Since we focus on the 1.5T MRI system, the frequency is fixed at 64 MHz. For clinical usage of medical devices, the geometry structure is hardly changed. In this section, we studied and evaluated the searching strategy to find an optimum set of permittivity, conductivity and permeability values that will minimize the RF heating effects by applying RSM.

3.5.1 Response Surface Methodology

RSM is a collection of statistical and mathematical techniques useful for developing, improving, and optimizing processes [42]. In our case, we expect to find appropriate permittivity (ε), conductivity (σ) and permeability (μ) to minimize the maximum SAR (S). The maximum SAR is considered to be a function of permittivity, conductivity and permeability

$$S = f\left(\varepsilon, \sigma, \mu\right) + \theta, \tag{3.1}$$

where θ represents the noise or error in response S. In most cases, those parameters may have constraints due to their physical limits. If we denote the expected SAR value as

$$E(S) = f(\varepsilon, \sigma, \mu) = \eta, \tag{3.2}$$

then the surface represented by η is called the response surface.

Because of the complexity of numerical methods in electromagnetics, the mathematical relationship between the response and the factors is unknown. A first-order approximating model is used in the optimization process

$$\eta = \beta_0 + \beta_1\varepsilon + \beta_2\sigma + \beta_3\mu, \tag{3.3}$$

where $\beta_1, \beta_2, \beta_3$ is called the sensitivity of factor ε, σ, μ to the response S, respectively. It should be noted that sensitivity is changed with different choices of factors. These coefficients are determined by 2-level factorial design: changing one factor slightly while others remain the same, the rate of change is considered the sensitivity. This approximation is valid within a small range of factors.

RSM is a sequential procedure. The initial guess is often far away from the optimum point. Modeled as a first-order approximation, 2-level factorial design is conducted to test the sensitivity of each factor. The next guess point goes along the path of steepest descent. It is crucial to determine the step length after knowing the direction of steepest descent. A flow chart detailing the computational process is shown in Figure 3.12. The optimization strategy is proposed as the following:

1) Initial guess and get response

2) Determine sensitivity of each factor, the steepest descent direction is obtained

3) Properly choose a step length, get the next guess

4) Use the new guess to get response, judge if the response is better than previous guess. If no, go to 3) and adjust step length. If yes, go to 5).

5) Determine sensitivity of each factor for the new guess, judge if the sensitivity

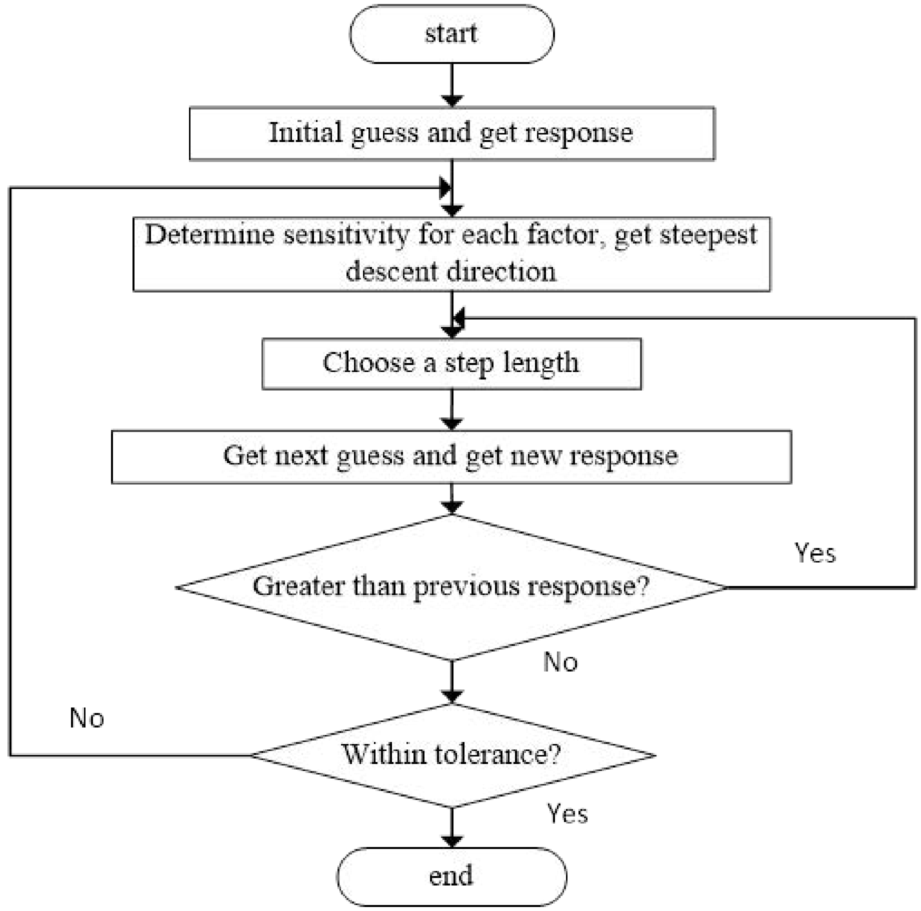

Figure 3.12. Flowchart for optimization process based on RSM.

is within tolerance level. If no, get steepest descent direction and go to 3). If yes, terminate.

3.5.2 RSM Scheme Implementation

The constraints of our case are set to: $2 \leq \varepsilon_r \leq 9$, $0 \leq \sigma \leq 0.1$ S/m,$0 \leq \mu_r \leq 2$. The initial guess is randomly chosen as $\varepsilon_r = 7$, $\sigma = 0.001$ S/m, $\mu_r = 1$. By factorial design, additional three sets of parameters are simulated. The results are shown in Table 3.3.

The result of the factorial design above shows that changing permittivity and permeability will not affect the maximum SAR in this process. Thus for the next step, only the conductivity is adjusted. The step length is chosen by empirical experience. The next guess point is: $\varepsilon_r = 7$, $\sigma = 0.01$ S/m, $\mu_r = 1$. Simulation results show the

Table 3.3. Factorial design for initial guess

ε_r	σ (S/m)	μ_r	S
7	1e-3	1	1190
6.9	1e-3	1	1190
7	1.1e-3	1	1180
7	1e-3	1.1	1190

maximum SAR inside phantom decrease to 649 W/kg, so further sensitivity analysis is performed to determine guess point for the next step.

Figure 3.13 shows the results of this RSM procedure. For the first few steps, the step lengths are chosen relatively large, whereas the step lengths for last steps are small. Changing the permeability of the material hardly impacts the RF heating effect since permeability of all guess points is always around 1.

The responses vs. passes are plotted in Figure 3.14. After 10 passes, the maximum SAR has decreased to a small range and only oscillates slightly. It is concluded that minimum heating is achieved by choosing $\varepsilon_r = 2.14$, $\sigma = 0.007$ S/m, $\mu_r = 1$. The maximum SAR is about 172 W/kg.

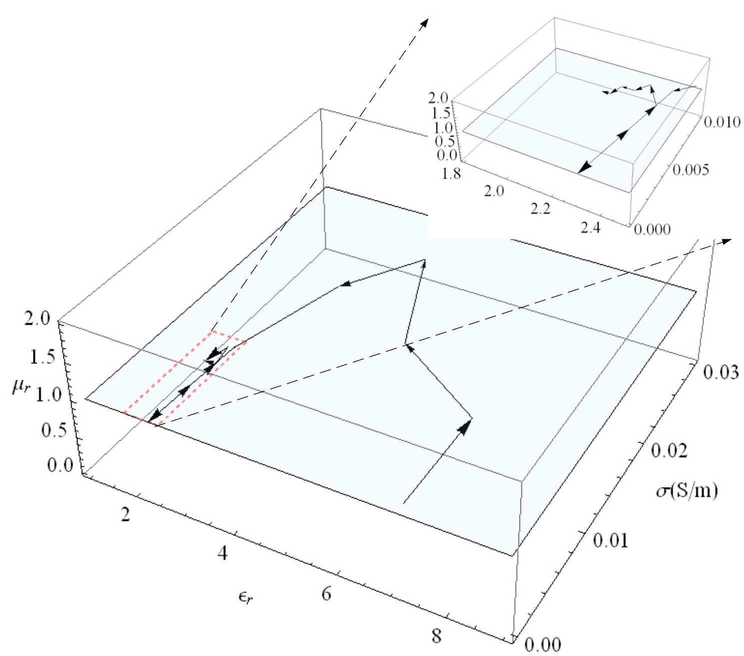

Figure 3.13. Choice of next guess point based on the steepest descent method.

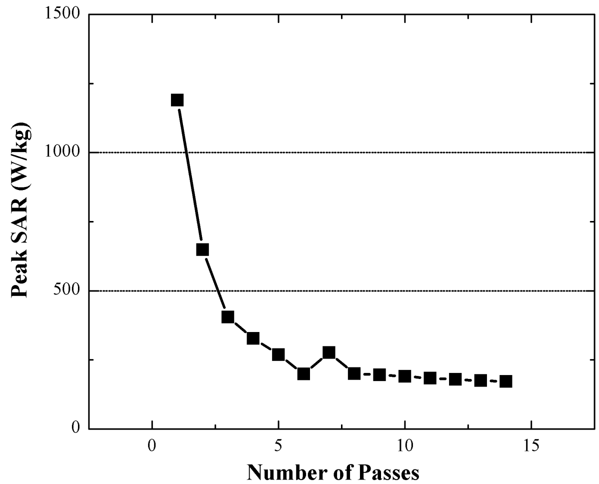

Figure 3.14. Peak SAR versus number of passes.

Chapter 4

Numerical Study of RF Coil Induced Heating on Circular External Fixation Devices

Circular external fixation devices are special forms of an external fixator module in construction. Compared to modular external fixation, the stability and configurability improve and will cause minimal invasive damage to soft tissue as well. Within decades, people have come to prefer to circular external fixator. In regards to MRI RF coil induced heating, circular external fixation devices tend to cause severe tissue heating issues. This section discusses the assessment of MRI RF coil induced heating effects for circular external fixation. To help evaluate the RF induced heating, a novel testing leg phantom is proposed and examined. Then, numerical studies are performed for worst-case RF heating determination.

4.1 Design of Leg Phantom

To analyze the RF induced heating effects of circular external fixation, the ASTM standard F2182 RF induced heating standard which is followed by a lot of studies will no longer be applicable. The fact that the circular external fixation devices are not implantable prevents the applicability of the standard. The large metallic conductive loop will induce extra current and have a great impact on RF heating. The heating evaluation method will be further discussed. Additionally, no standard ASTM phantom is suitable for circular external fixation devices. The existing ASTM phantom is a rectangular container, which is not physically robust enough to enforce every pin around the ring frame of circular external fixation device to be inserted into phantom from any direction.

Under certain circumstances, it is possible to use virtual family human models to help evaluate the RF induced heating effects. However, there are still inadequacies in those human models. First of all, virtual family models are computational models that are converted from a series of MR scan pictures. The utilization of virtual family is only applicable for simulation studies. Currently there are no physical human models for experimental measurement. Simulation results alone will not be sufficient to convince the MR compatibility of circular external fixation devices. Secondly, the virtual family human models are high-resolution models with about 80 different tissues. The large heterogeneity and fine mesh used to distinguish organs will require long simulation time and large GPU memory. For instance, a single DUKE simulation with the presence of a circular external fixation device using 2 mm grid resolution will take about 10 hours and 6G GPU memory to arrive at converged results. For GPUs with smaller memory capacity, the simulation will be much more time-consuming. Last but not least, the effects of different variables can be confounded with each other when using the human models. Unlike the ASTM phantom, which has a regular shape, the human models do not have uniform thicknesses. Even if we are able to get the simulation results after long simulation time, a robust conclusion cannot be easily drawn because multiple parameters are changing at the same time.

In order to assess the MRI RF coil induced heating effects for circular external fixation devices efficiently, there is a demand for developing a novel testing phantom which represents the lower half of the human body. The testing phantom should be regular in shape, as simple as possible to reduce simulation complexity, and representative for human models. The basic idea of developing such a phantom can be shown in Figure 4.1. Since we focus on the lower part of the human body, two cylinders can be used to represent two legs. The connecting part is added to retain the connectivity of the two legs as in human models. The shape and dimension of the testing leg phantom is then adjusted to get an optimal design.

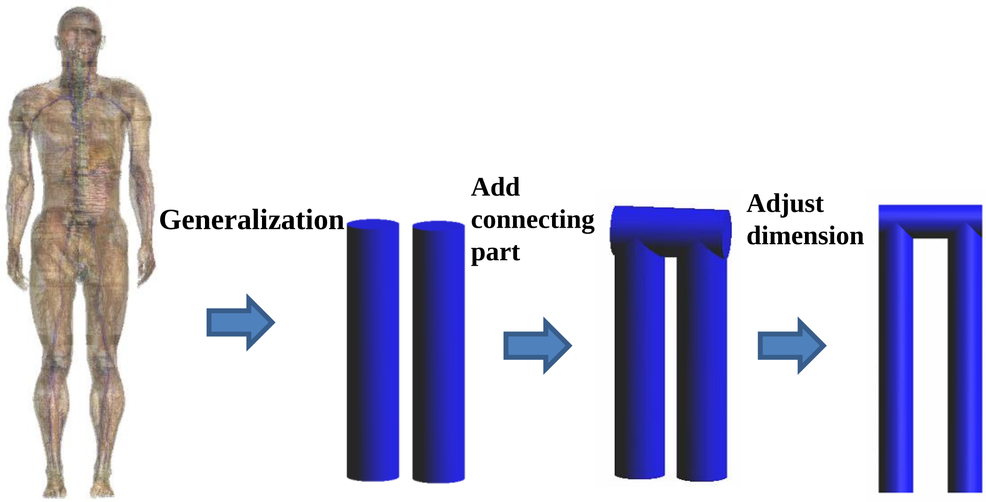

Figure 4.1. Procedures to design the leg phantom.

When manufacturing the leg phantom for experiment test, the physical robustness of the liquid holder that can contain the leg phantom gel should also be considered. In accordance to existing standard, the leg phantom gel should simulate overall human body electromagnetic and thermal properties, where the holder needs to be electrically insulated. To comply with the international standard ASTM F2182, the electromagnetic properties of the leg phantom gel and leg phantom shell can be found in Table 4.1. For ease of inserting the leg phantom inside MRI RF coil and keeping it stable, a hexagon-shaped leg instead of cylinder is used. As shown in Figure 4.2, the struts at the bottom also improve the stability of leg phantom holder. On the upper surface of the holder, several holes with a diameter of 1/4 inch are drilled for pin insertion. When the leg phantom is used for the experimental test, all the holes including the ones that are inserted with screws will be filled with engineering clay. The clay is an electrically insulating material so that the electric property of the liquid holder will not change. To approximate the size of human models, the leg phantom is designed to have a dimension of 80 cm long, 30 cm wide and 10 cm high as indicated in Figure 4.2. Figure 4.3 shows the morphology comparison between the DUKE model and the leg phantom.

Table 4.1. Electrical properties of the leg phantom material

	Relative Permittivity	Electrical conductivity(S/m)
Leg Phantom Gel	80.38	0.47
Leg Phantom Shell	3.7	0

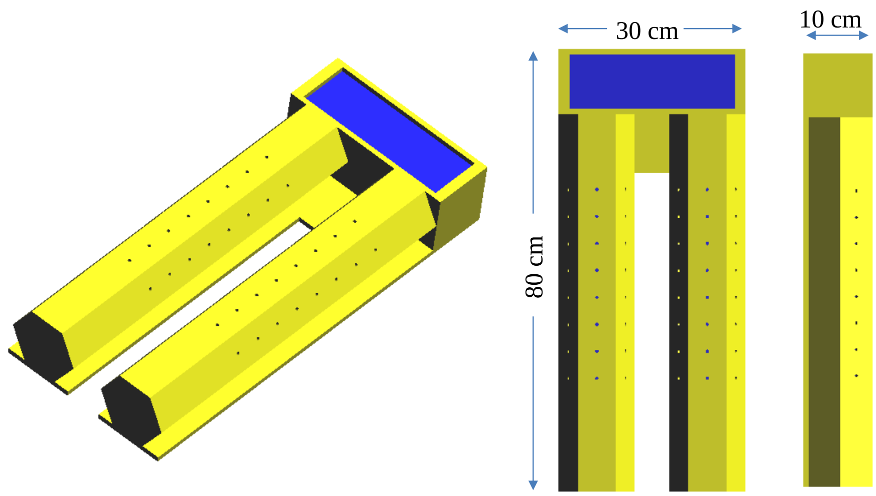

Figure 4.2. Basic dimensions of the leg phantom.

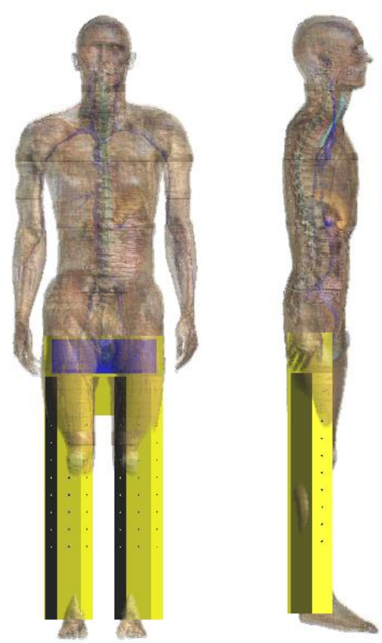

Figure 4.3. Morphology comparison between the DUKE model and the leg phantom.

4.2 Validation of Leg Phantom using Simulation

Before we use the leg phantom for numerical investigation of circular external fixation devices, it is critical to examine the validity of the novel testing phantom. The process of determining whether a leg phantom gets an optimal design is to inspect the electric field and/or SAR distribution inside or around the leg phantom and to compare with the field distribution for human models. In the rest of the section, two sets of simulations are conducted to validate the leg phantom: unloaded leg phantom/human in MRI RF coil comparison and loaded leg phantom/human in MRI RF coil comparison.

4.2.1 Unloaded Leg Phantom/Human in MRI RF Coil

The first group of simulations is set up for unloaded leg phantom and human in MRI RF coil. No medical devices are present in this simulation study. Both the leg phantom and human model are placed in a similar position where most of the leg component is in the center of MRI RF coil as shown in Figure 4.4. The electromagnetic properties of human tissues are retrieved from the ITIS database, where the parameters for the leg phantom gel and the leg phantom shell are specified in Table 4.1. The frequency is set to 64 MHz which corresponds to 1.5 T MRI system.

Due to the absence of circular external fixation devices, there is no significant energy deposition inside the leg phantom or human body. In other words, SAR values will be relatively small and thus are ignored. In these cases, only the electric field distribution is taken into consideration. Different loading positions are studied to show the similarity of leg phantom with human model. Loading position is defined as the distance moving from the horizontal center plane of MRI RF coil to the center part of the leg phantom/human knee center position. The loading position is defined to be zero at the position shown in Figure 4.4, where positive loading position means that the leg phantom or human is moving upwards in the longitudinal direction.

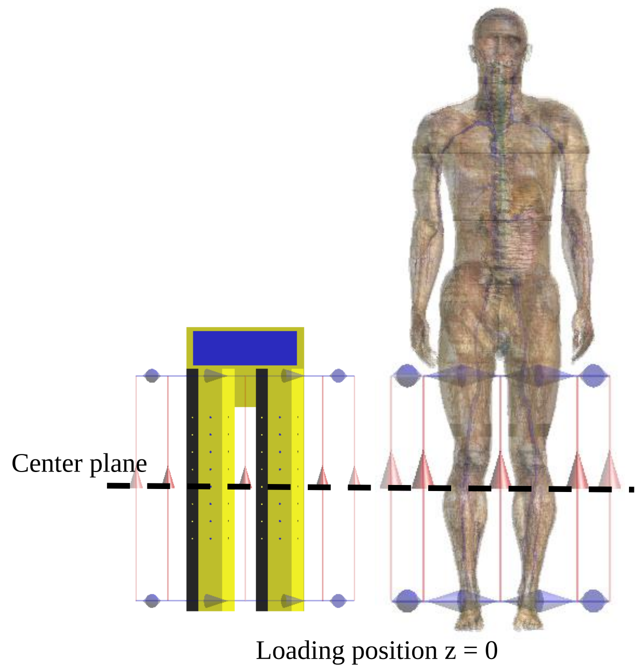

Figure 4.4. Illustration of center plane and 0 mm loading position for the leg phantom and the human model.

Figure 4.5 shows a comparison of the electric field distribution on the center plane between the leg phantom and the human model. It is clear that the field patterns are alike. Electric field distributions in both the leg phantom simulation and human simulations reach their minimum at the inner side of the legs. Progressing outwards, a larger electric field is observed. The electric field outside the leg phantom or human leg is even larger and reaches its maximum in the space between the legs.

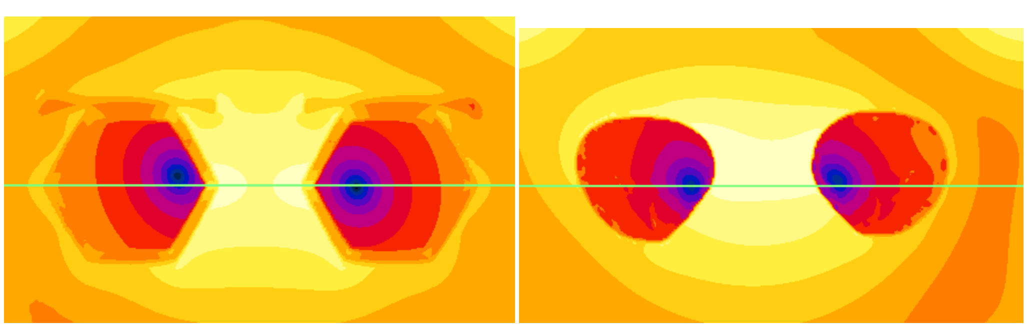

Figure 4.5. E_{RMS} field distribution pattern on the center plane for the leg phantom (left) and the human model (right).

In addition to the pattern, the amplitude of the electric field is an essential parameter to prove that leg phantom is effective to simulate the human leg. The amplitude of the electric field is proportional to the square root of input power, which is referred to as the normalization factor in most simulation studies. Three normalization methods are commonly used and studied in this dissertation: a) 2 W/kg whole body SAR (wbSAR) method, b) partial body SAR (pbSAR) method, and c) B_1 field method. For each method, the electric field on the center line that goes across the leg phantom or human knee position (denoted as the green line in Figure 4.5) is plotted.

The wbSAR method is commonly used for most situations. The input power is adjusted so that the whole body SAR is normalized to 2 W/kg as specified in ASTM F2182. By following the wbSAR method, the electric field plot can be seen in Figure 4.6. The two legs are positioned between the coordinates -0.15 m to -0.05 m and 0.05 m to 0.15 m. Although the electric field inside the phantom is of similar magnitude compared with human body simulation, the field between the two legs is about 700 V/m, which is smaller than the E field for human body (about 950 V/m).

From Figure 4.6, using wbSAR normalization method is likely to give underestimated results. The reason can be explained by the power deposition difference between the leg phantom and human body. For the leg phantom, most of the phantom portion is within the accessible region of the RF coil. For the human body, while the energy is still concentrated near the accessible region, the whole body mass becomes large since all the human body tissues are included. Given the same input power, the whole body SAR for the human body is less than that of the leg phantom. As a result, more input power is required for human models. Under this situation, the electric field in human model is even higher because most of the energy consumption is concentrated near the leg part of the human body. Thus leg phantom using wbSAR

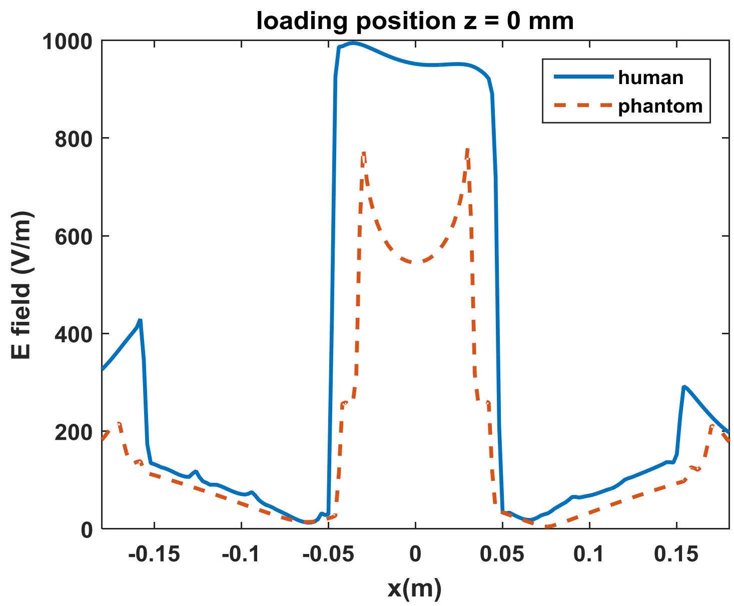

Figure 4.6. E_{RMS} field distribution along the center line for the leg phantom and the human when whole body SAR normalization is used.

normalization provides an underestimation in regards to MRI RF coil induced heating.

The pbSAR is also used in some simulation studies. As described in standard IEC-60601-2-33, it is used for cases in which most of the human body part is outside the MRI RF coil. The partial body SAR is defined as SAR averaged over the mass of the body that is exposed by the RF coil. The mass used to determine the pbSAR is called exposed mass. It is given by the mass within the effective volume of the RF coil. The effective volume of the RF transmit coil is the volume in which no more than 95 % of the total absorbed RF power is deposited inside a homogeneous material which fills the volume normally accessible by the patient. For partial body SAR, the SAR limits scales dynamically with the ratio of exposed mass by total mass. For a normal operating mode, the pbSAR limit is

$$pbSAR = 10 - 8\frac{m_{exposed}}{m_{total}}, \tag{4.1}$$

where $pbSAR$ is in unit of W/kg, $m_{exposed}$ is the exposed mass, and m_{total} is the total mass.

The electric field plot along the center line using pbSAR normalization is shown in Figure 4.7. Compared with wbSAR plot in Figure 4.6, the E field difference between the leg phantom and human models becomes less significant. The leg phantom using pbSAR normalization is still underestimating the RF heating in human models because the electric field between legs is still less than the field intensity for human body. The pbSAR normalization method helps improve the electric field similarity, but still underestimates the field in human body.

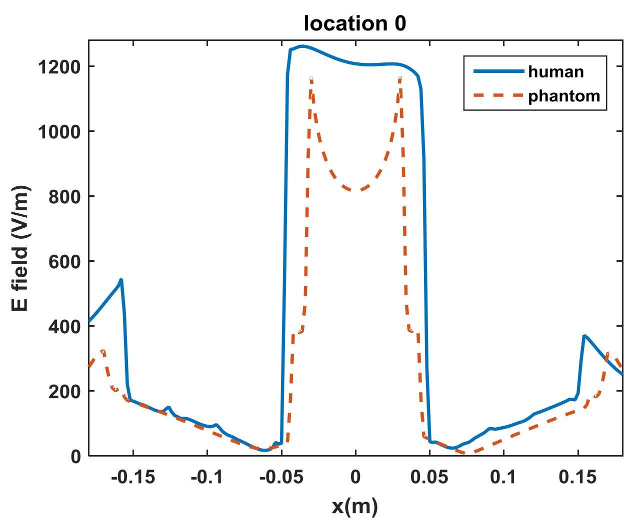

Figure 4.7. E_{RMS} field distribution along the center line for the leg phantom and the human when partial body SAR normalization is used.

Both wbSAR and pbSAR normalization are significantly affected by the mass that is present in the MRI system. Regardless of the mass, the B_1 normalization method is proposed based on the fact that image quality of MRI is closely related to the amplitude of MRI RF pulse. During the MR scan, the B1 field remains unchanged to achieve good signal-to-noise-ratio (SNR) for imaging. In the MR system, the B_1+ and B_1- field are defined as the rotational components of the B-field (typically used for RF field analysis) with the formulae

$$
\begin{aligned}
B_{1+}(r) &= \tfrac{1}{2}\left(B(r)\cdot\widehat{x} + jB(r)\cdot\widehat{y}\right) \\
B_{1-}(r) &= \tfrac{1}{2}(B(r)\cdot\widehat{x} - jB(r)\cdot\widehat{y})^{*}.
\end{aligned}
\tag{4.2}
$$

By convention, the B_1+ and B_1- field are calculated at the isocenter, which is located at the geometric center of MRI RF coil. During the normalization process, the B_1 field, which is chosen from the B_1+ or B_1- field with larger amplitude, is normalized to a constant value. The scaled input power is then calculated by the square of B_1 field scaling. Table 4.2 lists the B_1 field at the isocenter for different loading position when using 2 W/kg wbSAR normalization. As the loading position moves from -400 mm to 400 mm, the B_1 field in leg phantom first decreases and then increases, while the B_1 field in the human model grows from 4.58 μT to 9.87 μT. At loading position -200 mm, the B_1 field in leg phantom is close to the B_1 field in the human body. By taking the average of these similar B_1 field values, the normalized B_1 field for all loading positions is chosen to be 5.08 μT.

Table 4.2. B_1 field at the isocenter for different loading position using 2W/kg wbSAR normalization

Loading position	B_1 field in leg phantom (μT)	B_1 field in human model (μT)
-400	6.87	4.58
-300	5.80	4.67
-200	5.03	5.14
-100	4.46	5.68
0	4.16	6.78
100	3.92	7.67
200	3.85	8.31
300	3.94	8.90
400	4.24	9.87

Based on B1 normalization, the x, y, and z components of electric field along the center line can be viewed in Figure 4.8, Figure 4.9, and Figure 4.10. By examining the real and imaginary part of each component, the unloaded leg phantom is proved to be consistent with the human model in terms of electric field distribution.

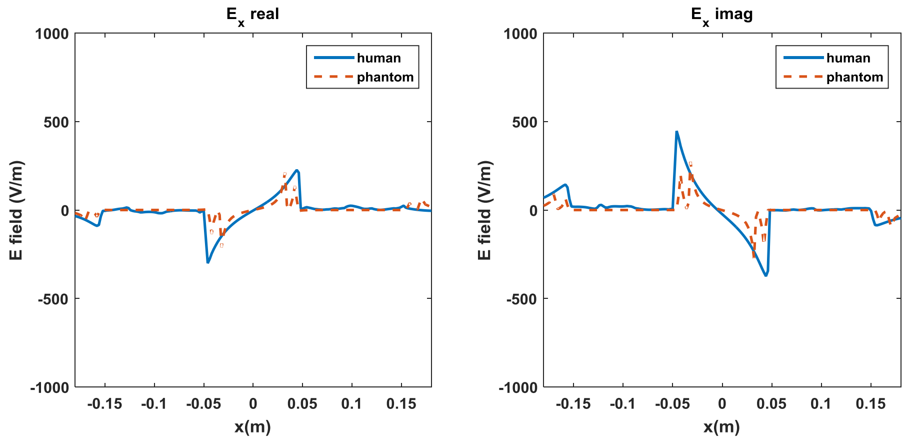

Figure 4.8. E_x along the center line using B_1 field normalization.

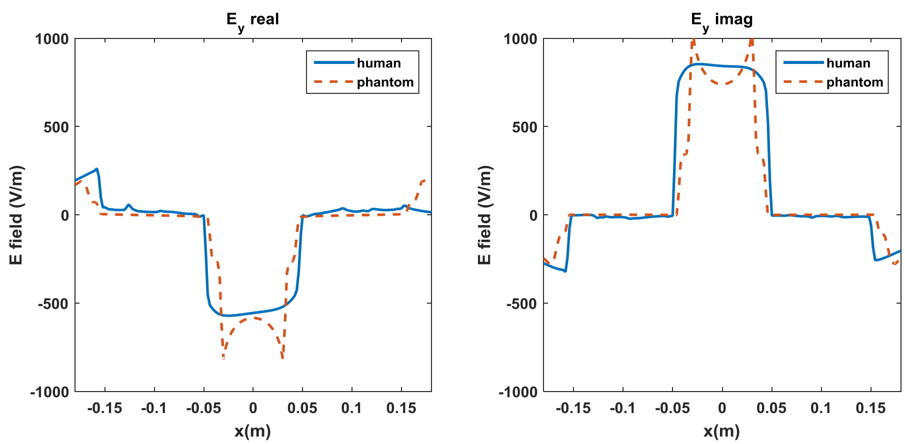

Figure 4.9. E_y along the center line using B_1 field normalization.

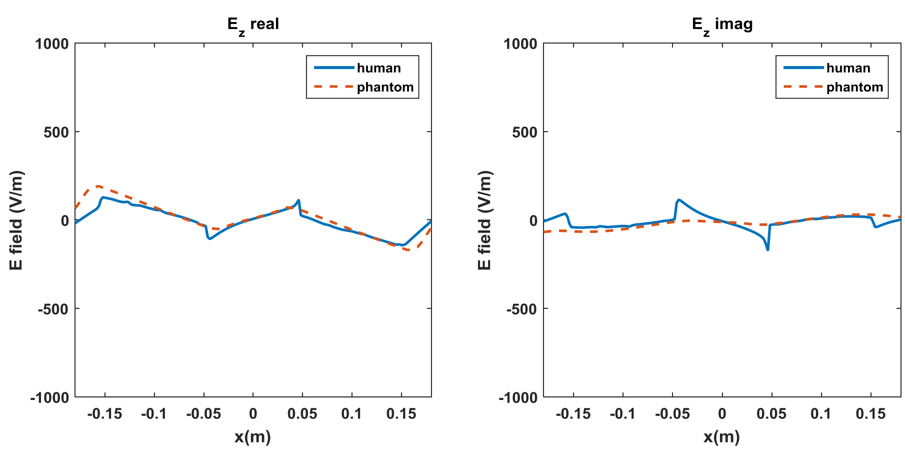

Figure 4.10. E_z along the center line using B_1 field normalization.

The RMS value of the total electric field along the center line is plotted in Figure 4.11. The two curves in Figure 4.11 are overlapping with each other, indicating that the overall impacts are similar.

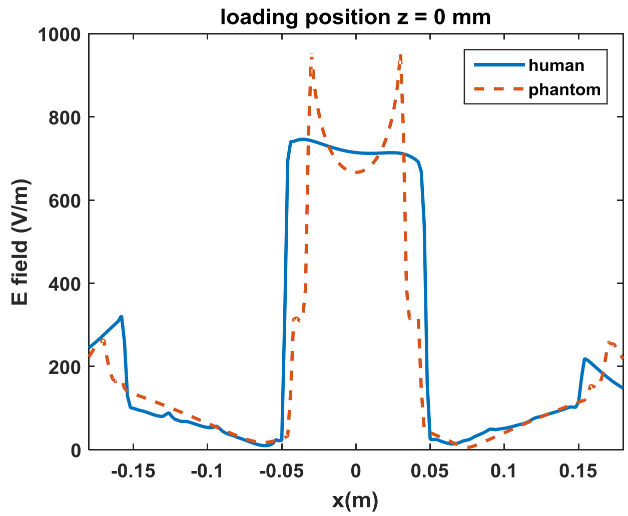

Figure 4.11. E_{RMS} field along the center line at 0 mm loading position using B_1 field normalization.

Beyond case $z = 0$, the B_1 normalization method is also valid for other loading positions. Figure 4.12 to Figure 4.15 shows the electric field comparison between the leg phantom and the human model at different positions along the center line.

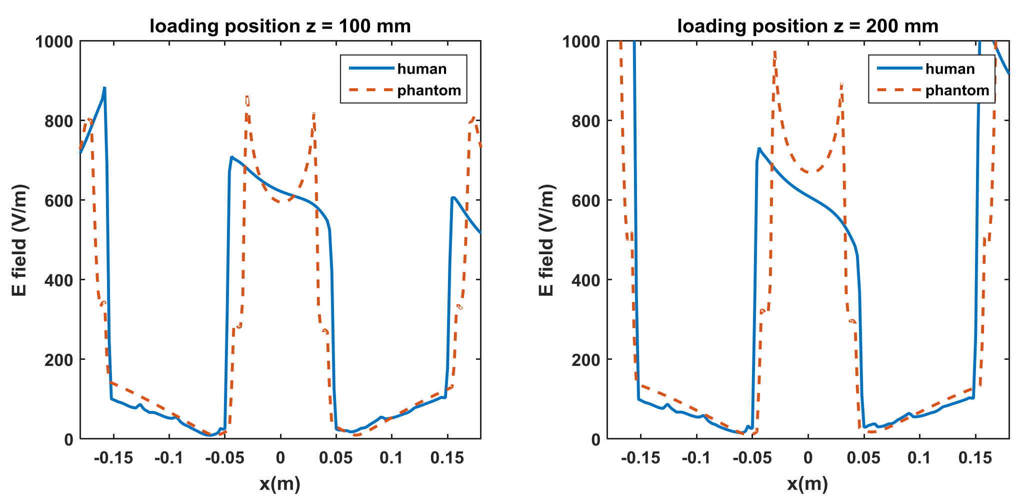

Figure 4.12. E_{RMS} field along the center line at 100 mm (left) and 200 mm (right) loading position using B_1 field normalization.

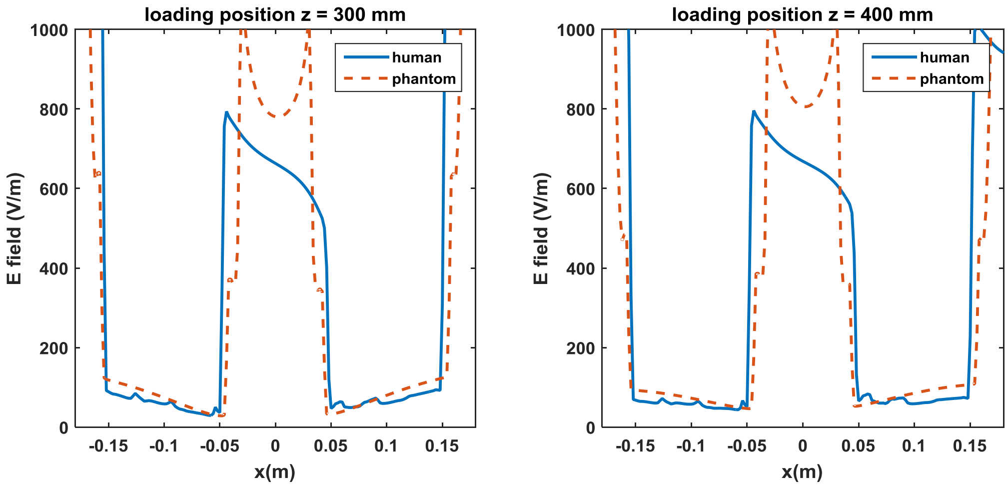

Figure 4.13. E_{RMS} field along the center line at 300 mm (left) and 400 mm (right) loading position using B_1 field normalization.

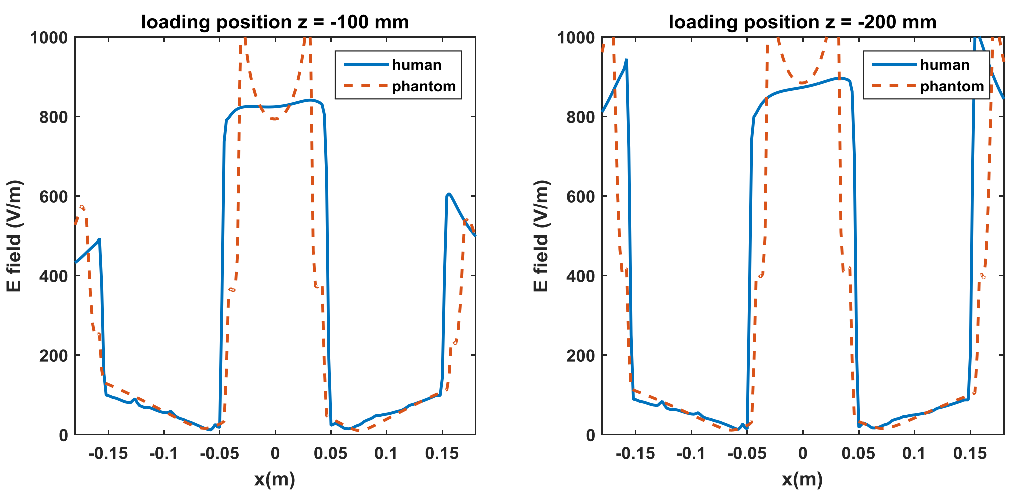

Figure 4.14. E_{RMS} field along the center line at -100 mm (left) and -200 mm (right) loading position using B_1 field normalization.

It is clear that the leg phantom can be used to represent human model simulations using the B_1 normalization method. The normalized field has a similar distribution to that of the human model for different loading positions ranging from -400 mm to 400 mm.

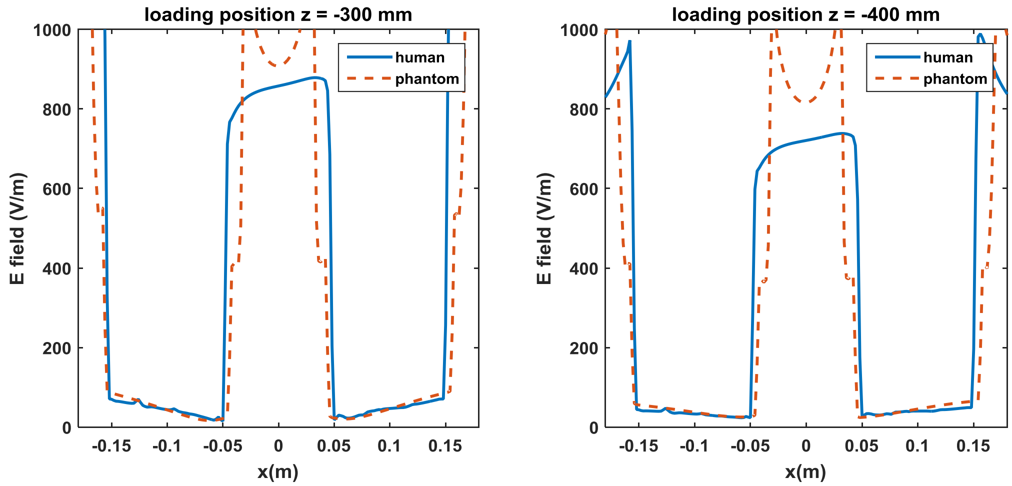

Figure 4.15. E_{RMS} field along the center line at -300 mm (left) and -400 mm (right) loading position using B_1 field normalization.

4.2.2 Loaded Leg Phantom/Human in MRI RF Coil

In the previous section, the field distribution of the unloaded leg phantom was shown to be similar to that of an unloaded human model for different loading positions. In most situations, the leg phantom is loaded with medical devices for lab testing. In this section, the effect of loading of the medical device is compared for both the leg phantom and the human model.

The simulation setup is depicted in Figure 4.16. The leg phantom and human model are placed at loading position $z = 0$ mm. A typical circular external fixation device is placed near the knee position of the human body. The center of circular external fixation device coincides with the center of the MRI RF coil in the longitudinal direction. The absolute position of the circular external fixation device is kept same for the left and right configuration in Figure 4.16.

Due to the presence of the metallic medical device, the electric field distribution in both the leg phantom and human body is altered by the surface current induced by the device. The overall effect of the altered electric field is the accumulation of power dissipation near the tip of the screws that impinge into leg phantom or human

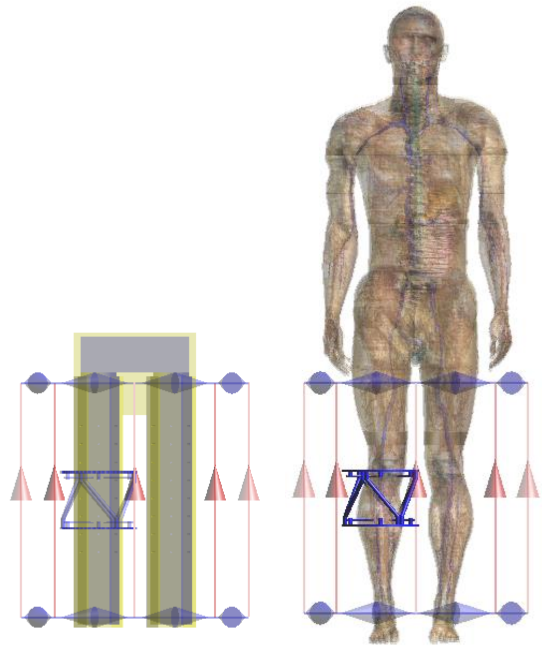

Figure 4.16. Simulation setup for the leg phantom and the human model with the presence of circular external fixation device.

body. Specific absorption rate (SAR) is calculated in this study to quantify the power dissipation. Figure 4.17 shows the SAR distribution for circular external fixation device loaded into the leg phantom near the top ring frame. Energy is concentrated near the tip of the impinging screw, and decays dramatically in the leg phantom gel.

The same SAR behavior is observed for circular external fixation devices loading into the human model. In Figure 4.18, the maximum SAR occurs at the tip of the screw. Although the field distribution shows some singularity due to the inhomogeneity of human body tissue, the general pattern is still consistent with that of the leg phantom.

In addition to the SAR distribution pattern, the use of a normalization factor is also investigated. Due to the presence of large metallic medical devices, the conventional B_1 normalization method does not function well. Strong surface current on devices will induce a large scattered field, which has a notable impact on B_1+ or B_1- field computation. The B_1 field calculation at the isocenter will become more difficult for circular external fixation devices in this case because the location of the circular

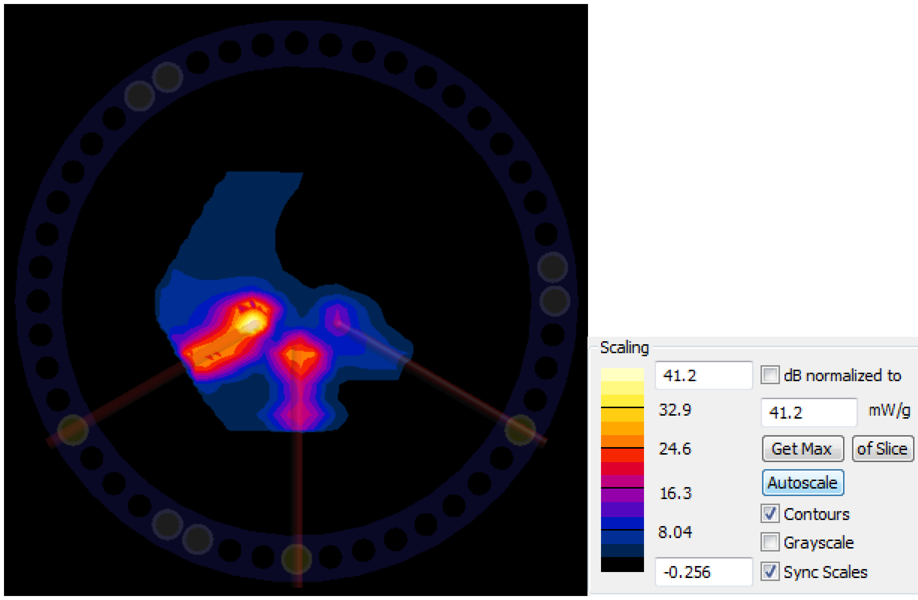

Figure 4.17. SAR distribution for circular external fixation device loaded into the leg phantom.

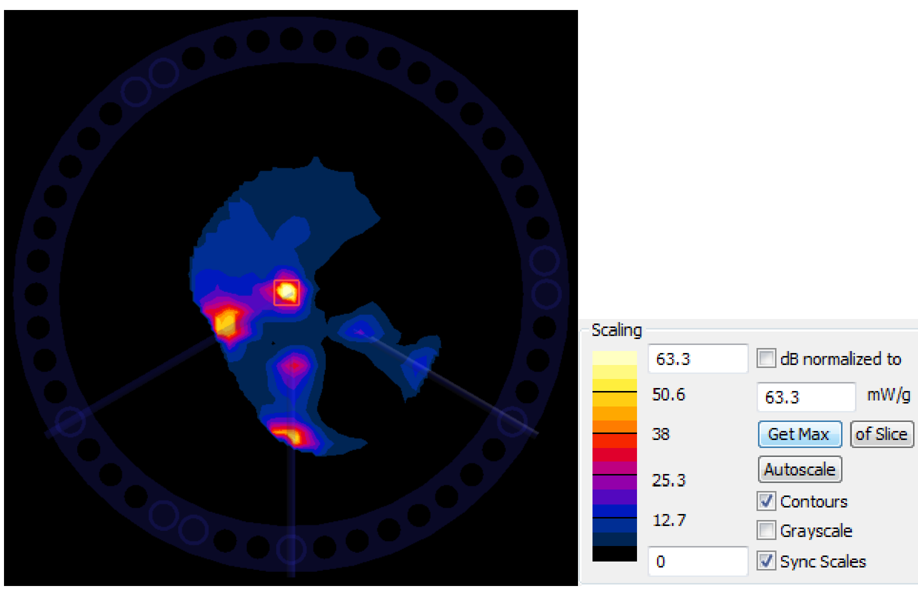

Figure 4.18. SAR distribution for circular external fixation device loaded inside the human model.

external fixation devices is very close to the MRI RF coil isocenter. The incident B_1 field is used as normalization criteria Instead of B_1 field. The incident field refers to the electric fields associated with the unloaded leg phantom or human body in MRI RF coil, which has been studied in the previous section. To distinguish from the incident field, the electric fields from induced current on circular external fixation devices are referred to as the induced field. The incident field is calculated without the presence of the circular external fixation device. No matter what the circular external fixation device is, the incident B_1 field is constant. The total electromagnetic field is the superposition of incident field and induced field.

Processes to obtain the same incident B_1 field are described as follows: (1) Use the conventional source settings to run an unloaded leg phantom/human simulation, in which the medical device is removed. Record the input power without any normalization. The power that excites the incident field is defined as the "pre-normalized incident power", which means the total input power when using the pre-defined source settings. (2) Adjust the normalization factor so that the B_1 field at the isocenter is equal to 5.08 μT, which is derived in the previous section. The total input power is called the "B_1 normalized incident power." (3) Apply the same source settings, and run a simulation with the presence of the circular external fixation device. Input power is then obtained without normalization. The power is referred to as the "pre-normalized total power." (4) "Incident B1 normalized total power" is calculated by

$$P_{B1_{inc}}^{tot} = \frac{P^{tot}}{P^{inc}} P_{B1}^{inc}, \tag{4.3}$$

where P^{inc} is pre-normalized incident power, P^{tot} is pre-normalized total power, P_{B1}^{inc} is B_1 normalized incident power, and $P_{B1_{inc}}^{tot}$ is incident B_1 normalized total power. Using the incident B_1 normalization, the MRI RF coil induced heating effect can be quantified.

Figure 4.19 shows the induced surface current distribution for a typical circular external fixation device exposed in MRI RF environment. It is observed that currents are induced from ring and struts structure of circular external fixation as well as the pin. Different parameters of the external fixation device are studied including: a) insertion depth, b) ring frame size, c) strut height and d) loading position. These parameters are chosen because the largest induced current appears at the ring frame structure, the struts, and the pins that enter the human body, as indicated in Figure 4.19. In addition, the loading position needs to be assessed because patients with medical devices are frequently loaded in or out of the MR machine during the MR scanning procedure. By showing the maximum 1g-averaged SAR tendency affected by each parameter, the leg phantom is proved to be representative for human model.

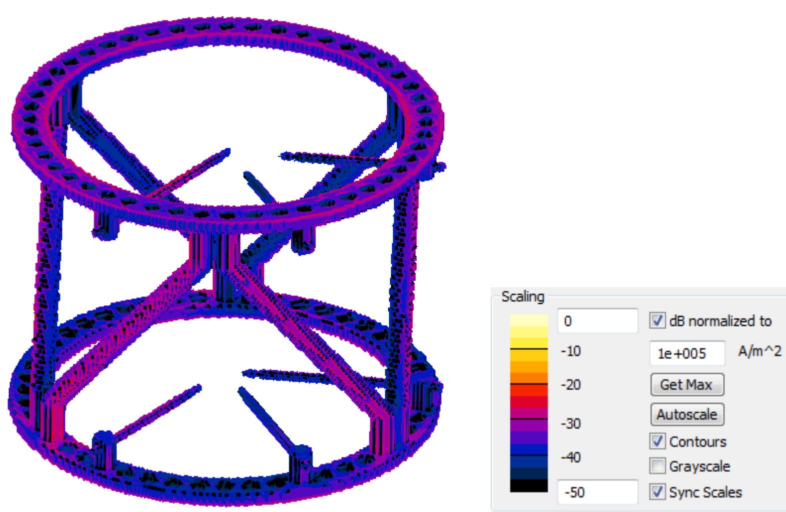

Figure 4.19. Induced surface current distribution for a typical circular external fixation device under MRI RF environment.

a) Insertion depth

The insertion depth is the length that a screw is immersed inside the phantom gel or the human body as shown in Figure 4.20. It plays an important part in the MRI RF coil induced heating effect because the insertion depth determines the path that energy takes during dissipation in the leg phantom or the human model. Insertion depths are chosen as 25 mm, 35 mm, and 45 mm to show the validity of the leg

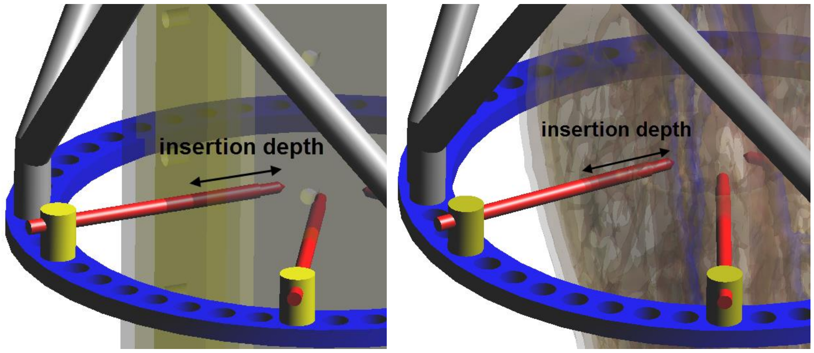

Figure 4.20. Insertion depth for circular external fixation device in the leg phantom (left), and in the human model (right).

phantom. For each insertion depth, the circular external fixation device is placed near the human model as well as the leg phantom.

Table 4.3. Maximum 1g-averaged SAR for different insertion depth

model	Insertion depth (mm)	Incident B1 normalized total power(W)	Maximum 1g-averaged SAR(W/kg)
Human model	25	191.17	79.6
Human model	35	190.79	60.6
Human model	45	190.64	47.8
Leg phantom	25	148.04	62.9
Leg phantom	35	147.54	48.5
Leg phantom	45	147.28	39.8

Table 4.3 shows the incident B1 normalized total power for each simulation and maximum 1g-averaged SAR. The relationship between maximum 1g-averaged SAR and insertion depth is plotted in Figure 4.21. As the insertion depth increases, the RF heating effects tend to decrease. Because the leg phantom gel is electrically lossy like the human tissues, when the insertion depth gets larger, the induced energy that travels along the pin to the tip will lead to more power dissipation along the path. Less energy will be dissipated at the pin tip. On the other hand, if the insertion depth becomes very short, the dissipated power is concentrated on the tip of the pin. The pin will reserve the most power and generate the worst-case heating.

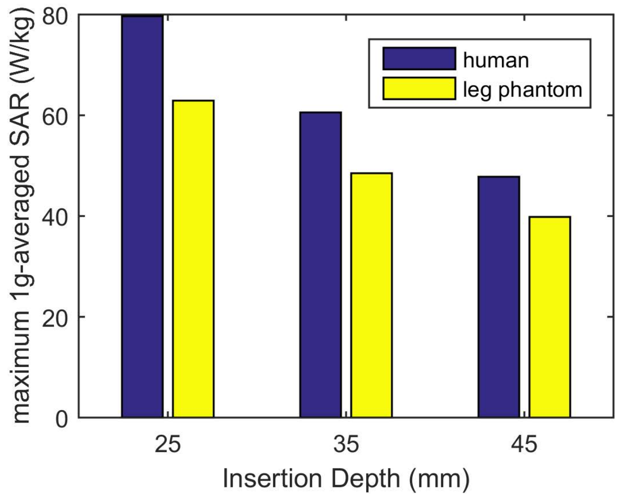

Figure 4.21. Maximum 1g-averaged SAR versus insertion depth for the leg phantom and the human model.

b) Ring frame size

Ring frame size can also affect MRI RF coil induced heating. For the leg phantom validation process, the radius of the ring size is selected to be 89 mm, 99 mm, and 109 mm as shown in Figure 4.22.

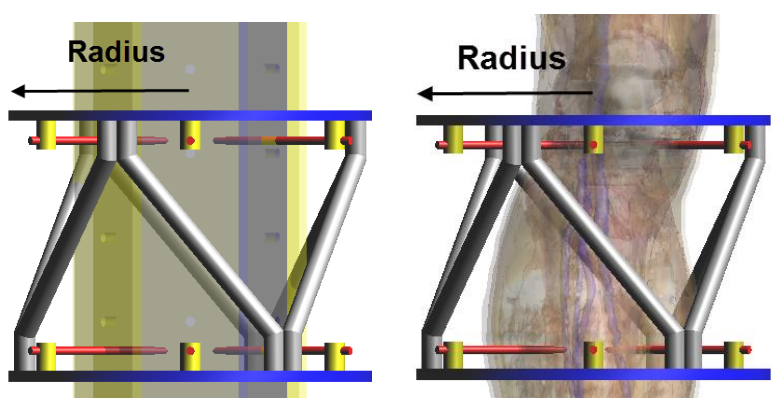

Figure 4.22. Ring frame radius for circular external fixation device in the leg phantom (left), and in the human model (right).

When loading the leg phantom or the human model with circular external fixation devices into the MR environment, the maximum 1g-averaged SAR is calculated as shown in Table 4.4. Figure 4.23 shows the trend of maximum 1g-averaged SAR varying with the ring size. As the radius of the ring frame grows, the maximum SAR appears near the tip of the pins that enter the human body is increasing. The same tendency is observed for both leg phantom and human simulations. These phenomena mean that a large conductive loop will easily receive RF signals, and strongly impact the current distribution in tissue. The larger the ring size is, the higher the RF heating effect will be.

Table 4.4. Maximum 1g-averaged SAR for different ring frame radius

model	Ring frame radius (mm)	Incident B1 normalized total power(W)	Maximum 1g-averaged SAR(W/kg)
Human model	89	193.32	57.3
Human model	99	190.79	60.6
Human model	109	187.54	66.0
Leg phantom	89	149.86	41.7
Leg phantom	99	147.54	48.5
Leg phantom	109	143.91	53.5

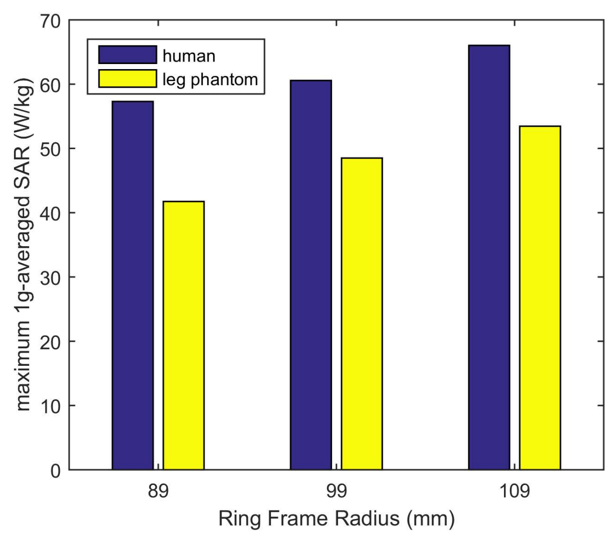

Figure 4.23. Maximum 1g-averaged SAR versus ring frame radius for the leg phantom and the human model.

c) Strut height

Strut height is the vertical distance between the upper ring frame and the lower ring frame as described in Figure 4.24. To investigate the effect of strut height, circular external fixation devices with different heights ranging from 140 mm to 170 mm are placed in leg phantom and the human model. The maximum 1g-averaged SARs under MR environment are calculated after the incident B_1 normalization.

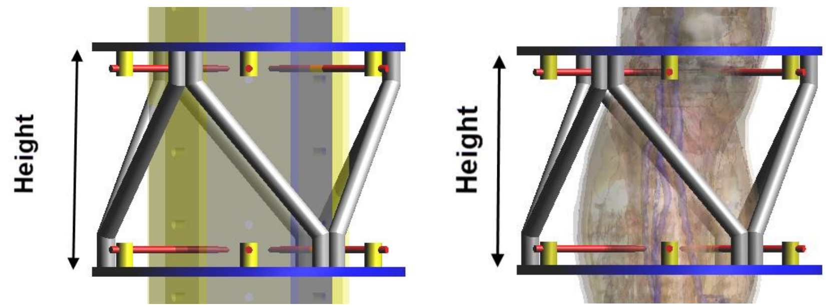

Figure 4.24. Strut height for circular external fixation device in the leg phantom (left), and in the human model (right).

Table 4.5 shows how maximum 1g-averaged SAR changes with strut height. To give a better illustration, the trend is also plotted in Figure 4.25. Because of the heterogeneity of human tissues and the irregular shape of human body, the fluctuation of maximum 1g-averaged SAR versus strut height curve is expected. Even the insertion depths of the screws are forced to be the same, the effects of human tissue and leg thickness at corresponding locations are different. Although there is deviation within the two curves, the basic trend is the same. The dashed line in Figure 4.25 is a fitted line using linear regression. Generally speaking, shorter strut height will lead to lower RF heating effect. This phenomenon is related to the antenna effect. In MRI RF exposure, the metal devices are acting like receiving antennas which capture the RF power. The induced RF power is dissipated inside the phantom gel. Compared with the wavelength for 64 MHz signal in air, the simulated strut height is much smaller. According to antenna theory, for the length that is much smaller than the half wavelength, increasing the antenna length will lead to higher efficiency, which will introduce stronger coupling between the MR environment and the external fixation devices. The shorter the distance between the ring frames is, the weaker the coupling there will be.

Table 4.5. Maximum 1g-averaged SAR for different strut height

Model	Strut height (mm)	Incident B1 normalized total power(W)	Maximum 1g-averaged SAR(W/kg)
Human model	140	201.76	63.1
Human model	145	201.87	67.0
Human model	150	201.87	63.8
Human model	155	202.59	60.6
Human model	160	201.19	64.1
Human model	165	201.38	73.4
Human model	170	201.12	88.6
Leg phantom	140	162.58	44.1
Leg phantom	145	162.50	45.7
Leg phantom	150	162.25	47.4
Leg phantom	155	162.38	48.5
Leg phantom	160	161.83	50.6
Leg phantom	165	161.71	51.8
Leg phantom	170	161.67	53.0

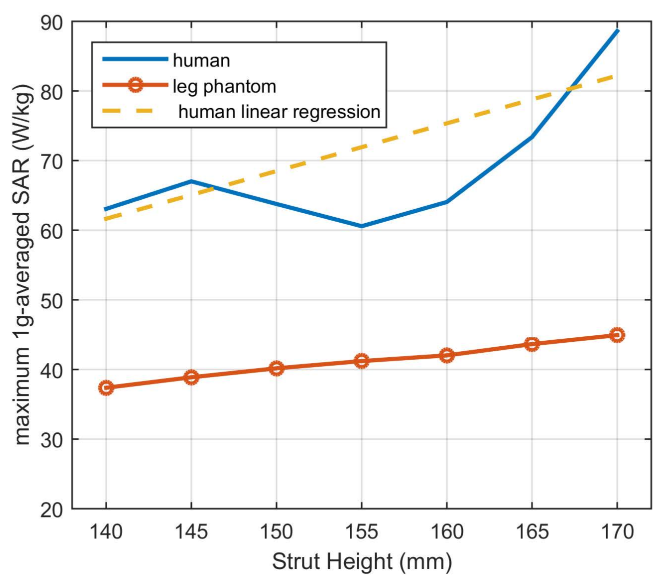

Figure 4.25. Maximum 1g-averaged SAR versus strut height for the leg phantom and the human model. Dashed line denoted the linear regression of human data.

d) Loading position

During the MR scanning procedure, patients with medical devices are frequently loaded in or out of the MR machine. To assess the RF heating effects of loading position, a set of simulations is conducted on leg phantom and the human model. As described in the previous section, the same simulation setup is used except that the circular external fixation device is moving together with the leg phantom and the human model. Figure 4.4 shows the loading position at $z = 0$ mm, where positive loading position means that both the leg phantom or the human and the circular external fixation device are moving upwards. The loading position in the vertical direction (z direction) is changing from -400 mm to 400 mm with an increment of 100 mm.

Table 4.6. Maximum 1g-averaged SAR for different loading position

Model	Loading position (mm)	Incident B1 normalized total power(W)	Maximum 1g-averaged SAR(W/kg)
Human model	-400	271.22	42.9
Human model	-300	278.03	62.5
Human model	-200	252.21	73.6
Human model	-100	235.39	74.9
Human model	0	207.48	65.6
Human model	100	193.43	53.5
Human model	200	208.40	63.1
Human model	300	210.88	69.2
Human model	400	203.33	63.2
Leg phantom	-400	130.26	27.6
Leg phantom	-300	134.50	38.1
Leg phantom	-200	141.60	46.2
Leg phantom	-100	155.83	51.4
Leg phantom	0	166.50	46.2
Leg phantom	100	162.67	34.9
Leg phantom	200	162.00	27.6
Leg phantom	300	160.48	30.7
Leg phantom	400	157.58	29.7

The incident B_1 field normalization factor can be calculated using the unloaded leg phantom and human simulation results. Table 4.6 shows the calculated incident B_1 total power as well as the maximum 1g-averaged SAR near the screw. Unlike the previous results, in which the incident B_1 normalized total power stays almost constant, the normalized input power is changing with different loading positions. The effect of maximum 1g-averaged SAR affected by the loading position can also be viewed in Figure 4.26. From Figure 4.26, it is clear that the trend of maximum 1g-averaged SAR for the leg phantom and the human model are similar. In the leg phantom and the human model simulations, the worst case 1g-averaged SAR value occurs at z = -100 mm.

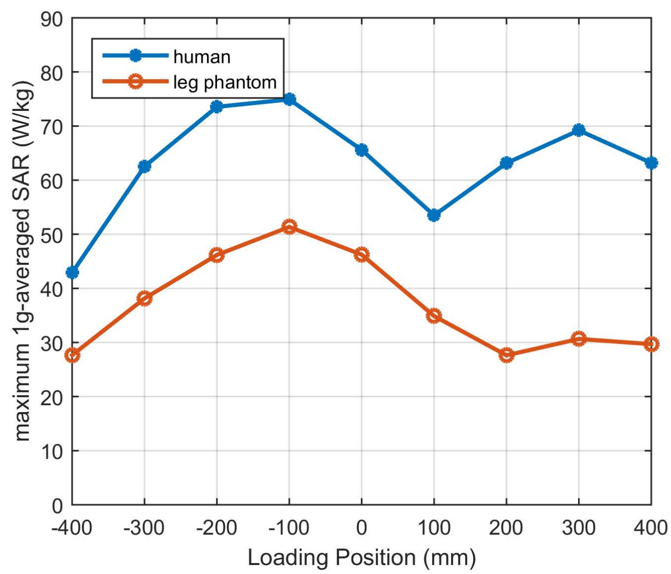

Figure 4.26. Maximum 1g-averaged SAR versus loading position for the leg phantom and the human model.

To conclude, by showing the same maximum 1g averaged SAR tendency affected by insertion depth, ring frame radius, strut length and loading position for both leg phantom and the human model, the leg phantom is proved to be representative for the human model. In the following sections, the leg phantom is used to determine the worst case RF heating configuration for a circular external fixation device.

4.2.3 Experimental Validation

In addition to simulation results, an experiment was performed to estimate the MRI RF induced heating inside an MRI shielding room. A testing 10 cm titanium rod is placed inside the leg phantom. The distance from the rod to the left inner edge of the phantom container is about 3 cm. The rod is located at the center plane of the left leg as shown in Figure 4.27.

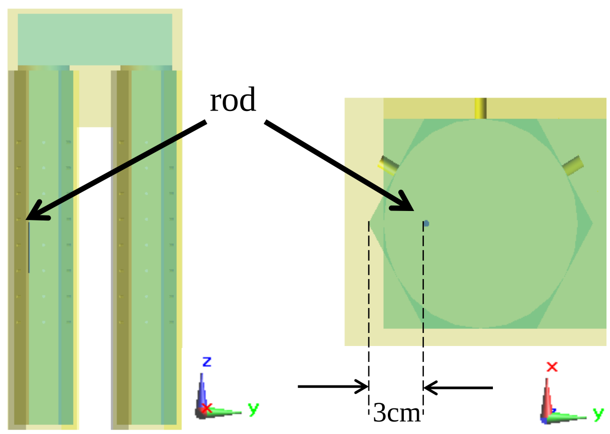

Figure 4.27. Illustration of experimental setup for leg phantom validation.

In experiment, the rod was fixed on a plastic frame, and slid into the leg phantom as shown in Figure 4.28. the holes on the side wall is covered with engineering clay. Fishing lines were used to push in or pull out the frame together with the rod. The employment of the fishing line and the plastic frame ensures that the rod is placed at the center of the leg phantom in the longitudinal direction.

The leg phantom loaded with the 10 cm rod is then placed at the center of the MRI bore (see Figure 4.29). Before the thermal experiment was conducted, the H field at the isocenter of the RF coil was measured using H probe as shown in Figure 4.30. The H field at the isocenter is 3.3 A/m when the MRI RF coil is turned on. The H field is used to normalize the input power in EM simulation. A temperature probe is attached at the tip of the rod and records the temperature during the 15 min MR exposure.

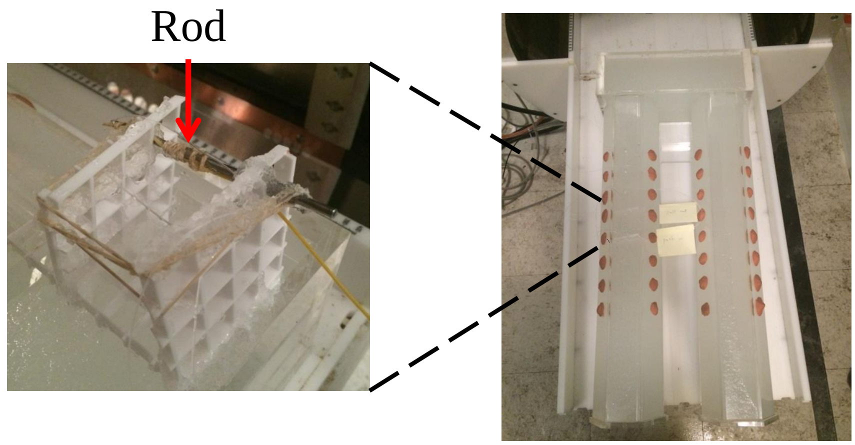

Figure 4.28. Experiment setup for rod with fixture and the placement in the leg phantom.

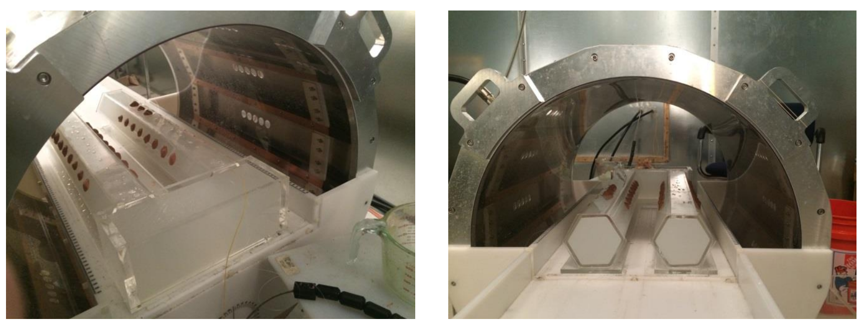

Figure 4.29. Side view of leg phantom with 10 cm rod loading inside the MRI bore.

Figure 4.30. H probe measurement at isocenter.

A validation simulation was run for comparison. After normalizing the H field in simulation to the measured data, the input power of the EM simulation is 102.6 W. The electric field, together with the normalization power factor, is used in thermal simulation. The thermal properties for leg phantom gel, leg phantom shell and the 10 cm rod are shown in Table 4.7. The EM source in the thermal simulation is turned on for 15 min, and then turned off so the rod will have 3 min cooling time. Figure 4.31 plots the temperature increase near the tip of the rod in the experiment and the simulation, and shows good agreement.

Table 4.7. Maximum 1g-averaged SAR for different loading position

Model	Specific heat capacity(J/kg/K)	Thermal Conductivity(W/m/K)	Density(kg/m^3)
Leg phantom gel	4160	0.42	1000
Leg phantom shell	1000	0.2	1000
PEC	400	7	8000

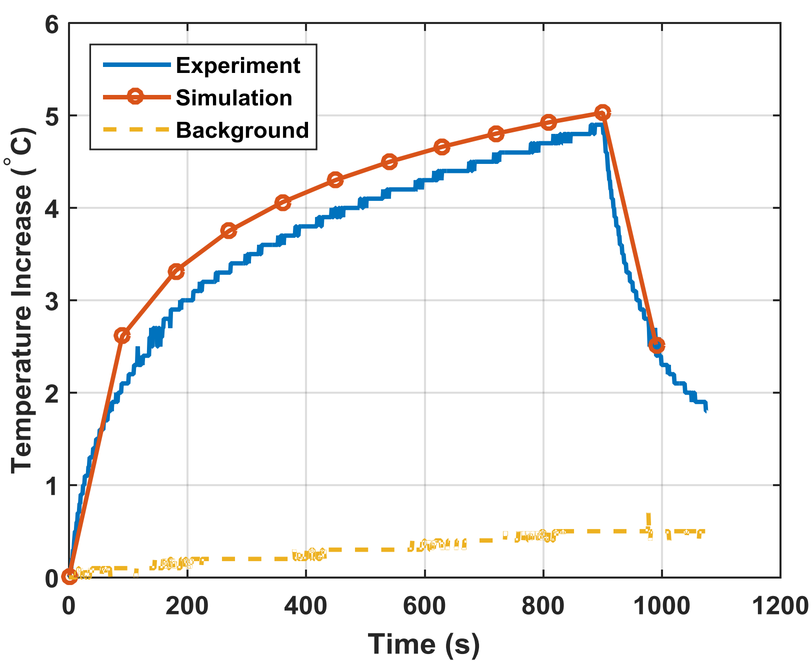

Figure 4.31. Temperature increase at the tip of 10 cm rod versus time.

4.3 Numerical Study of MRI RF Coil Induced Heating for Circular External Fixation using Leg Phantom

In the previous section, a number of simulation studies are provided to prove the validity of using leg phantom to represent human body. The leg phantom has been shown to have similar behavior compared to the human model by applying incident B_1 normalization. In this section, the leg phantom is used to determine the worst case circular external fixation device configuration. The strategy to seek the worst case MRI RF heating will be applied as follows.

4.3.1 Screw/wire Configuration

Screws and/or wires can be used in surgery depending on the patient's need. In clinical use, the number of screws and/or wires may vary. The utilization of circular external fixation improves the configurability of screws and wires. Typically screws and wires can be used simultaneously to obtain optimal stability. To seek the worst case heating configuration, different screw and pin setups are listed in Table 4.8.

Table 4.8. Maximum 1g-averaged SAR for different wire/screw configurations

Config index	Number of wire	Number of screw	Incident B_1 normalized total power(W)	Maximum 1g-averaged SAR(W/kg)
A	3	0	167.05	21.8
B	2	1	166.79	25.8
C	2	1	165.76	27.4
D	2	1	168.39	40.8
E	1	2	164.99	40.9
F	1	2	167.80	58.7
G	1	2	166.88	41.7
H	0	3	165.50	70.4
I	0	4	165.87	61.0

For every configuration, the device is loaded together with the leg phantom into an MRI RF coil. By applying incident B_1 normalization, the maximum 1g-averaged SAR can be viewed in Table 4.8. The maximum 1g-averaged SAR varies as a function of screw/wire configuration. Among different configurations, the three-screw configuration will give the worst case MRI RF heating as indicated by Figure 4.32. This can be explained by the power dissipation. A strong current is induced near the edge of metallic parts or the tip of screws that are inserted into phantom. RF power is generated around those locations. Compared with wire structures, screw structures tend to have fewer power dissipation paths. Intense energy is concentrated near the tip of the screw. This becomes more significant for smaller insertion depth and fewer screws.

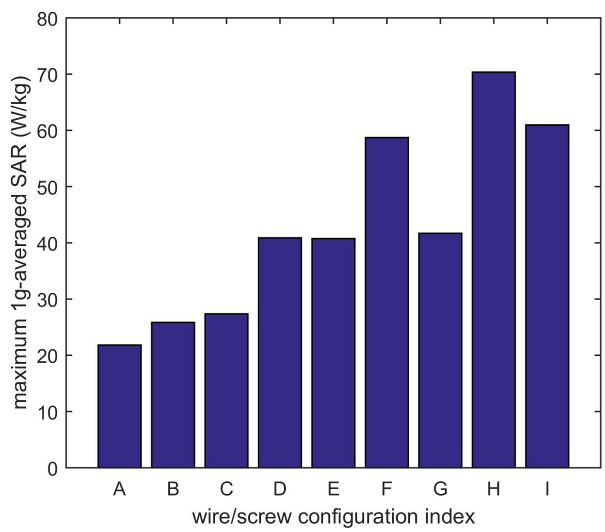

Figure 4.32. Maximum 1g-averaged SAR for different wire/screw configurations.

4.3.2 Ring Size

Previous search shows that circular external fixation devices with a 3-screw configuration are the worst MRI RF heating case. Based on the worst-case screw/wire configuration, the frame ring size is then changed. Typical ring radius ranges from 60 mm to 120 mm. To perform a complete ring size study, the following ring frame radius sizes are chosen: 69 mm, 79 mm, 89 mm, 99 mm, 109 mm, and 119 mm.

The maximum 1g-averaged SAR is calculated for each case as shown in Figure 4.33. The MRI RF heating effects tend to be more significant when the ring frame size becomes larger. By applying incident B_1 normalization, more detailed data can be found in Table 4.9. We can observe an increasing trend for the input power as we enlarge the ring frame size. For a circular external fixation device with larger ring frame size, the larger conductive loop tends to received more RF power from the MRI RF coil, and thus produce higher SAR.

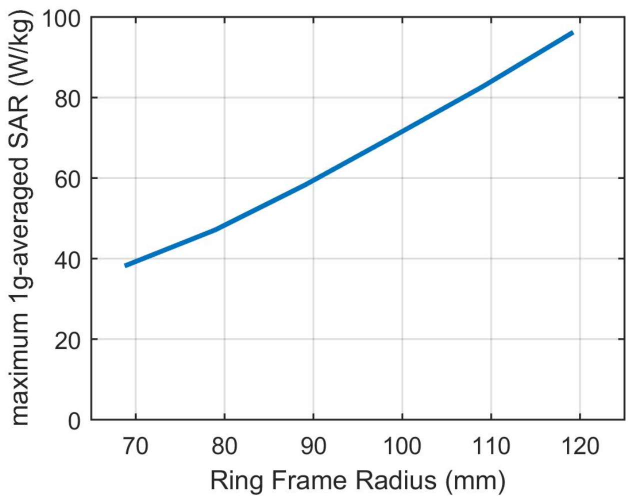

Figure 4.33. Maximum 1g-averaged SAR versus ring frame radius based on previous worst case.

Table 4.9. Maximum 1g-averaged SAR for different ring frame radius based on previous worst case

Radius(mm)	Incident B_1 normalized total power(W)	Maximum 1g-averaged SAR(W/kg)
69	151.14	38.4
79	155.48	47.2
89	159.31	58.2
99	165.50	70.4
109	171.54	82.7
119	181.69	95.9

4.3.3 Strut Length

Since the largest ring frame size configuration is determined to be the worst case, we now focus on the strut length effect using the 119 mm ring frame size. Strut length in this study is defined as the vertical distance between the two ring frames. A large number of different strut lengths are tested to form a comprehensive investigation. The strut lengths in our study range from 75 mm to 395 mm, with an increment of 40 mm. With the completion of full-wave EM simulations, the 1g-averaged SAR is calculated using incident B_1 field normalization. Table 4.10 shows the calculated maximum 1g-averaged SAR along with the incident B_1 normalization factor for different strut length configurations.

Table 4.10. Maximum 1g-averaged SAR for different strut heights based on previous worst case

Strut height(mm)	Incident B_1 normalized total power(W)	Maximum 1g-averaged SAR(W/kg)
75	184.29	35.1
115	183.61	68.9
155	181.69	95.9
195	178.96	115.2
235	175.41	127.1
275	172.27	135.7
315	168.32	138.4
355	164.95	138.3
395	161.19	136.6

Figure 4.34 shows the trend between 1g-averaged SAR and strut length. The 1g-averaged SAR value reaches its maximum at a strut length of 315 mm. As the strut length grows from 75 mm to 315 mm, the maximum 1g-averaged SAR increases dramatically from 35 W/kg to 138 W/kg. When strut length becomes larger than 315 mm, the maximum 1g-average SAR is kept almost constant. Opposite to the increasing trend of maximum 1g-averaged SAR, the incident B1 normalization factor displays a decaying tendency when the strut length grows.

The phenomenon described above is related to the wavelength of electromagnetic waves. In an MRI RF exposure, the circular external fixation devices, which are made of metallic components, act as receiving antennas and capture the RF power generated by the MRI RF coil. As a result, intensive induced surface current is generated. The

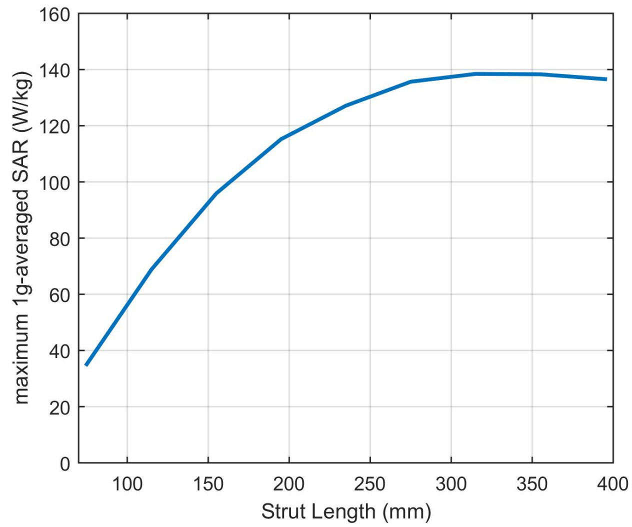

Figure 4.34. Maximum 1g-averaged SAR versus strut height based on previous worst case.

induced power is then dissipated inside the phantom or the human body. For 64 MHz signals, the wavelength is about 4.68 m in air. When the strut length is relatively small compared to half wavelength, the circular external fixation device does not efficiently receive RF power. As the strut length becomes larger, efficiency improves due to the antenna effect. More intensive current is induced on the circular external fixation devices by receiving MRI RF power. Furthermore, when the length of the strut is comparable with the half wavelength, the circular external fixation device tends to have a resonance phenomenon at a certain strut length. Even though the induced power becomes lower, the induced electromagnetic field grows dramatically. The intense electromagnetic field leads to high maximum 1g-averaged SAR.

4.3.4 Insertion Angle

In previous sections, the screws are inserted into the leg phantom perpendicularly. In most cases, the screws in circular external fixation devices can be inserted into human body at different angles. Different insertion angles may have an effect on the MRI RF coil induced heating effects. In this section, insertion angle studies are conducted numerically.

The insertion angle is defined as the angle between the screw and the perpendicular line to the surface of phantom gel. As depicted in Figure 4.35, it is also the elevation or depression angle measured from the screw to the plane of ring frame since the circular external fixation is aligned with the leg phantom. The insertion angle varies from -20° to 20° with an increment of 5°. These insertion angles examined here cover the most common cases in clinical use. When we change the insertion angle, the insertion depths are kept at 25 mm to remove the impact of different insertion depth.

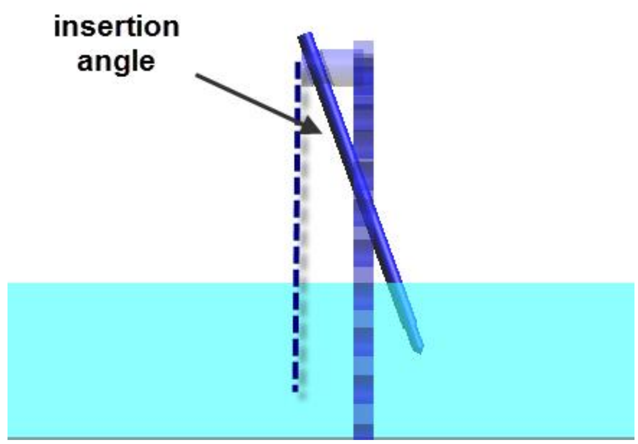

Figure 4.35. Illustration for insertion angle.

Simulation results can be viewed in Table 4.11. When the insertion angle is increasing from -20° to 20°, there is an increasing trend for the maximum 1g-averaged SAR. By inspecting the tendency in Figure 4.36, small angle variation will lead to dramatic maximum 1g-averaged SAR change at large insertion angles.

To explain the dramatic change of maximum 1g-averaged SAR caused by the insertion angle, we need to examine the electric field of the incident scenario. Without the presence of the medical device, the vector electric field inside the leg phantom is displayed as in Figure 4.37. The electric field within the leg portion is generally in the vertical direction.

When the screws are inserted into the leg phantom, induced surface current is generated at the screw surface. Due to the antenna effect of the screw, the induced

Table 4.11. Maximum 1g-averaged SAR for different insertion angles based on previous worst case

Angle(°)	Incident B_1 normalized total power(W)	Maximum 1g-averaged SAR(W/kg)
-20	161.25	75.9
-15	162.69	80.3
-10	164.38	86.7
-5	166.14	109.9
0	168.32	138.4
5	170.47	178.8
10	172.88	222.5
15	176.12	280.8
20	179.04	341.3

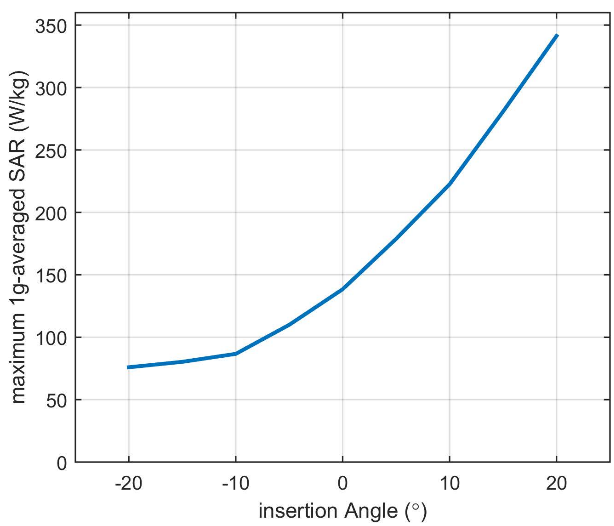

Figure 4.36. Maximum 1g-averaged SAR versus insertion angle based on previous worst case.

surface current is coupled with the tangential part of the incident electric field. For a large insertion angle, the screw is aligned with the direction of incident E field, and thus a large tangential electric field can be observed. The large tangential component of the electric field is interacting with the screw, and induces a large amount of RF power. On the other hand, when the insertion angle is small, although the screw can be coupled with a large tangential electric field, the opposite alignment of the screw and the electromagnetic field will result in field cancellation and thus reduce

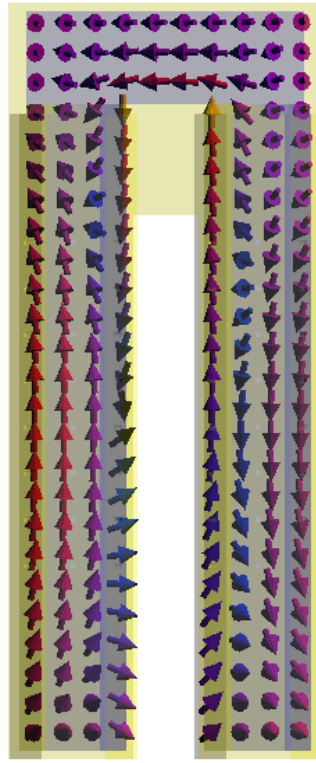

Figure 4.37. Vector electric field distribution in an unloaded leg phantom.

the efficiency of the receiving antenna. With less power received by the inserted screw, the energy deposited at the tip of the screw becomes lower.

4.3.5 Validation Process

To ensure that the worst-case heating configuration is captured, additional validation studies are performed in this section. In particular, the simulations will be based on the worst case in the previous sections and we change the components individually, keeping all other parameters constant. Different strut length, ring sizes, screws/wires configurations, and insertion angle will be analyzed using software. Four additional studies are performed to validate that the heating from these new configurations will not exceed the captured worst-case configuration.

The configurations for each validation simulation are listed in Table 4.12. By examining the maximum 1g-averaged SAR results using the incident B_1 normalization, the circular external fixation device with 3-screw configuration, 119 mm ring frame radius, 315 mm strut length and 20° insertion angle pointing outwards is guaranteed to be the worst cases of MRI RF induce heating.

Table 4.12. Validation process to ensure worst-case scenario is captured

Item	Change to	Incident B_1 normalized total power(W)	Maximum 1g-averaged SAR(W/kg)
worst case		179.04	341.3
length change	to 355	175.21	331.3
radius change	to 109	168.51	284.8
config change	to 2 screw 1 wire	177.37	254.6
number change	to 4 screw	180.72	310.7

4.4 Summary

With the help of numerical techniques, we are able to assess the RF heating effects of the circular external fixation devices. For the generic circular external fixation devices used in this study, the maximum heating locations are close to the tips of the screws that are inserted into the human body. Due to the presence of conductive loops, the circular external fixation can receive a large amount of RF power, and the induced energy is dissipated inside the human body or the phantom gel. Most of the energy is concentrated at the tips or edges of the impinging screws, and thus causes significant RF heating effects near screw tips.

In order to appropriately quantify the RF heating effects, the maximum 1g-averaged SAR is used as an indicator of temperature rise. A leg phantom is designed and numerically examined to represent human legs. The field distribution for an unloaded leg phantom inside the MRI RF coil has been shown to be the same as the field distribution of the human model when the B_1 field normalization is used. The incident B_1 field normalization method is proposed for the loaded leg phantom and human model. Simulation result has shown that the leg phantom is representative for the human model. When parameters such as insertion depth, ring frame size, strut length and loading positions are changed, the leg phantom and the human model present the same trend in MRI RF coil induced heating effects.

Numerical investigation based on the leg phantom is then carried out after we confirm the consistency of the leg phantom with the human model. To search for the worst case configuration of the circular external fixation device, the screws/wires configuration, ring frame radius, strut height, and insertion angle are swept in a large range. The final validation process guarantees the capture of the worst case scenario for the circular external fixation device.

The mechanism of how different parameters affect the MRI RF coil induce heating effect is discussed. Power dissipation is more concentrated with the absence of the wire component. Fewer screws and smaller insertion depths make the power dissipation even more focused and thus aggravate the RF induced heating effect. A large ring frame will easily receive the RF power produced by the coil, which leads to high local maximum SAR. The antenna effect explains the impact of the strut length on the RF induced heating, as well as the influence of the insertion angle.

Through numerical simulation of circular external fixation devices, the normalized 1g-averaged local SAR for the worst-case configuration can be as high as 341 W/kg. By applying the Pennes Bioheat Equation, the estimated temperature rise in the leg phantom is about 17 °C. With no doubt this high thermal effect will result in permanent tissue damage. There is an urgent requirement for the reduction of the tremendous temperature rise. In the next chapter, techniques that can potentially reduce the heating effects will be applied to this worst case configuration.

Chapter 5

Reduction of MRI RF Heating Effects for Circular External Fixation Devices

In the previous chapter, it was shown that all screw configuration with fewer screws, large ring frame size and relatively large strut length and the maximum insertion angle pointing outwards may lead to the worst case MRI RF coil induced heating. By avoiding those worst-case scenarios, a reduction of MRI RF induced heating can be expected. In practical use, however, the form of the circular external fixation devices is fixed due to the optimum stability requirement. Therefore the RF induced heating effects can be hardly reduced by changing the structure. The use of absorption material has been proved effective on modular external fixation devices. For circular external fixation devices, the technique can potentially reduce the RF heating effects. Based on the worst case configuration from the previous study, the technique of using absorption material is examined with caution in this chapter.

5.1 Using Absorption Material around the Screws

As illustrated in Chapter 3, the use of absorption material can help absorb the RF energy and change the power distribution for external fixation device. The consumption of RF power in the absorption material restrains the power that can propagate into the phantom gel or human body. For a single frequency, the absorption capability of the material is modeled as the electrical conductivity. In this study, the conductivity is varied from 10^{-4} S/m to 10^{3} S/m to cover the common range of electrical conductivity of the absorption material.

The simulation setup is depicted in Figure 5.1. The leg phantom is placed in the middle of the MRI RF coil, with the circular external fixation device loaded inside the leg phantom. The position and structure of the circular external fixation is the same as the worst case scenario determined by the previous chapter. Six tubular structures with inner diameter of 5 mm and outer diameter of 7 mm are placed at the connection part of screws and clamp as illustrated in Figure 5.2. The length of the absorption material tube should be long enough to make sure the whole connecting part is covered.

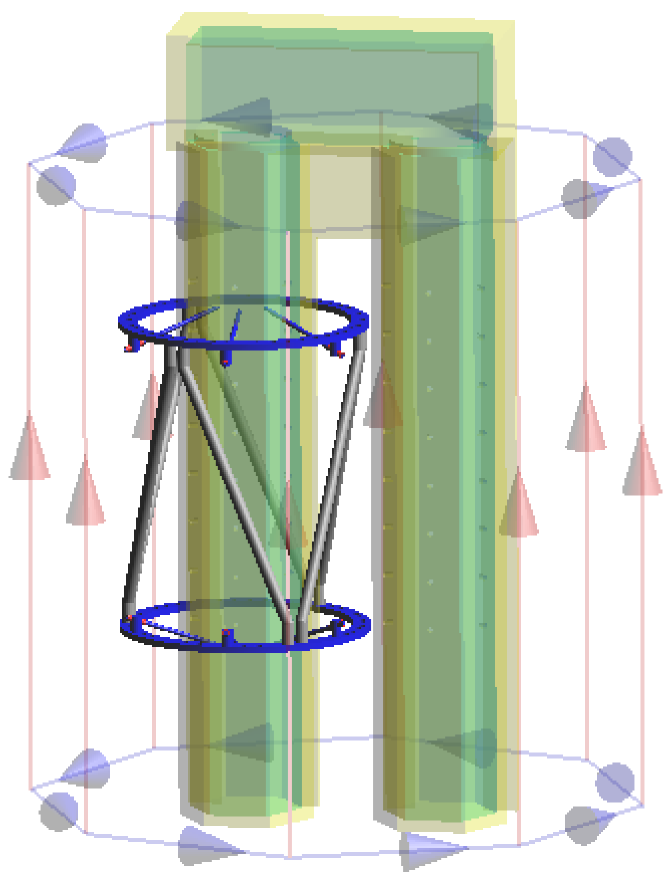

Figure 5.1. Simulation setup for investigation on using absorption material.

To study the effect of different absorption materials on induced RF heating of the device, five categories of materials with different absorption characteristics are examined. Each category has its individual dielectric constant $\varepsilon_r = 2, 3, 5, 7, 9$, and the electrical conductivity varies from 10^{-4} to 10^{3} S/m. The electromagnetic properties of the leg phantom gel and leg phantom shell are listed in Table 4.1. Once

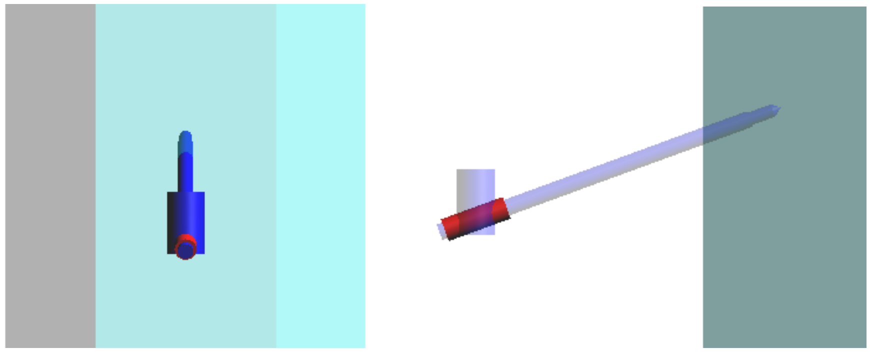

Figure 5.2. Front view (left) and side view (right) of absorption material that covers the connection of screw and clamp.

the simulation was complete, 1g-averaged SAR along device pins were calculated for further analysis.

Three typical examples are chosen to demonstrate the effect of using absorption material. When $\varepsilon_r = 7$, $\sigma = 10^3$ S/m, the maximum heating location occurs at the tips of the screw. Figure 5.3 shows the maximum 1g-averaged SAR is 346 W/kg. The high SAR value is expected since at 64 MHz, the loss tangent of the material is

$$\tan\delta = \frac{\sigma}{\omega\varepsilon} = \frac{\sigma}{2\pi f \varepsilon_0 \varepsilon_r} = 4.01 \times 10^4, \tag{5.1}$$

where ε_0 is the dielectric constant in free space. Because of the large loss tangent, the absorption material behaves like PEC. The result is similar to the worst case in the previous study. The induced surface current generates a large amount of induced RF power, which is dissipated into the phantom gel or human body through the screw. The power injected into the leg phantom is highly focused. Within a 1 cm range, the power level decays from the maximum value to -20 dB. Localized energy deposition near the tips of the screws leads to a significant MRI RF heating effect.

When the tubes are made up of pure insulating material ($\varepsilon_r = 7$, $\sigma = 0$ S/m), the maximum heating location also appears at the tips of the screws. The maximum

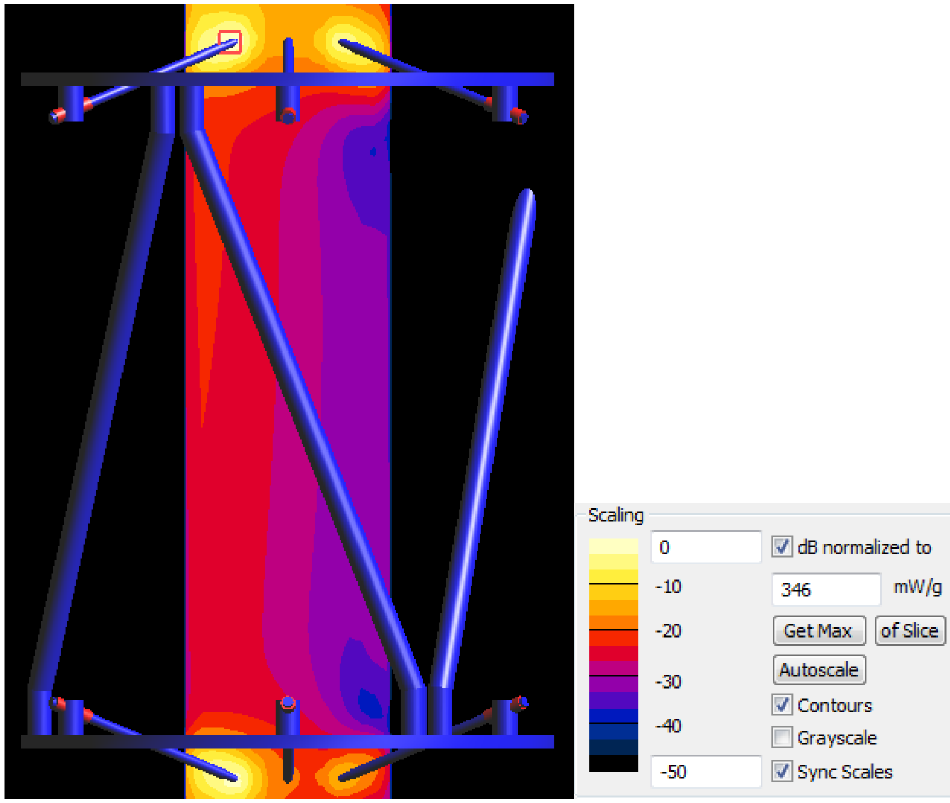

Figure 5.3. SAR distribution when absorption material ($\varepsilon_r = 7$, $\sigma = 10^3$ S/m) is used.

1g-averaged SAR is reduced to 71.9 W/kg. Using insulating layers can help reduce the MRI RF heating effects because it can block the current flowing into the phantom gel or human body. With the help of the insulating layer, the maximum 1g-averaged SAR has been reduced significantly from 346 W/kg to 71.9 W/kg.

The third example is shown when $\varepsilon_r = 7$, $\sigma = 10^{-2}$ S/m. While the 1g-average SAR pattern inside the leg phantom is still the same as in the previous cases, the red cubic box in Figure 5.4 indicates that the significant heating location occurs at the absorption material tubes. The maximum 1g-averaged SAR at the absorption material tube is 406 W/kg. By inspecting the maximum local SAR within the leg phantom, the SAR value is as low as 56.5 W/kg. Compared to the worst case when no absorption material is used, the 1g-averaged SAR inside the leg phantom gel is reduced by 83.4% from 341 W/kg to 56.5 W/kg.

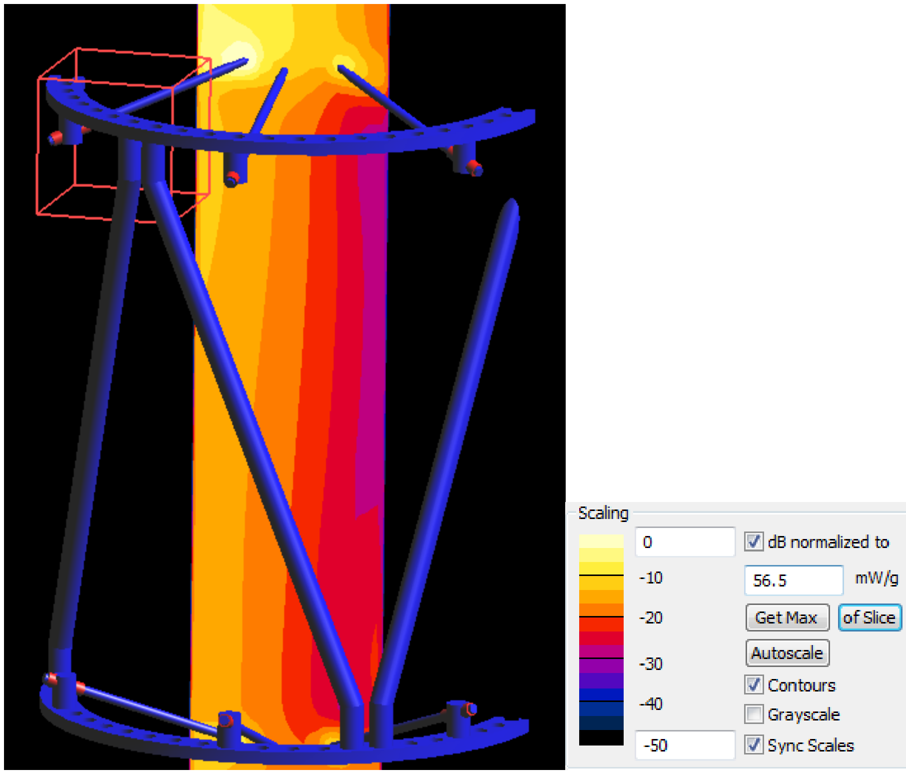

Figure 5.4. SAR distribution when absorption material ($\varepsilon_r = 7$, $\sigma = 10^{-2}$ S/m) is used.

For different dielectric constants and conductivity, the RF heating effect is expected to vary. Figure 5.5 shows the maximum 1g-averaged SAR's dependence on conductivity for various relative dielectric constants. It is obvious that this curve has the same trend as for the modular external fixation devices. When appropriately choosing the electromagnetic characteristics of the absorption material, we are able to reduce the MRI RF heating effects significantly by simply attaching the material in the connection part of the screws and the clamp. The maximum 1g-averaged SAR can be reduced from 346 W/kg to 22.6 W/kg.

The reason absorption material is effective for the MRI RF induced heating reduction for circular external fixation device can be explained using the same logic as for the modular external fixation case. SAR is defined as $\sigma E^2/2\rho$. When conductivity is either to low or too high, the dissipated energy in the absorption material approaches

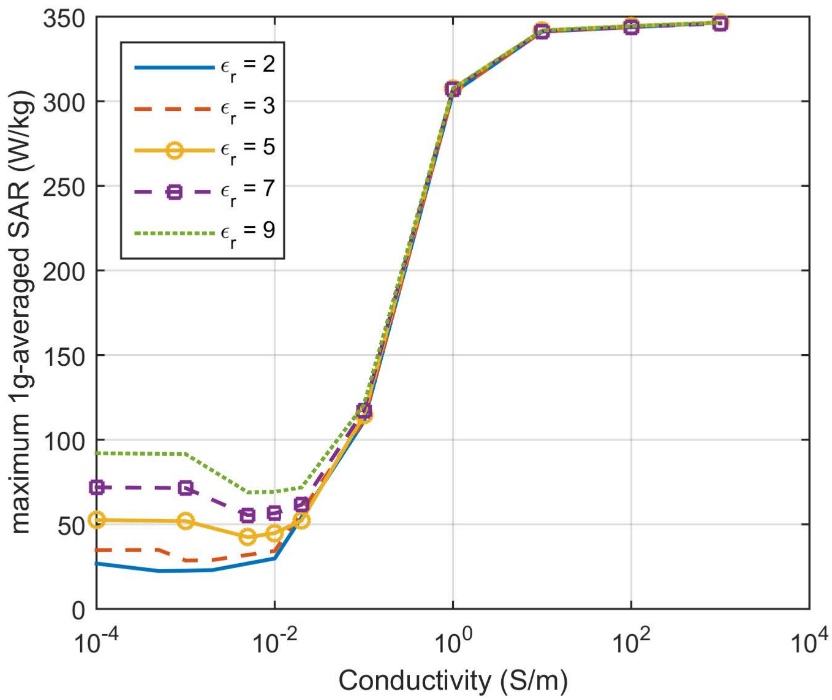

Figure 5.5. Maximum 1g-averaged SAR versus conductivity for different dielectric constant.

zero. Because there is no power dissipation in the absorption material, all energy enters into the phantom gel and thus higher SAR is expected in the gel. When conductivity is in a certain range, neither conductivity nor E-field approaches zero. The power consumption in the material reaches its maximum. Energy that can propagate in the phantom becomes less intense.

5.2 Using Absorption Material at Various Locations

While the ring frames and the struts receive power from the MRI RF coil, the induced energy can penetrate into the phantom gel through the inserted screws. The utilization of absorption material has been shown effective to reduce RF induced heating for circular external fixation devices at the connection part of the screws and the clamps. The original purpose of choosing this location is to prevent the RF induced current from flowing into the screw. While using absorption material can help inhibit the power consumption in the leg phantom gel, it is also possible that this material can change the induced current distribution. When placed at optimal locations, the absorption material can be efficient for reduction of RF induced heating. A different location is tested using numerical simulations.

To determine the optimal locations, the induced current distribution of the worst case circular external fixation is plotted in Figure 5.6. The induced current generated by the struts is propagating into the leg phantom through the clamps and screws. Other than the connection between the clamp and the screw, current conduction is observed at the connection between the ring frame and the clamp. With the presence of appropriate absorption material at this connection, most of the current will be suppressed.

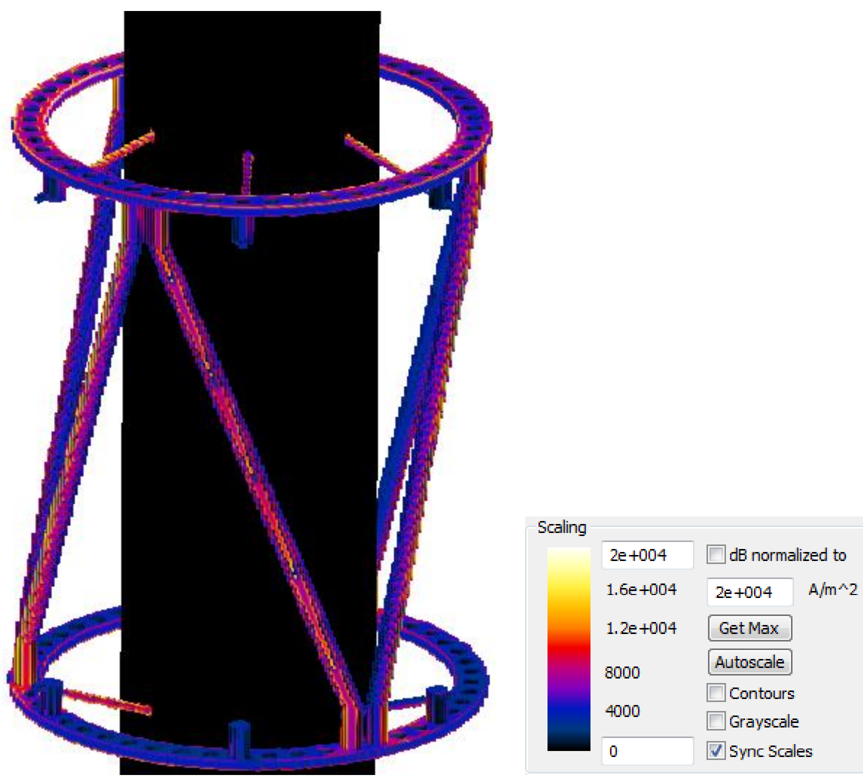

Figure 5.6. Induced surface current distribution on typical circular external fixation device.

The placement of the absorption material in the new location is depicted in Figure 5.7. The shape of the absorption material is tubular with an inner diameter of

12 mm and outer diameter of 15 mm. The length of the material is 10 mm that ensure all the connecting part is covered. From the previous study, it has been shown that the absorption material with low permittivity can achieve the most significant MRI RF induced heating. Here the case $\varepsilon_r = 2$, $\sigma = 0.001$ S/m is chosen. The maximum 1g-averaged SAR inside the phantom is reduced to 22.1 W/kg. Using absorption at a different location tends to have the same impact.

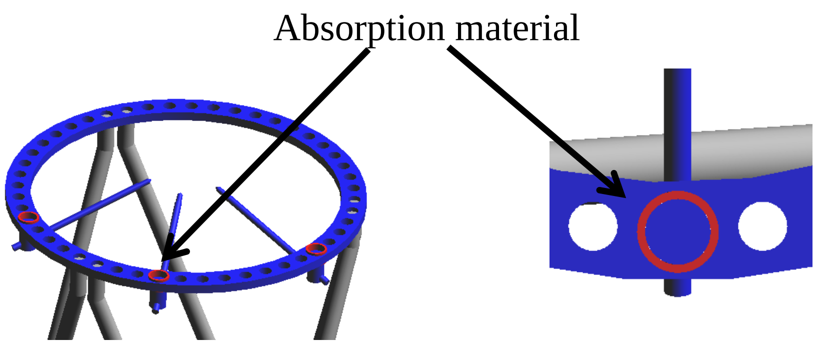

Figure 5.7. The placement of absorption material between the connection of clamp and ring frame.

It is possible to apply the absorption material at both locations. By using the absorption material using the same electrical properties as previous case, the thermal effect can be viewed in Table 5.1. The use of absorption material at both locations will produce a better reduction on MRI RF induced heat.

Table 5.1. Using absorption at different location of circular external fixation device

absorption material location	maximum 1g-averaged SAR(W/kg)
none	341
screw and clamp	22.6
clamp and ring frame	22.1
both	15.6

5.3 Experimental Validation

By numerical simulation, it has been shown that using absorption material can help reduce the MRI RF induced heating effect. In addition to the simulation studies, experiments were carried out in the lab. Figure 5.8 shows a commercially available circular external fixation device. The ring frame diameter is about 20 cm, which can fit into the hexagon-shaped leg phantom. The 6 struts which connect the two ring frames improve the stability of the external fixation device. Millimeter graduations on each strut ensure the strut are of the same length and are aligned to the circular external fixation frames. All the components are made of titanium to reduce the weight. By adjusting the screw location, strut height and insertion depth, the circular external fixation can fit into the leg phantom.

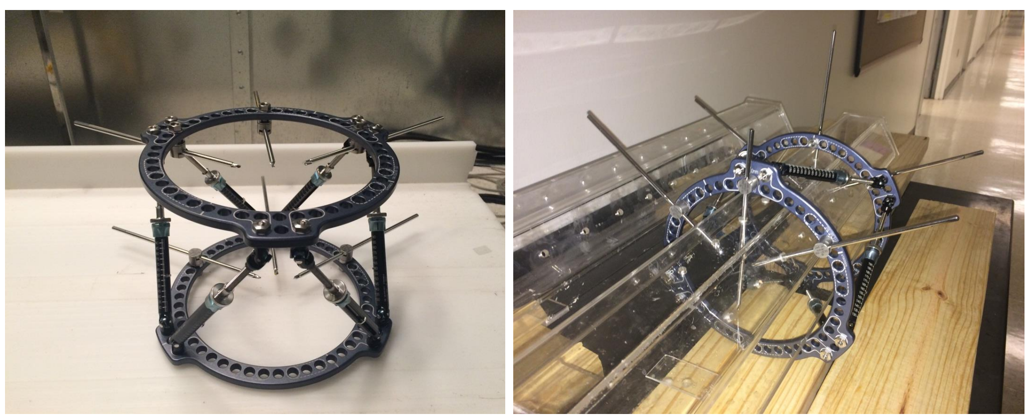

Figure 5.8. Circular external fixation device that can fit in the leg phantom.

In the experiment, the circular external fixation, together with the leg phantom, was loaded into ZMT MITS1.5 system. The complete experiment setup is shown in Figure 5.9. Wooden boards were used as the support of the leg phantom to allow circular external fixation placement. The insertion depths were fixed at 25 mm and the temperature probe was attached at the tip of the screw using rubber band. Before the leg phantom is filled with gel, we use engineering clay to cover the holes on the leg phantom. Two extra fiber-optical temperature probes were used. One was placed

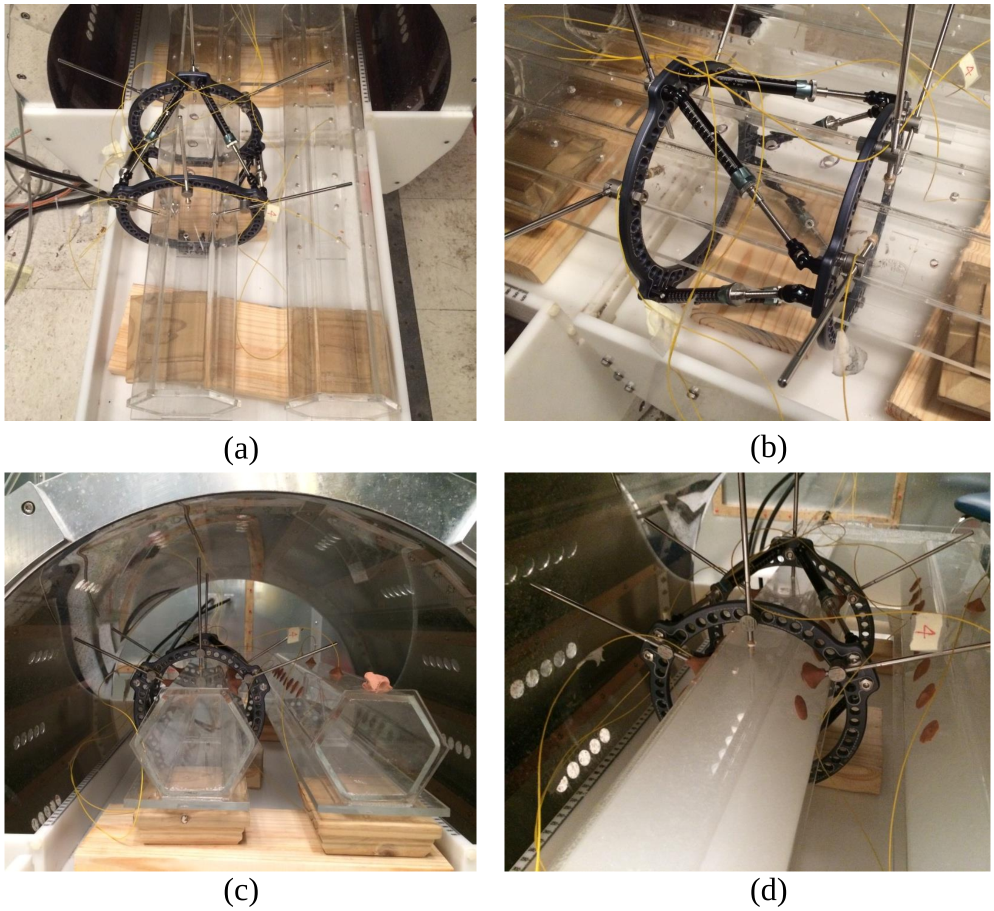

Figure 5.9. Experiment setup for leg phantom loaded with circular external fixation: (a)use wooden frame to support leg phantom (b) attach probe to the tip of the screw (c) use engineering clay to cover the holes (d) fill with gel.

at the tip of the screw on the other ring frame, and the other was inserted into the leg on the other side for background temperature monitoring.

As per ASTM F2182 recommendations, the leg phantom with the circular external fixation device was exposed into the MRI RF coil for 15 min. The temperature was continuously recorded for 2 min after MITS1.5 system was powered off. The time resolution was 1 s, and the resolution of the temperature probe was 0.2 °C.

The same absorption material, provided by Molex Inc., Lisle, IL, USA, is shown in Figure 5.10. The material is cut to be the same length to maintain constant thickness when wrapped at the connecting part between clamps and screws. Two experiments were conducted for comparative study: one was using absorption material and the

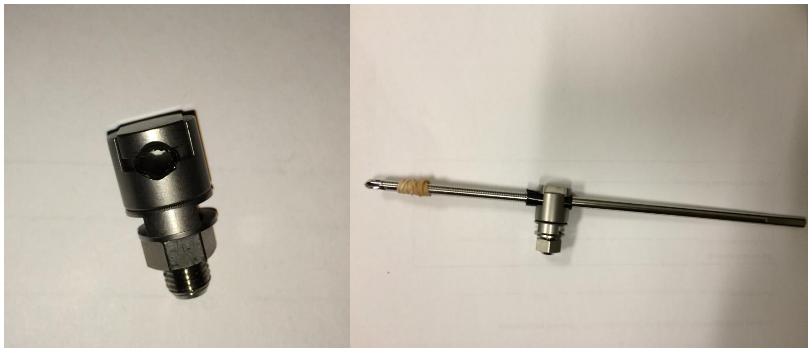

Figure 5.10. Absorption material that is wrapped at the connecting part between clamp and screw.

other was directly put inside the birdcage. The temperature increase plot can be viewed in Figure 5.11. The temperature increase for the circular external fixation device with 15 min exposure inside MRI RF coil can be as high as 4.1 °C. When the absorption material is applied at the connecting part between all the screws and clamps, the temperature rise is reduced to 2.6 °C.

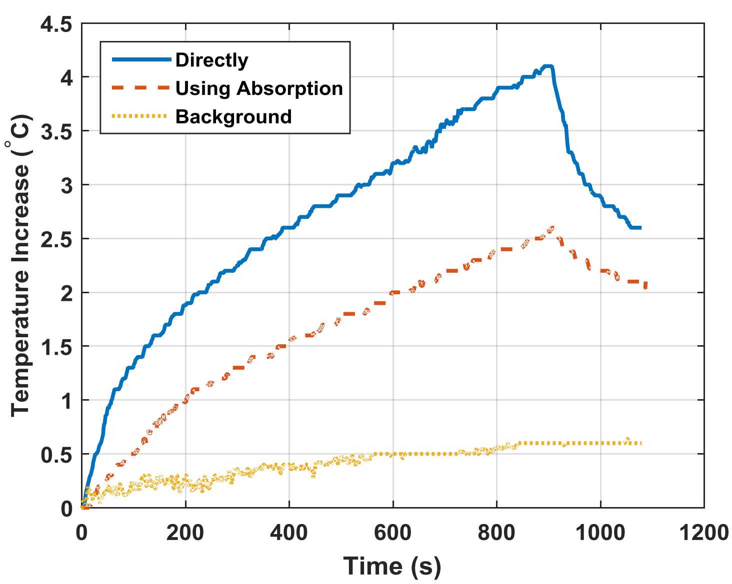

Figure 5.11. Temperature increase measurement for circular external fixation device with/without absorption material.

5.4 Qualitative Explanation using Circuit Model

As seen in Figure 3.7 and Figure 5.5, the behavior of 1g-averaged SAR in the leg phantom gel in the low conductivity range is different. Unlike the findings suggested by Liu et al. [26], the high permittivity insulating material (ε_r = 5, 7, 9) can also reduce the MRI RF induced heating effectively for circular external fixation device. This is due to the structure of circular external fixation. For the circular external fixation device, the formation of conductive loops can be viewed as inductors at 64 MHz. The capacitive coupling that causes the induced current to flow into the screw can be compensated by the inductance produced by the circular external fixation. The cancellation of the capacitive coupling prevents the induced RF power from entering the screw through the insulating layers. As the permittivity of the insulating layers increases, the capacitive couple effect becomes significant. An extreme case of insulating layers with a relative dielectric constant of 60 has been simulated. The 1g-averaged SAR is 461 W/kg near the tip of the screw, which is even higher than the local 1g-averaged SAR without using any absorption material.

The inductance effect of the circular external fixation is an indicator that the RF heating reduction by using absorption material can be explained by the circuit theorem. Based on the induced current flow in the system, a circuit model is built to qualitatively demonstrate the heat reduction mechanism.

As shown in Figure 5.12, the induced MRI RF field is modeled as a voltage source since the RF induced heating is closely related to the incident E field. Because most of the power is dissipated inside the leg phantom gel, a load resistance is used to represent the leg phantom. The circular external fixation device, which is set as PEC in EM simulations, can be viewed as an inductance because no conductivity loss exists. The circular external fixation device acts as a receiving antenna. The induced current is generated on the surface of the device, and propagates into the phantom gel.

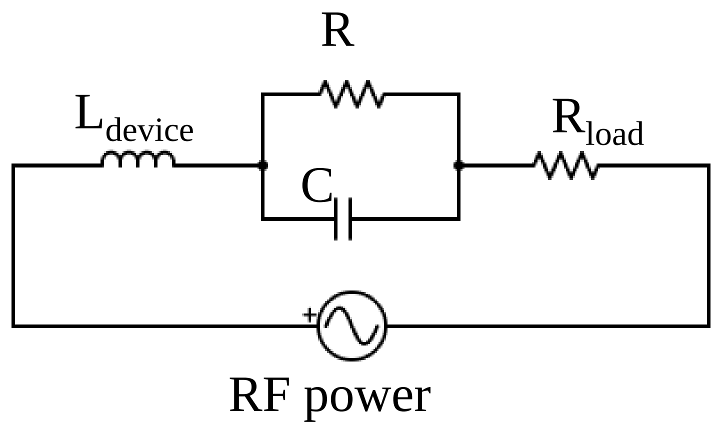

Figure 5.12. Circuit model for reduction of MRI RF coil induced heating using absorption material.

The induced current flows into the phantom gel through the absorption material. The tubular absorption material is modeled as a capacitor parallel with a resistor. This assumption is reasonable because the current is flowing radially on the tubular absorption material, from the clamp into the screw. The absorption material is operating as a cylindrical capacitor with lossy media inside it. The whole circuit is in series due to the continuity of the induced current. To get an approximately correct response from the circuit, the characterization of each lumped element in the circuit plays an important part. A rough estimation for each circuit component in Figure 5.12 is given below based on the practical size of each component.

5.4.1 Load Resistance

To calculate the load resistance, the leg phantom is treated as a large resistor. The screws that are inserted into the phantom gel can be viewed as electrodes which conduct current. By rough estimation, the load resistance is

$$R_{load} = \frac{1}{\sigma} \cdot \frac{L_{phantom}}{\pi r_{leg}^2}, \tag{5.2}$$

where σ is the conductivity of the leg phantom, $L_{phantom}$ is the estimated effective length of the leg phantom, and r_{leg} is the estimated radius of the leg. Here we choose

σ =0.47 S/m, $L_{phantom}$ = 400 mm, and r_{leg} = 55 mm.

5.4.2 Device Inductance

The inductance of the circular external fixation device is produced from the conductive loop formed by the metallic struts and ring frames. Just to provide a basic estimation, we simply consider the inductance of one strut rather than the whole structure. The inductance of the straight thick wire with finite length is calculated by

$$L = \frac{\mu_0}{2\pi}\left(l \ln\left[\frac{1}{c}\left(l + \sqrt{l^2 + c^2}\right) - \sqrt{l^2 + c^2} + c + \frac{l}{4}\right]\right), \tag{5.3}$$

where l is the length of the wire, c is the radius. When we choose l = 350 mm, c = 6 mm, the inductance of the strut can be obtained. Although it is not the exact inductance of the circular external fixation device, the actual inductance should be in the same range.

5.4.3 Capacitance and Resistance of Absorption Material

When modeling the capacitance and resistance of the absorption material, the current distribution flowing in the tube is of great importance. The current flow on the absorption material tube is plotted in Figure 5.13. Since most of the current is flowing radially, the circuit model for the absorption material tube is designed to be cylindrical capacitor with lossy media inside it.

For cylindrical capacitor with lossy media, the capacitance and resistance of the absorption material are calculated by

$$C = \frac{2\pi\varepsilon_0\varepsilon_r h}{\ln(b/a)} \tag{5.4}$$

and

$$R = \frac{\ln(b/a)}{2\pi\sigma h}, \tag{5.5}$$

where a, b and h are the inner radius, outer radius, and height of the absorption

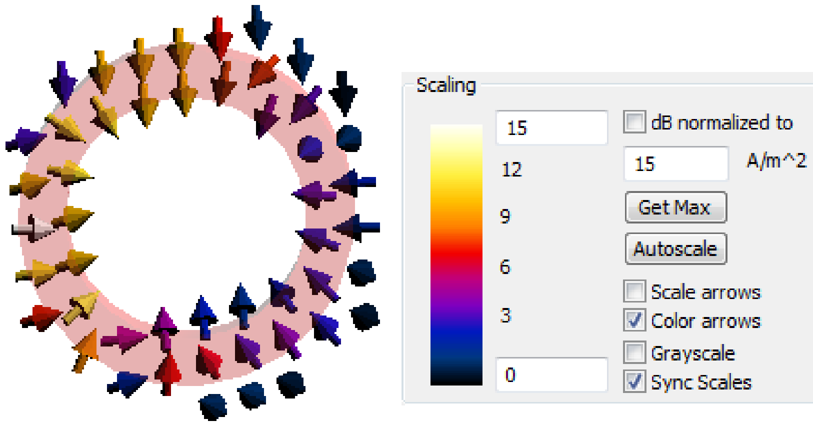

Figure 5.13. Current distribution inside the absorption material.

material, and ε_r and σ are the relative permittivity and conductivity. For rough estimation, $a = 2.5$ mm, $b = 3.5$ mm, $h = 15$ mm. This approximation is good enough to characterize the thin layer absorption material tube.

The MRI RF induced heating effect is quantified by the maximum 1g-averaged SAR. For particular simulation environment, the maximum 1g-averaged SAR is proportional to the power dissipation within the leg phantom due to the similar field distribution. Hence in the circuit model, the power consumption of the load resistor is used to represent the maximum 1g-averaged SAR. Figure 5.14 shows how the conductivity of the absorption material changes the normalized power dissipated by the phantom leg.

The curve reflects the same trend as the simulation results. When the conductivity is very large, R = 0, the capacitance in the circuit model is shorted and cause no effect on the delivered power. When the conductivity is zero, R is an open circuit. The capacitor, the inductor and the load resistor form a series resonant circuit. The delivered power reaches its maximum when the resonance condition matches

$$\omega^2 LC = 1, \tag{5.6}$$

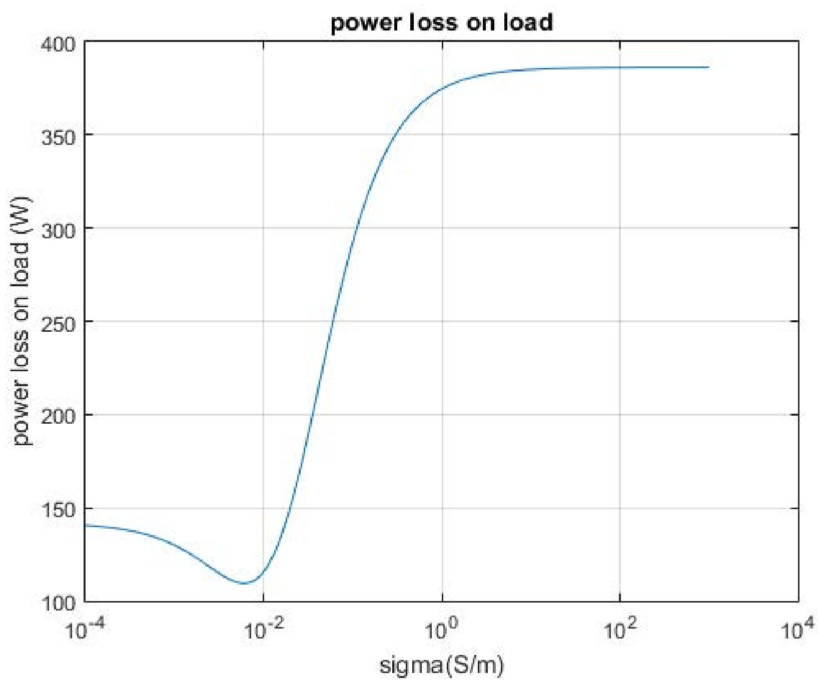

Figure 5.14. Normalized power loss on load resistor versus conductivity using circuit model.

and a permittivity that is too high or too low will detune the circuit and restrain the delivered power. For fixed permittivity, when the conductivity is properly chosen, the power dissipated on the load will be

$$P = I^2 R_{load}, \tag{5.7}$$

where

$$I = \frac{V}{j\omega L + \frac{R(j\omega C)^{-1}}{R+(j\omega C)^{-1}} + R_{load}}. \tag{5.8}$$

The minimum will be achieved when the conductivity is in the middle range.

The equivalent circuit model also throws light on the phenomena that high permittivity will make the heating effects even higher. Figure 5.15 shows how the curve varies for different permittivity. When the permittivity increases, the capacitance of the equivalent circuit model also increases. For low permittivity cases, the circuit is inductive. Increasing the capacitor means to reduce the reactance part and tune the circuit. The power dissipation is thus growing to reach the maximum at resonance. However, when the capacitance becomes even larger, the circuit becomes capacitive and gets detuned. As shown in Figure 5.15, the MRI RF induced heating effects become less significant when ultra-high permittivity absorption material is chosen.

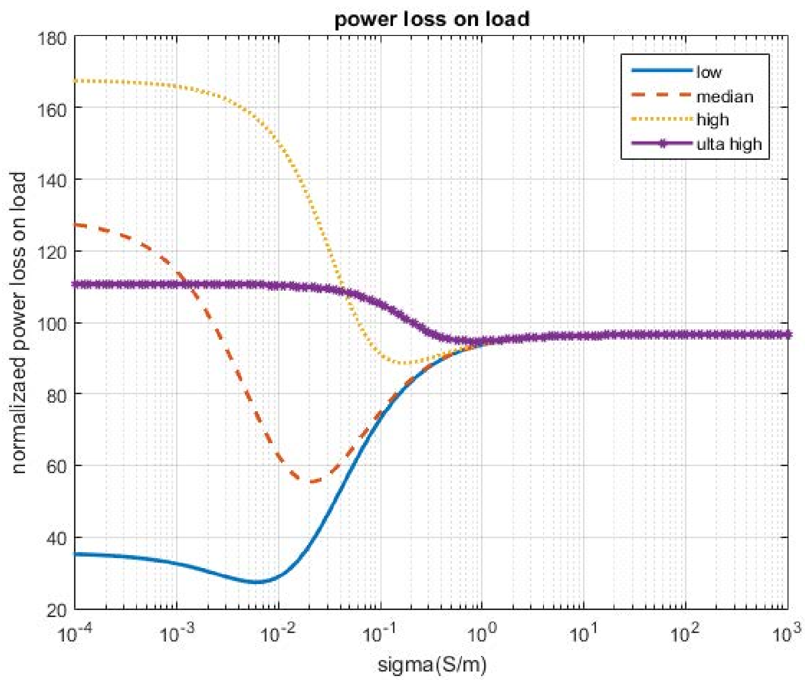

Figure 5.15. Normalized power loss on load resistor change with conductivity and permittivity using circuit model.

In conclusion, the circuit model proposed in this chapter agrees with the simulation results. The introduction of the absorption material has the effect of adding a capacitor that detunes the circuit in parallel with a resistor that dissipates part of the induced power.

Chapter 6

Preliminary Error Quantification

Measurements are subject to uncertainty. A measurement result is only complete if it is accompanied by a statement of the level of confidence. In most MRI-related standards, an uncertainty budget is required for estimating the uncertainty of measurements or simulations. While a lot of factors may result in temperature change in MRI RF coil induced heating measurement, only selected parameters that affect the uncertainty in temperature measurement is analyzed in this chapter. Instead of directly carrying out experiment to investigate the uncertainty, computational models are used to give a preliminary error quantification. The uncertainty comes from either simulation software or experimental settings, which will be discussed in this chapter. An uncertainty budget based on the preliminary study of the selected parameters is given by combining the simulation uncertainty and experimental uncertainty.

To determine the impact of individual parameters, pairs of simulations with only a single parameter changing have been compared. Assuming linear dependence of the measurement values on the varying parameter, a sensitivity factor f_i can then be determined for each parameter. Multiplying the sensitivity with the standard deviation s_i of the parameter uncertainty results in the uncertainty contribution of this parameter. The standard deviations are small for geometrical parameters such as the probe location which can be accurately determined and large for parameter such as the material parameters. For preliminary investigation, the selected parameters are considered independent to each other. Therefore the individual uncertainty contributions can be combined according to $\sqrt{\sum (s_i f_i)^2}$.

6.1 Simulation Uncertainty

Numerical models are the primary way we have to estimate the MRI RF heating effects. By using 3D EM full-wave software, we are able to calculate the field distribution in or around the location of interest with complicated environment and arbitrary shape medical device that we cannot derive an analytical solution. The simulation results, however, may not reflect the real situation. Indicating the level of confidence will help determine the accuracy of the simulation. The simulation uncertainty comes from either simulation settings before simulation or the post-processing portion after we obtained the results. The major parameters that affect the simulation results are absorbing boundaries, simulation time, discretization and averaging. The effect of each part is discussed in this section.

The simulation uncertainty is analyzed by comparing the simulation result with the known solution. For a simple structure, an analytical solution can be derived. Here we choose an example of electromagnetic scattering by a layered sphere. A $+z$ direction plane wave is incident onto a multi-layer sphere. The total field is produced by the superposition of the incident field and scattered field. The size and the electrical characteristics of the sphere, the calculated region of the plane wave, and the simulation settings are all comparable to the MRI RF coil simulations, producing a representative result.

As shown in Figure 6.1, a plane wave is propagating along positive z direction, the electric field is polarized in x direction. The radius of the inner sphere is 1 m and the thickness of the shell is 1 m. To mimic the simulation scenario, the electrical property of the inner sphere is set the same as the phantom gel: $\varepsilon_r = 80.38$, $\sigma = 0.47$ S/m, where the shell is set to plastic: $\varepsilon_r = 3.7$, $\sigma = 0$. The calculated region is a 3 m $\times$ 3 m $\times$ 3 m box centered at the origin. All the dimensions are comparable with the MRI RF coil simulations.

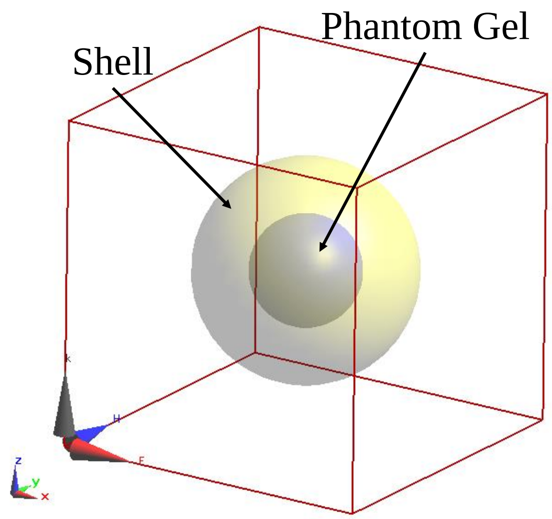

Figure 6.1. Illustration of multi-layer sphere scattering problem.

Because of the simple geometry, an analytical solution can be derived. In spherical coordinates, the electromagnetic fields are expressed in the series form of the products of the Riccati-Bessel functions, associative Legendre polynomials, and exponential functions. The solution to the scattering problem of a multi-layer sphere is acquired by solving a linear system for the field coefficients, which is constructed from the boundary conditions. The calculated and simulated E_{RMS} field distribution on the $y-z$ plane is plotted in Figure 6.2 and Figure 6.3. Similar pattern can be observed.

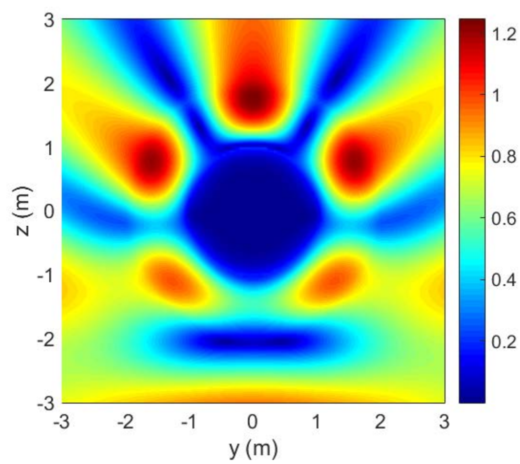

Figure 6.2. E_{RMS} field distribution on $y-z$ plane by analytical solution.

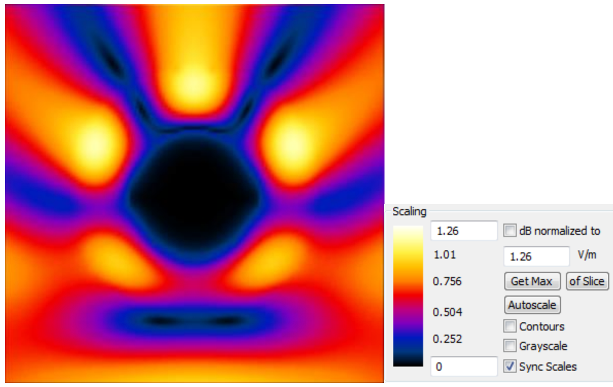

Figure 6.3. E_{RMS} field distribution on $y-z$ plane using simulation.

Figure 6.4 plots the RMS total electric field along the vertical z axis. To compare the simulated result and the analytical curve, the relative percentage error of the simulated result is defined by

$$error = \frac{\sqrt{\int \left(f\left(z\right) - f_0\left(z\right)\right)^2 dz}}{\int f_0\left(z\right) dz} \times 100\%, \tag{6.1}$$

where f is the simulated RMS total electric field, and f_0 is the analytical solution along the z axis. In this case, the relative error is 3.33%. For simulation uncertainty analysis, all discussions will be based on this example.

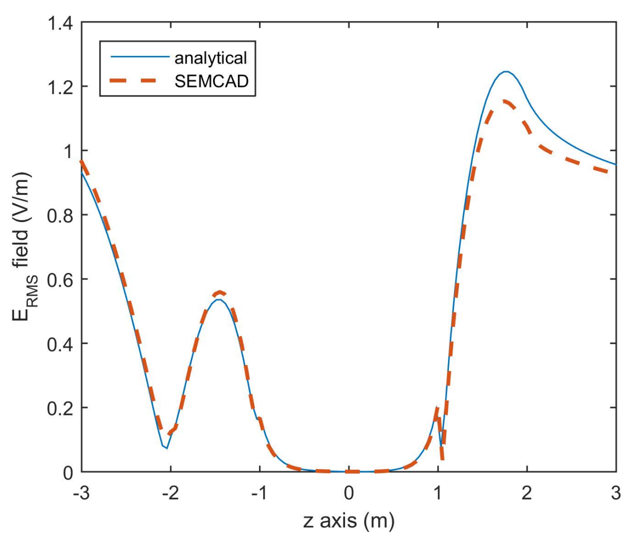

Figure 6.4. Comparison of E_{RMS} field along z axis between simulation and analytical solution.

6.1.1 Absorbing Boundaries

The FDTD scheme requires the application of absorbing boundaries to spatially limit the computational domain. Common differential equations do not allow the determination of the tangential field components located at the domain boundaries. The Absorbing Boundary Conditions (ABC) have been proposed to reduce reflections from the computational boundaries of the FDTD grid. In general, ABCs are essentially based on two principles: conditions imitating an absorbing material or conditions based on plane wave solutions to the wave equation. Within these methods, the tangential electric field components must be calculated to absorb the incident wave as effectively as possible.

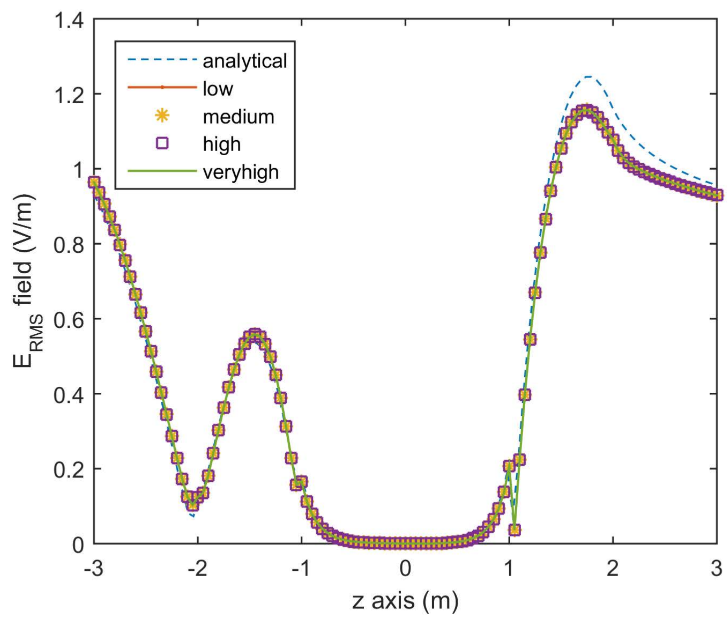

Figure 6.5. E_{RMS} field along z axis for different absorbing boundaries.

Different absorbing boundary settings may lead to different simulation result. When used for MRI simulation, the UPML/CPML boundary conditions are usually chosen. In SEMCAD X, four options are provided for the UPML/CPML absorbing boundary conditions: low, medium, high and very high. Each boundary setting is used for separate simulations. Figure 6.5 shows the E_{RMS} field distribution along z axis for different absorbing boundary conditions. Changing the UPML/CPML absorption level does not affect the result. The uncertainty for the absorbing boundary is 3.33%.

6.1.2 Simulation Time

The FDTD scheme is implemented in the time domain. For harmonic solutions, the software will automatically do the Fourier transform based on the waveform in time domain at every calculated location. The simulation time can have an impact on the Fourier transform result. The E_{RMS} distribution along z axis for different simulation time is shown in Figure 6.6. When the simulation time is larger than 20 periods, increasing the simulation time will not improve the simulation accuracy. Table 6.1 shows the relative error of different simulation time. For the 20 period simulation time setting, the error is 3.33%

Table 6.1. Relative error for different simulation period settings

Period	5	10	20	50	100
Error (%)	24.92	3.08	3.33	3.33	3.33

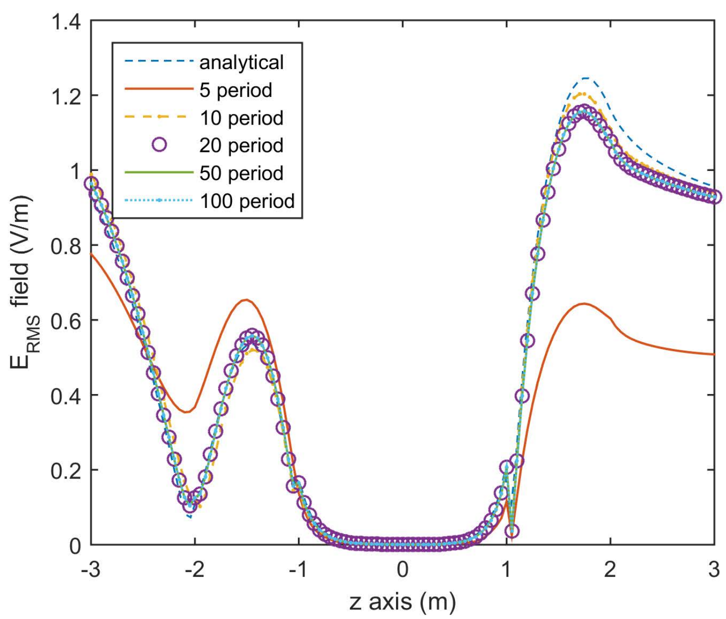

Figure 6.6. E_{RMS} field along z axis for different simulation periods.

6.1.3 Discretization

Numerical simulations could not be complete without the discretization of models. In SEMCAD X, the geometry of the models is partitioned into small voxels aligned in Cartesian coordinates. The smoothness of the model is lost due to discretization, which impacts the inaccuracy when calculating the electromagnetic field. The effect of different mesh sizes on the RMS total electric field along z axis is shown in Figure 6.7. Table 6.2 shows the relative error change with mesh sizes. The relative error is bounded within 3% when the mesh size is smaller than 30 mm.

Table 6.2. Relative error for different mesh size settings

Mesh size (mm)	80	70	60	50	40	30	20	15
Error (%)	4.61	5.69	3.66	3.33	3.05	2.92	2.49	1.67

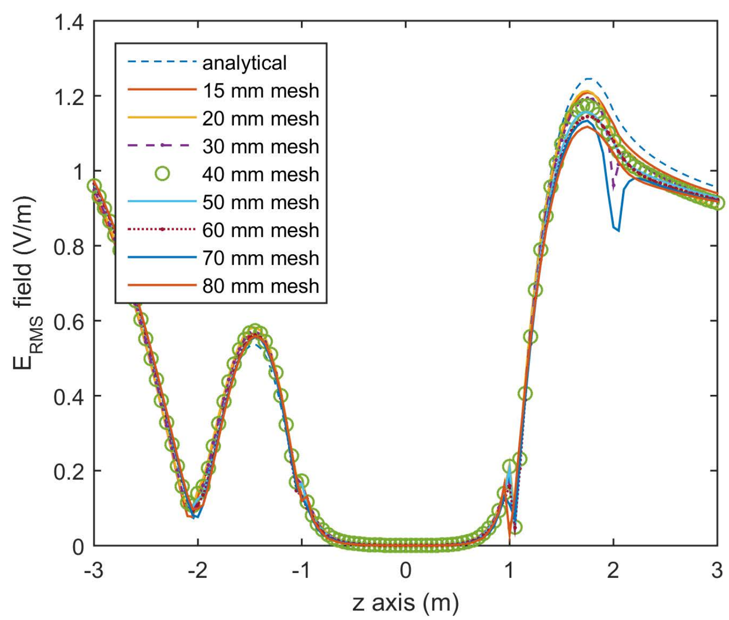

Figure 6.7. E_{RMS} field along z axis for different meshing size.

As a conclusion, the uncertainty coming from the simulation settings is discussed. With the existing simulation settings, the relative error for the electric field is within 3.33%. In terms of SAR, which is proportional to the square of electric field, the relative error is about 6.7%.

6.1.4 Post-processing

During the post-processing portion, the maximum 1g-averaged SAR is needed for characterization of MRI RF heating effects. In our simulation studies, the powerful SEMCAD X post-processing module can automatically calculate the 1g-averaged SAR. In this section, the uncertainty of the averaging is discussed.

Instead of a simple sphere structure with known analytical solution, a different simulation is used to reflect the clinical reality. Here we choose the case which was discussed in Chapter 4 for leg phantom validation. As shown in Figure 4.27, a 10 cm titanium rod with 1/8 inch diameter is placed inside the leg phantom. The front view shows that the rod is at the center of the leg phantom in the z direction, while the bottom view shows that the rod is at 3 cm from the left edge of the leg phantom gel, and in the center plane in the y direction.

Figure 6.8 plots the 1g-averaged SAR distribution around the 10 cm rod. The red circle denotes where the 1g box with maximum 1g-averaged SAR is located. For uncertainty analysis, the 0.9g-averaged SAR and 1.1g-averaged SAR were calculated. Table 6.3 shows the absolute and relative change for different averaged mass. When changing the averaged mass by 10%, the relative error for averaging is around 6%. Thus the sensitivity of averaging is 0.6%/%.

Table 6.3. Absolute and relative error for different averaging weight

Averaged SAR over mass(g)	0.9	1	1.1
Maximum averaged SAR(W/kg)	89.9	84.3	79.6
Absolute difference (W/kg)	5.6	0	-4.7
Percentage error (%)	6.64	0	-5.58

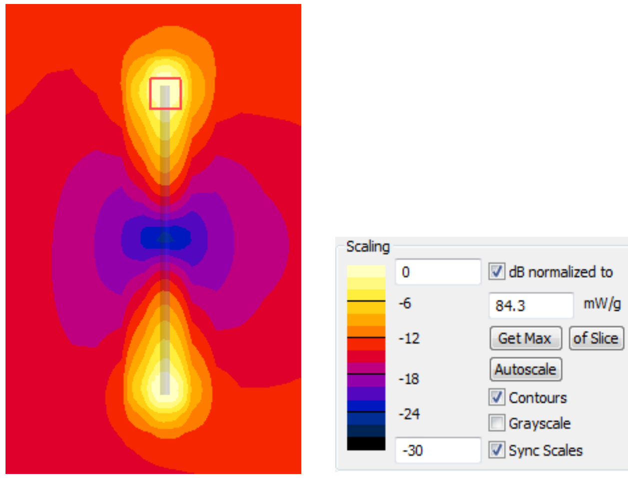

Figure 6.8. The 1g-averaged SAR distribution around 10 cm rod.

6.2 Measurement Uncertainty

To assess the quality of the experimental measurement, an uncertainty analysis is necessary. As discussed in Chapter 4, the 10 cm titanium rod inside the leg phantom experiment shows good agreement with the simulation. This simulation is a good approximation for experimental results, and thus is treated as the standard testing method. Here we use this case to quantify the measurement error of the MRI RF experimental system. The experimental setup is the same as depicted in the previous example. While many factors may have an impact on the MRI RF coil induced heating measurement, the following primary parameters are discussed.

6.2.1 Probe Uncertainty

During experiment, the MRI RF coil induced heating is indicated by the local temperature rise. Optic fiber temperature probes are used to measure temperature changes. Ideally, the temperature probe should be placed at the maximum heating spot for monitoring. However, the probe is attached to the tip of the rod with rubber band in practice. This generates inaccuracy of temperature probe position. The inaccuracy issue becomes significant since the temperature drops rapidly from the tip of the screw. To analyze the effect of probe positioning, a thermal simulation is conducted based on the existing EM simulations. The temperature rise around the tip of the rod is plotted in Figure 6.9. The red ball in Figure 6.9 shows the 2 mm range from the tip of the rod. Within this 2 mm range, the temperature drop in each direction is listed in Table 6.4. The variance in z direction has the most significant impact; changing 2 mm in the positive z direction will lead to 22.6% uncertainty. In an experiment, when we place the temperature probe near the tip of the rod, the distance between the active region of the temperature probe and the tip of the rod can be controlled less than 1 mm. Details for calculating the combined sensitivity can be found in Table 6.4, which gives a combined sensitivity (CS) of 10.81%/mm.

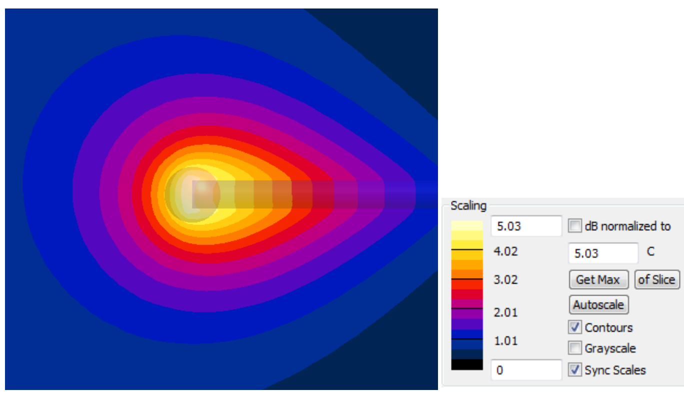

Figure 6.9. Temperature rise around the tip of the rod.

Table 6.4. Temperature increase in different directions

Direction	Offset (mm)	T (°C)	Offset (mm)	T (°C)	Averaged change	Factor (%/mm)	CS (%/mm)
	0	5.03					
x	+2	4.58	-2	4.66	8.15%	4.08	
y	+2	4.25	-2	4.70	11.03%	5.51	10.81
z	+2	3.88	-2	4.50	16.70%	8.35	

6.2.2 Device Location

When conducting an experiment, the rod is expected to be located at the center of the leg in z direction, and 3 cm from the left edge in center $y-z$ plane. In reality, manually placing the rod inside the leg phantom will lead to inaccuracy in device location. Table 6.5 shows the maximum temperature increase when 1 cm offset in positive or negative x, y, and z directions is achieved in simulation. With a 1 cm change in y direction, the temperature increase around the tip of the rod can be affected by about 1 °C. Moving toward the edge will result in more temperature increase and vice versa. This is expected since the incident electric field is stronger at the edge of the leg phantom. As a result, the uncertainty in the y direction is 21%, and the uncertainty in x, z direction is 1.59% and 2.58%. Table 6.5 gives an estimated combined sensitivity (CS) of 21.09 %.

Table 6.5. Temperature increase of device when moved 1cm in different locations

Direction	Offset (cm)	T (°C)	Offset (cm)	T (°C)	Averaged change	Factor (%/cm)	CS (%/cm)
	0	5.03					
x	+1	5.15	-1	4.99	3.18%	1.59	
y	+1	3.94	-1	6.04	-41.75%	-20.87	21.09
z	+1	5.14	-1	4.88	5.17%	2.58	

6.2.3 Medium Parameters

As per the international standard ASTM F2182, the relative permittivity of the phantom gel is 80.38, while the electrical conductivity is 0.47 S/m. The actual permittivity and conductivity can be rarely guaranteed to be exactly the same value as in the standard. These parameters are sensitive to the temperature, humidity, barometric pressure, etc. The relative change in permittivity or conductivity can be up to 10%. By implementing the 10% error, the simulation results can be viewed in Table 6.6.

Table 6.6. Temperature increase for different parameter change

Permittivity/conductivity change	90%	110%	Reference
Temperature increase (°C)	4.87	5.43	5.03
Percentage error	2.8%	8%	

When the electric parameters increase by 10%, the uncertainty in temperature increase is 8%, while the uncertainty for decreasing electric parameters by 10% leads to 2.8% uncertainty. The averaged sensitivity is 5.4%.

6.3 Summary

Through numerical simulations, we are able to perform uncertainty analysis for MRI RF coil induced heating evaluation. For simulations, the total uncertainty is bounded within 6.7% based on comparison between numerical results with analytical solutions. Post-processing may produce 0.6% uncertainty. Experimental measurement uncertainties may come from probe positioning, device location and medium parameters. Assuming that all the parameters are independent with each other, the uncertainty may go up to 14.99% by calculating the root-sum-square of each uncertainty budget as shown in Table 6.7.

Table 6.7. Uncertainty budget for MRI RF experiment system

	Sensitivity	Probability distribution	Standard deviation	Standard uncertainty(%)
Simulation settings				6.7
Post-processing	0.6%/%	N	1%	0.6
Probe uncertainty	10.81%/mm	R	1 mm/$\sqrt{3}$	6.24
Device location	21.09%/cm	N	0.5 cm	10.55
Medium parameters	0.54%/%	N	10%	5.4
Combined standard uncertainty		RSS		14.99

Chapter 7

Conclusions and Future Work

7.1 Conclusions

External fixation is a surgical treatment used to stabilize bone and soft tissues. When dealing with the MRI-related safety issues, the external fixation devices may exhibit severe RF coil induced heating effects. The primary contribution of this dissertation is to numerically evaluate the MRI RF coil induced heating effects of external fixation devices and the technique to reduce this thermal impact.

The idea of using absorption material to reduce RF coil induced heating effects is proposed in Chapter 3. For modular external fixation devices, the reduction of using absorption material is validated through simulations and experiments. The Response Surface Methodology indicates low permittivity absorption material with a conductivity of 0.007 S/m will achieve optimum heat reduction for the specific modular external fixation design.

The MRI RF coil induced heating effects of circular external fixation devices is discussed in Chapter 4. Due to the limitations of the conventional testing procedure, a novel methodology, including the leg phantom and the incident B1 field normalization, is proposed. The leg phantom has similar electric field distribution to represent human legs when B_1 field normalization is applied. With the presence of circular external fixation device, the MRI RF coil induced heating effects on the leg phantom exhibit the same trend as in the human models. Numerical investigation using incident B_1 field normalization on leg phantom simulations suggests that all screw configuration with fewer screws, large ring frame size and relatively large strut length and the maximum insertion angle pointing outwards may lead to the worst case MRI RF coil induced heating.

Chapter 5 applies the technique of using absorption material to the circular external fixation device. When appropriately choosing the electromagnetic characteristics of the absorption material, we are able to reduce the MRI RF heating effects significantly by simply attaching the material in the connection part of the screws and the clamp. The maximum 1g-averaged SAR can be reduced from 346 W/kg to 22.6 W/kg. A circuit model that represents the MRI RF coil induced heating is built based on the induced current behavior. The mechanism of using absorption material is analyzed qualitatively.

Preliminary error quantification analysis of RF coil induced heating measurement is introduced in Chapter 6. While simulation uncertainty is bounded within 6.7%, the combined uncertainty for whole MRI RF experiment system is 14.99%.

7.2 Future Work

A lot of work has been done to assess the effect of using absorption material on MRI RF coil induced heat reduction for external fixation devices. However, a number of related topics should be taken into consideration in the future.

Beyond the parameters of uncertainty analysis considered in this dissertation, some other factors may have effects on the experimental measurement. The uncertainty effects of the leg phantom location, RF coil field, etc. need to be rigorously analyzed.

In this dissertation, the MRI RF coil is implemented using non-physical current source together with the lumped circuit elements. Although this is the ideal current distribution that the RF coil needs to achieve, a physical coil model is necessary for better representation of commercial MRI RF coils. To design such a physical MRI RF coil, numerical simulations need to be performed to match the clinical reality.

With the development of MRI RF coils, RF shimming is now available for most MR equipment. RF shimming aims at B1 field homogeneity improvement, which is implemented through phase and/or magnitude adjustment of each channel in MRI RF coil. The impact of this state-of-the-art technique on MRI RF coil induced heating is still unknown. Since the MRI RF induced heating is closely related to the amplitude and phase shift for each source port, there should exist Eigen modes of excitation. By expanding the source excitations into the superposition of Eigen modes, we can do a quick MRI RF heating effects estimation.

References

[1] F. G. Shellock, T. O. Woods, and J. V. Crues III, "MR Labeling Information for Implants and Devices: Explanation of Terminology," *Radiology*, vol. 253, no. 1, pp. 26–30, 2009.

[2] ASTM F2503, "Standard Practice for Marking Medical Devices and Other Items for Safety in the Magnetic Resonance Environment," *West Conshohocken, PA, ASTM International*, 2005.

[3] A. R. Rezai, D Finelli, J. A. Nyenhuis, G Hrdlicka, J Tkach, A Sharan, P Rugieri, P. H. Stypulkowski, and F. G. Shellock, "Neurostimulation Systems for Deep Brain Stimulation: In Vitro Evaluation of Magnetic Resonance Imaging-related Heating at 1.5 Tesla," *J Magn Reson Imaging*, vol. 15, no. 3, pp. 241–250, 2002.

[4] J Powell, A Papadaki, J Hand, A Hart, and D McRobbie, "Numerical Simulation of SAR Induced around Co-Cr-Mo Hip Prostheses in Situ Exposed to RF Fields Associated with 1.5 and 3 T MRI Body Coils," *Magn Reson Med*, vol. 68, no. 3, pp. 960–968, 2012.

[5] Y. Liu, J. Chen, F. G. Shellock, and W. Kainz, "Computational and Experimental Studies of an Orthopedic Implant: MRI-related Heating at 1.5-t/64-MHz and 3-t/128-MHz," *J Magn Reson Imaging*, vol. 37, no. 2, pp. 491–497, 2013.

[6] C. Marincas, M. Mada, D. Rotaru, A. Carpenter, and R. Ciupa, "Evaluation of Radio Frequency-induced Heating near Fixed Orthodontic Applicances during MRI Examination at 3 Tesla," *ACTA Electrotehnica*, vol. 54, no. 1, pp. 72–75, 2013.

[7] S. Ayyldz, K. Kamburolu, C. Sipahi, S. Murat, S. Grgl, and B. Pikin, "Radiofrequency Heating and Magnetic Field Interactions of Fixed Partial Dentures

during 3-Tesla Magnetic Resonance Imaging," *Oral and maxillofacial radiology*, vol. 166, no. 5, pp. 640–647, 2013.

[8] F. G. Shellock, "Metallic Neurosurgical Implants: Evaluation of Magnetic Field Interactions, Heating, and Artifacts at 1.5-Tesla," *J Magn Reson Imaging*, vol. 14, no. 3, pp. 295–299, 2001.

[9] S. A. Mohsin, N. M. Sheikh, and W. Abbas, "MRI Induced Heating of Artificial Bone Implants," *Journal of Electromagnetic Waves and Applications*, vol. 23, no. 5-6, pp. 799–808, 2009.

[10] H. Muranaka, T. Horiguchi, Y. Ueda, S. Usui, N. Tanki, and O. Nakamura, "Evaluation of RF Heating on Hip Joint Implant in Phantom during MRI Examinations," *Nihon Hoshasen Gijutsu Gakkai Zasshi*, vol. 66, no. 7, pp. 725–733, 2010.

[11] M. Niehaus and J. Tebbenjohanns, "Electromagnetic Interference in Patients with Implanted Pacemakers or Cardioverter-Defibrillators," *Heart*, vol. 86, no. 3, pp. 246–248, 2001.

[12] S. L. Pinski and R. G. Trohman, "Interference in Implanted Cardiac Devices, Part II," *Pacing and clinical electrophysiology*, vol. 25, no. 10, pp. 1496–1509, 2002.

[13] R. Luechinger, V. A. Zeijlemaker, E. M. Pedersen, P. Mortensen, E. Falk, F. Duru, R. Candinas, and P. Boesiger, "In Vivo Heating of Pacemaker Leads during Magnetic Resonance Imaging," *European Heart Journal*, vol. 26, no. 4, pp. 376–383, 2005.

[14] W. R. Nitz, A. Oppelt, W. Renz, C. Manke, M. Lenhart, and J. Link, "On the Heating of Linear Conductive Structures as Guide Wires and Catheters in Interventional MRI," *Journal of Magnetic Resonance Imaging*, vol. 13, no. 1, pp. 105–114, 2001.

[15] E. Mattei, G. Calcagnini, M. Triventi, F. Censi, P. Bartolini, W. Kainz, and H. Bassen, "MRI Induced Heating of Pacemaker Leads: Effect of Temperature Probe Positioning and Pacemaker Placement on Lead Tip Heating and Local SAR," in *Engineering in Medicine and Biology Society, 2006. EMBS'06. 28th Annual International Conference of the IEEE*, IEEE, 2006, pp. 1889–1892.

[16] K. B. Baker, J. Tkach, J. D. Hall, J. A. Nyenhuis, F. G. Shellock, and A. R. Rezai, "Reduction of Magnetic Resonance Imaging-related Heating in Deep Brain Stimulation Leads using a Lead Management Device," *Neurosurgery*, vol. 57, no. 4, pp. 392–397, 2005.

[17] D. A. Finelli, A. R. Rezai, P. M. Ruggieri, J. A. Tkach, J. A. Nyenhuis, G. Hrdlicka, A. Sharan, J. Gonzalez-Martinez, P. H. Stypulkowski, and F. G. Shellock, "MR Imaging-related Heating of Deep Brain Stimulation Electrodes: In Vitro Study," *American Journal of Neuroradiology*, vol. 23, no. 10, pp. 1795–1802, 2002.

[18] J. R. James, Y. Gao, M. A. Miller, A. Babsky, and N. Bansal, "Absolute Temperature MR Imaging with Thulium 1, 4, 7, 10-Tetraazacyclododecane-1, 4, 7, 10-Tetramethyl-1, 4, 7, 10-Tetraacetic Acid (TmDOTMA-)," *Magnetic Resonance in Medicine*, vol. 62, no. 2, pp. 550–556, 2009.

[19] R. Luechinger, P. Boesiger, and J. A. Disegi, "Safety Evaluation of Large External Fixation Clamps and Frames in a Magnetic Resonance Environment," *Journal of Biomedical Materials Research Part B: Applied Biomaterials*, vol. 82, no. 1, pp. 17–22, 2007.

[20] Y. Liu, J. Shen, W. Kainz, S. Qian, W. Wu, and J. Chen, "Numerical Investigations of MRI RF Field Induced Heating for External Fixation Devices," *Biomedical engineering online*, vol. 12, no. 1, p. 12, 2013.

[21] ASTM F2182, "Standard Test Method for Measurement of Radio Frequency Induced Heating On or Near Passive Implants During Magnetic Resonance Imaging," *West Conshohocken, PA, ASTM International*, 2011.

[22] "Assessment of the Safety of Magnetic Resonance Imaging for Patients with an Active Implantable Medical Device,"

[23] IEC 60601-2-33, "Particular Requirements for the Basic Safety and Essential Performance of Magnetic Resonance Equipment for Medical Diagnosis," 2012.

[24] F. A. Jolesz, "Invited. Interventional and Intraoperative MRI: A General Overview of the Field," *Journal of Magnetic Resonance Imaging*, vol. 8, no. 1, pp. 3–7, 1998.

[25] J. Schenck, "Health Effects and Safety of Static Magnetic Fields," *Magnetic Resonance Procedures: Health Effects and Safety*, pp. 1–29, 2001.

[26] "Effect of Insulating Layer Material on RF-induced Heating for External Fixation System in 1.5 T MRI System,"

[27] C. J. Yeung and E. Atalar, "A Greens Function Approach to Local RF Heating in Interventional MRI," *Medical physics*, vol. 28, no. 5, pp. 826–832, 2001.

[28] SEMCAD X, "Reference Manual for the SEMCAD Simulation Platform for Electromagnetic Compatibility, Antenna Design and Dosimetry," *SPEAG - Schmid & Partner Engineering AG*, 2006.

[29] *Safety Information Article*, http://www.mrisafety.com/SafetyInfov.asp?SafetyInfoID=268, Online; accessed 27-April-2016.

[30] Y. Liu, J. Shen, W. Kainz, S. Qian, W. Wu, and J. Chen, "Computational Study of External Fixation Devices Surface Heating in MRI RF Environment," in *Electromagnetic Compatibility (EMC), 2012 IEEE International Symposium on*, IEEE, 2012, pp. 612–616.

[31] C. Lenarz, G. Bledsoe, and J. T. Watson, "Circular External Fixation Frames with Divergent Half pins: A Pilot Biomechanical Study," *Clinical orthopaedics and related research*, vol. 466, no. 12, pp. 2933–2939, 2008.

[32] C. E. Hayes, W. A. Edelstein, J. F. Schenck, O. M. Mueller, and M. Eash, "An Efficient, Highly Homogeneous Radiofrequency Coil for Whole-body NMR Imaging at 1.5 T," *Journal of Magnetic Resonance (1969)*, vol. 63, no. 3, pp. 622–628, 1985.

[33] P. Nordbeck, F. Fidler, I. Weiss, M. Warmuth, M. T. Friedrich, P. Ehses, W. Geistert, O. Ritter, P. M. Jakob, M. E. Ladd, H. H. Quick, and W. R. Bauer, "Spatial Distribution of RF-induced E-fields and Implant Heating in MRI," *Magnetic resonance in medicine*, vol. 60, no. 2, pp. 312–319, 2008.

[34] F. G. Shellock and J. V. Crues, MRI Bioeffects, Safety, and Patient Management. 2014.

[35] A. Christ, W. Kainz, E. G. Hahn, K. Honegger, M. Zefferer, E. Neufeld, W. Rascher, R. Janka, W. Bautz, J. Chen, B. Kiefer, P. Schmitt, H.-P. Hollenbach, J. Shen, M. Oberle, D. Szczerba, A. Kam, W. J. Guag, and N. Kuster, "The Virtual Family Development of Surface-based Anatomical Models of Two Adults and Two Children for Dosimetric Simulations," *Physics in medicine and biology*, vol. 55, no. 2, N23, 2009.

[36] ASTM D2413-99, "Standard Practice for Preparation of Insulating Paper and Board Impregnated with a Liquid Dielectric," *West Conshohocken, PA, ASTM International*, 2009.

[37] ASTM D149-09, "Standard Test Method for Dielectric Breakdown Voltage and Dielectric Strength of Solid Electrical Insulating Materials at Commercial Power Frequencies," *West Conshohocken, PA, ASTM International*, 2009.

[38] X. Huang, J. Zheng, X. Wu, M. Kono, H. Hozono, W. Kainz, F. Yang, and J. Chen, "MRI Heating Reduction for External Fixation Devices using Absorption Material," *Electromagnetic Compatibility, IEEE Transactions on*, vol. 57, no. 4, pp. 635–642, 2015.

[39] A. Hasnain, M. I. Imran, Z. S. Rohaiza, S. Roslan, A. A. Takiyuddin, A. Rusnani, and A. A. Azremi, "Preliminary Development of Mini Anechoic Chamber," in *Applied Electromagnetics, 2007. APACE 2007. Asia-Pacific Conference on*, IEEE, 2007, pp. 1–5.

[40] J. Antony, Design of Experiments for Engineers and Scientists. Elsevier, 2014.

[41] D. C. Montgomery, G. C. Runger, and N. F. Hubele, Engineering Statistics. John Wiley & Sons, 2009.

[42] D. C. Montgomery, Design and Analysis of Experiments. John Wiley & Sons, 2008.